Understanding the Solar System with Numerical Simulations and Lévy Flights

Thesis by

Benjamin F. Collins

In Partial Fulfillment of the Requirements
for the Degree of
Doctor of Philosophy

California Institute of Technology
Pasadena, California

2009
(Defended May 21, 2009)

Acknowledgements

This work, literally, would not have been possible without my adviser, Re'em Sari. Collaborating with Re'em was a constantly enlightening process, and I'm very grateful for his attention, patience, and generosity as we worked together for the last six years.

Margaret Pan has been a great mentor ever since I joined her and Re'em in studying planetary dynamics. Hilke Schlichting has been an invaluable compatriot through all of our academic rites. While working and traveling with Re'em, Margaret, and Hilke, I have had many terrific adventures that I will always remember fondly.

I would like to thank my committee: Marc Kamionkowski, Shri Kulkarni, and Dave Stevenson. In addition to their roles in the preparation and defense of this thesis, I have benefited greatly from interacting with each of them in classrooms, meeting rooms, or impromptu conversations.

Finally, I thank my parents, Gale and Malcolm, and my brothers, Steven and Andrew, for their unwavering encouragement of my academic pursuits.

Abstract

This thesis presents several investigations into the formation of planetary systems and the dynamical evolution of the small bodies left over from this process.

We develop a numerical integration scheme with several optimizations for studying the late stages of planet formation: adaptive time steps, accurate treatment of close encounters between particles, and the ability to add non-conservative forces. Using this code, we simulate the phase of planet formation known as "oligarchic growth." We find that when the dynamical friction from planetesimals is strong, the annular feeding zones of the protoplanets are inhabited by not one but several oligarchs on nearly the same semimajor axis. We systematically determine the number of co-orbital protoplanets sharing a feeding zone and the width of these zones as a function of the strength of dynamical friction and the total mass of the disk. The increased number of surviving protoplanets at the end of this phase qualitatively affects their subsequent evolution into full-sized planets.

We also investigate the distribution of the eccentricities of the protoplanets in the runaway growth phase of planet formation. Using a Boltzmann equation, we find a simple analytic solution for the distribution function followed by the eccentricity. We show that this function is self-similar: it has a constant shape while the scale is set by the balance between mutual excitation and dynamical friction. The type of evolution described by this distribution function is known as a Lévy flight.

We use the Boltzmann equation framework to study the nearly circular orbits of Kuiper Belt binaries and the nearly radial orbits of comets during the formation of the Oort cloud. We calculate the distribution function of the eccentricity of Kuiper belt systems, like the moons of Pluto, given the stochastic perturbations caused by close encounters with other Kuiper belt objects. For Oort cloud comets, we find the distribution function of the angular momentum as it is excited by perturbations from passing stars in the Galaxy. Both systems evolve as Lévy flights. This work unifies the effects of stochastic stellar encounters and the smooth torque from the Galactic potential on Oort cloud comets.

Contents

List of Figures

List of Tables

Chapter 1

Introduction and Overview

Astronomy was born as the first scientists, in ancient times, meticulously tracked the motion of the planets across the sky. As technology has improved, ever distant regions of the universe have become accessible, revealing a diverse menagerie of objects with fascinating properties. However, there is still much to learn about the solar system itself. We can now catalogue the tiny denizens of the outer regions of the solar system and study the orbits of their smaller satellites. We routinely leverage enormous computational power to contemplate the formation of planetary systems from the primordial dust and gas. Robotic explorers have been sent to the other planets and their moons to return in-depth measurements and high resolution images. After all this time, new data still raises new questions and the scientific frontier is pushed forward.

The work presented in this thesis focuses on understanding the processes that created the planets of our solar system. We developed a numerical code to simulate the orbital evolution of the solid bodies that eventually grow into planets. Analytic studies of the dynamics of these objects enrich the numerical work by providing a more complete understanding of the interactions of the protoplanets with themselves and the rest of the disk. Debris left over from the planet formation process exists today in the Kuiper Belt and Oort Cloud; further analytic work examines the processes that shape the orbits of these bodies in the time after the solar system formed. Understanding the evolution of their orbits allows us to determine how the conditions during their formation can be deduced from their current properties.

1.1 Numerical Code

The two-body Keplerian orbit is one of the most famous analytic solutions in physics. However, when an additional massive object is added to the system, the dynamics become quite complex. Numerical integration of the equations of motion is the only feasible way to solve directly for the interacting orbits of the myriad protoplanetary objects that eventually grow into full-sized planets.

The growth of computing power in combination with algorithmic advances has given rise to a rich literature on the dynamics of a population of protoplanets. Arguably the most important computational development has been the popularization of symplectic integration schemes, starting with the work of Wisdom & Holman (1991). The astonishing advantage of these codes is that the error in the total energy due to the discretization of the integration is bounded. The equations can then be evolved with a much larger time step than in a conventional integration scheme, however the time step must remain fixed throughout the calculation. This is a significant disadvantage in certain contexts where the required time resolution may vary a great deal (a very close passage of two bodies, or modeling multiple orbits with a wide range of orbital periods). Much work has addressed these issues. Mercury (Chambers, 1999) and SyMBA (Duncan et al., 1998) are two symplectic codes that allow close encounters between the particles. Saha & Tremaine (1994) introduced a symplectic algorithm that allows each particle to have its own time step.

As part of the work presented in this thesis, we developed a new integration scheme that is designed to handle the technical problems inherent in studying the later stages of planet formation. Because it is the collisions between protoplanets that lead to their growth, it is essential that our code treats close encounters accurately. The code must be able to account for the growth of the eccentricities of protoplanets to very large values as they excite each other. Lastly, we require the capability to add extra terms to the orbital evolution in a simple way, with the intent of representing the influence of the planetesimals not through a separate integration, but by including their average effects analytically in the equations of motion of the protoplanets.

We choose special variables to minimize the error associated with discretizing the continuous physical system. Instead of describing the motion of each particle with Cartesian coordinates and velocities, we integrate constants of the two-body solution of each particle around the central mass. The central acceleration is then implicitly accounted for, and integration handles only the perturbations caused by interparticle forces. We employ a fifth-order Runge-Kutta algorithm with adaptive time steps (Cash & Karp, 1990; Press et al., 1992), and use a Newton-Raphson algorithm to solve Kepler's equation. By using an adaptive time step algorithm, we achieve the stated goal of handling phenomenon that occur over a range of timescales. The simplicity of the equations easily allows the specification of non-gravitational forces. For close encounters, we use the same differential equations to integrate the relative motion of the two bodies and the orbit of their center of mass around the central star.

Test integrations of our code show that it cannot avoid the eventual quadratic error growth in position that plagues non-symplectic and non-time-reversible schemes (Quinlan & Tremaine, 1990). However, its error growth is better behaved than a conventional non-symplectic code, and it indeed takes bigger time steps, allowing for a more computationally efficient calculation. This code was an essential part of the investigations presented in Chapters 3, 4, and 5.

1.2 Co-Orbital Oligarchy

Chapter 3 presents numerical studies of the oligarchic phase of a protoplanetary disk. In this phase, proposed by Lissauer (1987) and studied by Kokubo & Ida (1998), the runaway growth of the protoplanets has left their number density low enough that they no longer experience frequent collisions. Each protoplanet then holds court over a thin annulus of the disk, and grows only by accreting nearby planetesimals. This shuts off runaway growth; the protoplanets spend most of their formation time in this phase. Occasionally, the protoplanets grow too large for their spacing to be dynamically stable. They then enter a period of chaotic close encounters. When collisions have lowered the number density of protoplanets enough, the oligarchs settle into a new stable configuration. At some point in the evolution of the disk, a stable configuration does not exist, and the protoplanets undergo a final round of strong interactions before ending up with close to their final mass (Goldreich et al., 2004a).

The dynamical friction from planetesimals is an important part of this process. Kokubo & Ida (1996, 1998) included the planetesimals explicitly in their simulations, however their planetesimals had to be large to keep the total particle number low enough to be computationally feasible. With our new simulation code, we include the effects of the planetesimals on the protoplanets without having to calculate the orbits of each individual body. This lets us study the oligarchic phase of planet formation in a more highly-damped regime.

Our simulations show that after a period of excitation, one or more protoplanets in the resulting oligarchy orbit stably at nearly the same semimajor axis. Just as collisions bring the disk towards stability by reducing the number density, the co-orbital resonances prevent those protoplanets from undergoing close encounters with each other. In Chapter 3, we present a suite of simulations to explore systematically the typical number of co-orbital oligarchs as a function of the total protoplanet mass and the strength of the dynamical friction (given by the total mass of planetesimals). A significant number of co-orbital protoplanets qualitatively changes the relationship between the oligarchic disk and the final planets. In the inner solar system, dividing the available solids into a higher number of co-orbital protoplanets decreases the mass of each one. In the giant impact phase that follows oligarchy, more collisions are then required to assemble the final terrestrial planets. In the outer solar system, where the planets reach their final size during the oligarchic phase, an enhancement of the disk is necessary to provide the material for the extra co-orbital protoplanets.

1.3 Shear-Dominated Protoplanetary Dynamics

Two important functions that describe the state of a protoplanetary disk at a given time are the mass distribution and the velocity distribution of the particles. The two are related since the accretion rate depends on the relative velocities of the interacting objects, and the velocity dispersion is in turn set by the distribution of sizes of the protoplanets and planetesimals. In a Keplerian disk, the velocity dispersion is related to the eccentricity distribution: particles with some eccentricity have an extra motion on top of the background rotation of the disk.

Much previous work has sought analytic descriptions of the rates of accretion and eccentricity evolution. One technique, summarized by Stewart & Ida (2000), is to calculate average diffusion coefficients that describe the time derivative of the root-mean-squared eccentricity of the protoplanets or planetesimals.

In Chapters 4 and 5, we present a different approach to studying the eccentricities of the protoplanets. We calculate the probability density of the protoplanets' eccentricities given the dissipation of dynamical friction and the stochastic mutual excitations. We use a Boltzmann equation that relates the probability for a single perturbation to the full distribution function of the eccentricity. In spite of the complex nature of the multi-body dynamics in the protoplanetary disk, we find an astonishingly simple analytic solution for the distribution function when the balance between mutual excitations and dynamical friction allows a steady state. The probability of finding a protoplanet in a logarithmic interval of e is exactly:

$$\frac{dn(e)}{d\log e} = \frac{(e/e_c)^2}{(1+(e/e_c)^2)^{3/2}}. \tag{1.1}$$

This function has a peak around $e \approx e_c$, which corresponds, to an order of magnitude, to the eccentricity at which the timescale for dynamical friction is equal to the timescale for excitation. Above e_c, the distribution function decreases as e^{-1}; the mean of the distribution is logarithmically divergent, and the variance is undefined.

The full distribution of eccentricities allows us to make several conclusions. The overall shape of the distribution, a two-dimensional Cauchy distribution, is qualitatively different than the Rayleigh distribution that is commonly assumed in the literature; Rayleigh distributions fall exponentially at high eccentricity while our findings show a power law behavior. The typical kinetic energy, which scales as e^2, is dominated then by the fewer protoplanets with the highest eccentricities, while most of the protoplanets have eccentricities of about e_c. Numerical simulations using the code described in Chapter 2 verify the analytic solution.

Chapter 5 extends the results of Chapter 4 to apply to protoplanets that are not in a steady state, such as a disk where there is no dynamical friction, or if the total mass of protoplanets or of planetesimals is changing with time. Further analysis of the Boltzmann equation reveals that the time-dependent distribution function is self-similar: it retains a constant shape (Equation 1.1) while the eccentricity scale, e_c, evolves with time. The time-dependent scale factor, $e_c(t)$, is set by the surface mass density in protoplanets, that in planetesimals, and the distance of this region from the

Sun. Assuming a self-similar solution, the Boltzmann equation reduces to two equations that specify the distribution function. The first is a dimensionless version of the Boltzmann equation, whose solution is the shape described by Equation 1.1. The second is an ordinary differential equation that relates the rate of change of the eccentricity scale, $\dot{e}_c(t)$, to the damping and excitation timescales.

When dynamical friction is included, this ODE reproduces the results of Chapter 4: e_c is constant and set by the equilibrium between dynamical friction and protoplanet stirring. If there is no damping, e_c grows linearly, and the shape of the distribution is maintained while it moves to higher values of eccentricity. Thus Equation 1.1 is an accurate description of the eccentricities of the protoplanets for both steady-state and dynamically evolving scenarios. The time-dependent scale $e_c(t)$ handles the evolution of the physical parameters, such as the surface densities. Again, numerical simulations of this process provide a stunning verification of the analytic results.

1.4 Lévy Flights of Circular Binary Orbits

The Kuiper belt is a collection of icy bodies outside of Neptune's orbit that contains leftover planetesimals from planet formation in the outer solar system; Pluto is one of its most famous members. Recent high resolution imaging has shown Pluto to be surrounded by two very small moons in addition to its larger partner Charon (Weaver et al., 2006). Further observations constraining the orbits of the satellites show that all three have small but finite eccentricities (Tholen et al., 2008). Several other Kuiper belt objects of about the size of Pluto have been discovered and found to have nearly circular satellites of their own (Brown et al., 2005, 2006). For most of these systems, tidal interactions between the primary and the satellites are expected to damp the eccentricity of the satellites, leaving their orbits completely circular.

Close approaches by other Kuiper belt objects (KBOs) are one possible source for the eccentricity of these systems. Stern et al. (2003) studied the forcing of the eccentricity of Pluto-Charon with a numerical experiment simulating random encounters from other KBOs. They found that the observed eccentricity of 0.003 is too large to be explained by the stochastic perturbations, given the theoretical estimate of the eccentricity damping rate.

Chapter 6 presents our efforts to determine an analytic solution for the distribution function of eccentricity created by the interactions between impulsive perturbers and a nearly circular binary orbit. We follow the same approach outlined in Chapters 4 and 5, and study the probabilities of eccentricity excitement through a Boltzmann equation. When the perturbers are more massive than the binary, that distribution is given by Equation 1.1. The type of diffusion followed by the eccentricity of the binary is known as a Lévy flight, and appears in nature under many diverse circumstances in chemistry, biology, and physics (Shlesinger et al., 1995). The eccentricities of the protoplanets discussed in Chapter 4 also follow Lévy flights. We exploit the analytic simplicity of

Lévy flights to solve for the distribution function of the binary's eccentricity for perturbing mass distributions of arbitrary power law slopes.

From the distribution function for the eccentricity of these systems we calculate confidence intervals for an observed eccentricity, given the mass distribution of the Kuiper belt. The eccentricities of the outer two satellites of Pluto are within these intervals. The eccentricity of Charon, on the other hand, is too large to be attributed to impulsive perturbations. The eccentricities of the satellites of the other two Plutoids, Eris, and Haumea, are consistent with external perturbations if tidal dissipation is ignored.

1.5 Stellar Perturbations and Galactic Tides Demystified

Another possible fate for the leftover planetesimals is that they become the Oort cloud of comets. At the end of planet formation, the perturbations from the new planets add energy to the planetesimals, but their periapses remain in the planetary region. Thus their eccentricity grows close to $e = 1$. Once the semimajor axes of the comets get large enough, perturbations from passing stars in the Galaxy begin to affect the orbits of the comets. Their periapses grow, saving them from the planetary perturbations and trapping them in what is called the Oort cloud. When the orbits of the small bodies evolve back into the planetary region, we observe them as comets.

Heisler & Tremaine (1986) found that the planar mass distribution of the Galactic disk exerts a torque on the comet that dominates the effects of stellar encounters over long timescales. Subsequent numerical studies of the formation of the Oort cloud have included both a mean growth of the magnitude specified by the Galactic tides and a stochastic term to represent stellar perturbations (Duncan et al., 1987; Heisler, 1990; Dones et al., 2004).

We tackle this problem with the techniques developed in the previous chapters. First we examine the perturbations caused by a single field star traveling on a straight trajectory. We then relate the spectrum of possible single perturbations to the distribution function of the comet's angular momentum. Amusingly, the angular momentum vector also follows a Lévy flight. The shape of the distribution function is the two-dimensional Cauchy distribution, and the typical value is set by a differential equation that depends on the parameters of the comet and the perturbing swarm. These similarities to the nearly circular case are a consequence of the identical scaling of the perturbation strength with the mass of a single perturber, its distance of closest approach to the comet, b, and its velocity, v_p.

To represent the planar structure of the Galactic disk in our treatment of stellar interactions, we restrict the velocity of the perturbers to a single direction. This causes an asymmetry in the probability distribution of angular momentum delivered by single encounters, where the perturbers that pass with $b \sim a$ (where a is the semi-major axis of the comet) deliver angular momentum preferentially to one component of the total angular momentum vector. The coherent accumulation from these perturbations causes the angular momentum vector to grow, on average, in one direction. This effect is exactly the torque derived from the smooth planar mass distribution and attributed to the tides from the Galactic disk.

This result unites the derivation of the Galactic tidal torque, which assumes a smooth mass distribution, with the fundamentally discrete nature of the perturbations by stars. Our calculations confirm that the mean of the distribution function of the angular momentum is always set by the tidal torque. However, at early times, the bulk of the distribution function remains axisymmetric, and the mean is manifested by the occasional rare nearby encounter. Only over timescales long enough that impact parameters near the comet are well sampled is the angular momentum likely to have a value close to the mean.

Chapter 2

A New Planetary Simulation Code: RKNB3D

In 1991, Wisdom & Holman revolutionized planetary dynamics. The symplectic integrators that they developed evolve the orbital equations of motions exactly under a Hamiltonian close to but different from the Hamiltonian of the physical system. The difference between the physical Hamiltonian and the numerical one represents the truncation error of the calculation. This error is typically bounded and does not accumulate throughout the integration. Accordingly, a symplectic integration can be carried out with a much larger time step than is possible when using a conventional integration scheme.

One downside is that the time step of a symplectic integrator must remain fixed throughout the calculation. In some contexts a fixed time step is not a problem, such as a long-term simulation of the outer solar system (Duncan & Quinn, 1993). In planet formation, however, there are occasional events that must be integrated with time steps much shorter than is necessary during the majority of the simulation. The acceleration experienced by very eccentric particles is stronger near periapse and weaker at apoapse, and this ratio can be extreme. Pairs of bodies often pass close enough to each other that their mutual gravitation is stronger than that from the star, but the encounters usually last less than a single orbital period. Setting the time step of the entire simulation to resolve these quick and isolated events reduces the efficiency of symplectic techniques.

Many authors have developed symplectic codes that address these problems. Saha & Tremaine (1994) devised an algorithm in which the time step of each particle is set independently; however the time step does not adapt in response to the events in the simulation, so this is not an ideal solution for the two problems mentioned above. SyMBA (Duncan et al., 1998) and Mercury (Chambers, 1999) are two codes that implement methods to integrate close encounters without interfering with the energy conservation of the overall integration.

Our goal in this work is to develop an integrator with adaptive time steps that is optimized for planet formation simulations. We also desire the ability to add arbitrary accelerations to represent the planetesimals that are too numerous to include directly. To compensate for not using a symplectic scheme, we focus on reducing the error accumulation with a judicious choice of parameters to describe the orbits of each particle. We describe our variables and how they evolve under an acceleration in Section 2.1. Section 2.2 discusses the algorithm used to integrate the equations, and Section 2.3 describes the additional features we have implemented to improve the performance of the simulations.

In Section 2.4 we test the performance of our code and compare its properties to several symplectic codes. We summarize our results in Section 2.5.

2.1 The Differential Equations

The most naive way to calculate the orbits of many gravitationally interacting particles is to integrate the changes in their positions and velocities directly. In the context of planetary systems, such a scheme overlooks the integrability of the two-body system. Specifically, the shape of the orbit of a single particle around a central mass is given by a closed-form analytic expression. Directly integrating the acceleration from the star introduces errors that, in a two-body system, are entirely avoidable. In our code, we integrate a set of osculating orbital elements instead of the positions and velocities. These parameters describe the solution to the two-body problem that each particle would follow if there were no accelerations besides that from the central object. Compared to the size of the central acceleration, the other perturbations are, typically, orders of magnitude smaller.

Our criterion for choosing the orbital elements to integrate is that they are well-behaved. We avoid the longitude of periapse and the longitude of the ascending node, since for circular non-inclined orbits they are not defined. More importantly, if the eccentricity and inclinations are small, small perturbations may change these angles by a large amount, forcing the integration algorithm to take more time steps than would otherwise be required.

Our code tracks nine parameters for each body: the energy per unit mass, $\mathcal{E}$, the two-dimensional eccentricity vector $\mathbf{e}$, the three-dimensional angular momentum per unit mass, $\mathbf{H}$, the current modified eccentric anomaly, $\bar{E}(t)$, the modified eccentric anomaly at a reference time, $\bar{E}_0$, and the mass of the particle, m. Since these quantities are constants of the two body solution, the only time derivatives that do not cancel to first order are those due to the interparticle accelerations, which we denote $\mathbf{A}$. The energy per unit mass, $\mathcal{E}$, evolves as:

$$\dot{\mathcal{E}} = \mathbf{A} \cdot \mathbf{v}. \tag{2.1}$$

The derivative of the energy is the work done by all the other particles.

The eccentricity vector, $\mathbf{e} = (\mathbf{v} \times \mathbf{H})/G(M_c + m) - \hat{r}$, evolves as:

$$\dot{\mathbf{e}} = \left(\frac{1}{G(M_c + m)} \right) \left[2\mathbf{r}(\mathbf{v} \cdot \mathbf{A}) - \mathbf{v}(\mathbf{r} \cdot \mathbf{A}) - \mathbf{A}(\mathbf{r} \cdot \mathbf{v}) \right]. \tag{2.2}$$

where M_c is the mass of the central body. This vector encapsulates both the scalar eccentricity $e = |\mathbf{e}|$ and the longitude of periapse relative to a reference direction, and is well behaved as the eccentricity of the particle goes to zero. This vector always lies in the orbital plane of the particle, so we integrate it using only the two components in that plane.

The derivative of the angular momentum per unit mass vector, **H**, is the torque:

$$\dot{\mathbf{H}} = \mathbf{r} \times \mathbf{A}. \tag{2.3}$$

This three-dimensional vector is integrated relative to a fixed coordinate system. It describes the orientation of the orbital plane in a more well-behaved way than the inclination angle and the line of nodes. Also, we can use its components to transform the position and velocities of the particles into and out of the orbital plane.

The modified eccentric anomalies, $\bar{E}$ and $\bar{E}_0$, are used in a version of Kepler's equation to find the phase of the particle as a function of time, given the rest of its orbital parameters.

$$n(t - t_0) = \bar{E} - \bar{E}_0 - e_1(\sin \bar{E} - \sin \bar{E}_0) + e_2(\cos \bar{E} - \cos \bar{E}_0), \tag{2.4}$$

where $n = (-2\mathcal{E})^{3/2}/G(M_c + m)$ is the orbital frequency, e_1 and e_2 are the components of $\mathbf{e}$ in the orbital plane, and $\bar{E}_0 = \bar{E}(t = t_0)$. This version of Kepler's equation is derived from the usual one by combining the eccentric anomaly with the longitude of periapse, $\bar{E} = E + \varpi$. Finding the phase by solving Kepler's equation is an alternative to integrating the phase itself over time, which would have caused errors to accumulate even when calculating the constant orbit of a single particle.

Instead of using the time of last periapse passage as a two-body constant of motion, we use the modified eccentric anomaly $\bar{E}_0$, which is also constant for a two-body system. The formula for $\dot{\bar{E}}_0$ is tedious to derive. The derivative of Equation 2.4 provides most of the terms, and we use the derivative of $x \sin \bar{E} - y \cos \bar{E}$ to solve for $\dot{\bar{E}}$, where x and y are the components of $\mathbf{r}$ in the orbital plane and are a function of $\bar{E}$.

Unfortunately, the expression for $\dot{\bar{E}}_0$ contains a term proportional to t. To reduce the effect this has on the integration, we update t_0 and $\bar{E}_0$ periodically for each particle. This introduces an accumulation of error with every rescaling, but at a much slower rate than a direct integration of the orbital phase.

The energy, $\mathcal{E}$, the eccentricity vector, $\mathbf{e}$, and the angular momentum, $\mathbf{H}$, all evolve smoothly through the transition between bound and unbound orbits. Unbound orbits, however, require a different version of Kepler's equation:

$$n(t - t_0) = e(\sinh F - \sinh F_0) - F + F_0, \tag{2.5}$$

where F and F_0 are the hyperbolic anomalies at time t and t_0 respectively (Danby, 1988). The equation for $\dot{F}_0$ again is tedious to derive but follows from algebraic manipulation of the derivatives of Equation 2.5 and the components of $\mathbf{r}(F)$.

Solving the modified Kepler's equation provides $\bar{E}(t)$ (or $F(t)$), which gives the position of the particle in the plane of its orbit. As noted above, the components of $\mathbf{H}$ provide the transformation between the orbital plane of each particle and the fixed frame. Since this transformation evolves as $\mathbf{H}$ evolves, the derivatives of $\mathbf{e}$ and $\bar{E}_0$, which are fixed in the orbital plane, must include additional terms depending on $\dot{\mathbf{H}}$.

Finally, we allow for the specification of an arbitrary $\dot{m}$, which, physically, could represent the average accretion rate of planetesimals onto the protoplanets in a simulation of planet formation. A time-dependent mass affects the translation between Cartesian coordinates and the elements. Physically, the elements do evolve as a result of planetesimal accretion; however, for simplicity, we set the derivatives of the other elements such that the shape of the orbit is not affected by a change in mass.

2.2 The Algorithms

Finding an efficient set of evolution equations is only part of the simulation scheme; choosing an effective algorithm to integrate them is also important. As stated before, one goal for this code is to implement adaptive time steps. Another goal is to allow the inclusion of additional accelerations to represent effects like dynamical friction that are caused by a population of bodies too numerous to be integrated. These forces can be dissipative, so we must not use algorithms that require a conservative force. Finally, we note that the most potentially computationally intensive part of our code is calculating the gravitational forces, which contributes to the total running time proportionally to N^2, where N is the number of particles. Thus we favor lower order codes that require fewer force evaluations.

We choose a fifth-order Runge-Kutta scheme with Cash-Karp coefficients (Cash & Karp, 1990; Press et al., 1992). In this algorithm, the values of the equations at the end of a time step can be estimated to any order below five using linear combinations of the same sub-step calculations. Comparing the fourth-order calculation to the full fifth-order one provides an estimate of the error in each step, which is used to adjust the size of the subsequent step. The accuracy of the integration is controlled by specifying a tolerance for the errors of each step. Since we anticipate our parameters to have small values, we use the absolute error of each variable to adjust the step size. Our implementation of this algorithm is based on the description by Press et al. (1992).

Since we rely on Equation 2.4 to provide the orbital phase of each body, we must solve it each time that we calculate the gravitational forces. We use the Newton-Raphson algorithm for finding the root of the equation for each particle (Danby, 1988; Murray & Dermott, 1999).

2.3 Enhancements

One advantage of this scheme is that it implicitly evolves the particles under the acceleration from the central mass, which typically provides the largest acceleration by several orders of magnitude. This hierarchy is reversed, however, when two particles suffer a very close encounter; in planet formation, these events are essential for the growth of the protoplanets and the excitation of their velocity dispersion. The distance from a particle where the motion due to the Sun is comparable to the motion caused by the gravity between the two close particles is known as the Hill radius; we use the definition that $R_{\mathrm{H}} = (m/(3M_{\odot}))^{1/3}a$.

As one particle approaches another on the scale of their Hill radii, the advantages of our differential equations are lost. To accurately describe the motion of one particle around the other, the constants of motion of the heliocentric two-body solution must undergo large rapid changes. However, in the limit that the particles are very close to each other, their relative motion is very close to a two-body solution, with the central star providing only a perturbation. We follow the objects through the close encounter by using the same differential equations to integrate the shape of the relative orbit. The center of mass of the pair of particles is not affected by their strong mutual acceleration, and is described well by a two-body solution around the central star.

Another coordinate transformation is necessary to handle the transition between bound and unbound orbits. Since the shape of bound and unbound orbits are fundamentally different, each regime requires its own conversion between the two-body constants of motion and the position of the particle. We implement a transition region in the code for the particles that are in between the two regimes. We integrate the position and velocity of these particles directly, including the acceleration from the central object as well as all other particles. While this solution offends the sense of error-minimization adhered to by the rest of the code, the relative amount of time spent integrating these coordinates is very small. The benefit is the ability to smoothly integrate an orbit that undergoes almost any kind of change.

We have also included the option to use orbital elements centered on the barycenter of the central object and one other body. In our code, the positions and velocities are always relative to the central object. If a test particle travels very far away from the system, the force should also become small and the code should take very large time steps. However, the acceleration of the other planets on the central mass does not decrease as the test particle moves away; in fact this indirect term causes the elements of the distant particle to vary substantially. By integrating the orbit of the test particle around the barycenter of the central mass and one of the other particles, part of the indirect term is eliminated. The circular-restricted three-body problem for very eccentric orbits is one example of a case where barycentric orbital parameters with an adaptive time step algorithm provide an overwhelming advantage over other routines.

2.4 Numerical Tests

To demonstrate the performance of our code, we present three tests. The first is to monitor the Jacobi constant, an integral of the motion in the circular-restricted three-body problem. We perform the same simulations as described in Section 6.3 of Duncan et al. (1998) so that, in addition to comparing the conservation of the Jacobi constant in the two codes, we can compare the qualitative results of our simulations with theirs. We integrate 50 massless particles interacting with a Neptune-sized planet, which has been placed on a circular orbit at 30 AU. The initial coplanar orbits of the test particles are such that all 50 have periapses at 30 AU, but their semimajor axes are spread evenly between 36 and 40 AU. The integrations are carried out for 10^9 years or until the massless particle collides with Neptune. Since many of the test particles do collide after undergoing many close encounters with Neptune, this is a good test of our code's ability to resolve the close encounters.

Our results are quite similar to those using the SyMBA code (Duncan et al., 1998). We find a median lifetime of the test particles of 4.5×10^6 years, within about a factor of two of their results. The average time steps of our simulations range between 2.0 and 8.3 years, with a median of 3.8. For comparison, the SyMBA integrations used a time step of 2 years. Our worst case error in the Jacobi constant is 1 out of 14,000; again this is close to the results of SyMBA's performance on this test. We point out that the error conservation is entirely dependent on the simulation time; particles that collided with Neptune earlier showed a much lower amount of accumulated error. The number of close encounters in a single simulation did not affect the rate of error accumulation, so we trust that our scheme for integrating close encounters has performed well.

We next examine the accumulation of error in the orbital phase of a particle, and compare it to the phase error of the same integration using the Mercury code (Chambers, 1999). This investigation is based on similar integrations comparing a variety of algorithms in Saha & Tremaine (1992). We integrate the orbit of a massless asteroid at 2.6 AU, with an eccentricity of 0.25 and an inclination of 0.2 rad. We include Jupiter with its current eccentricity and inclination. For both our code and Mercury, we perform several integrations with different levels of accuracy. By comparing the orbital phase of the asteroid in the most accurate simulation against the others, we estimate the absolute error in the orbital phase as a function of the specified time step or tolerance parameter.

To normalize the differences in the order of the two codes (RKNB3D being fifth-order and Mercury being second), we only compare the errors of simulations that use the same number of force evaluations per orbit. For RKNB3D, we divide the total number of force evaluations by the integration time to find the average number per orbit. RKNB3D has an inherent disadvantage in this metric, since our algorithm requires six force evaluations at each time step, and second-order symplectic codes require only one.

Figure 2.1 plots the orbit-averaged phase error for RKNB3D and Mercury in two sets of simula-

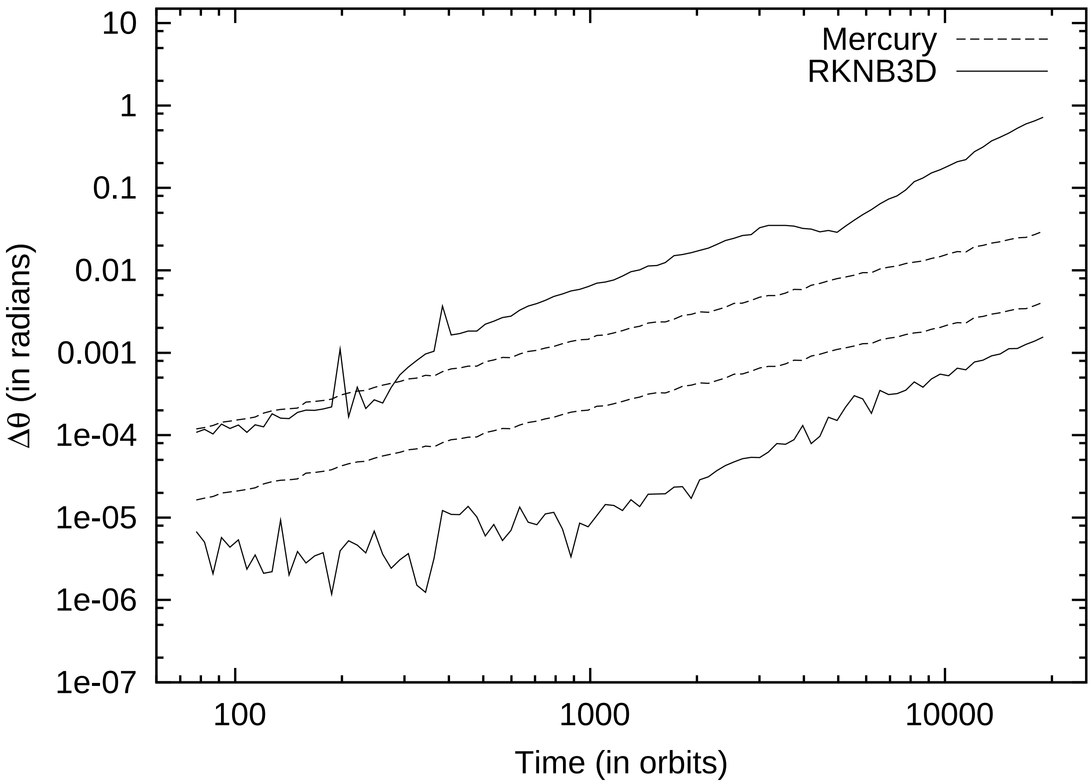

Figure 2.1 Root-mean-square error in orbital phase as a function of time in four integrations of Jupiter and an asteroid with eccentricity of 0.25. The solid lines are the error found with RKNB3D, and the dashed lines are the error from Mercury. The tolerance parameter of RKNB3D and the step size of Mercury have been chosen such that, on average, each code performs 100 force evaluations per orbit for the upper lines, and 300 for the lower ones.

tions. The upper lines are computed from simulations with 100 force evaluations each orbit, as in Figure 1 of Saha & Tremaine (1994). Each measurement is the root-mean-square of the difference in orbital phase at several points spread across multiple orbits. The phase error of the asteroid in Mercury, the dashed line, grows linearly with time over the entire length of the integration. The asteroid in our code, in the solid line, initially shows the same level of error. However after a few hundred orbits, the error accumulation accelerates, causing the phase error to grow faster than in the Mercury integrations.

For this scenario, the symplectic integrator has lived up to its reputation. However, since RKNB3D is a higher order code than Mercury, increasing the number of force evaluations per step has a greater effect on the overall error accumulation. The lower lines in Figure 2.1 correspond to simulations with 300 force evaluations per orbit. While the error in the orbital phase of both codes has decreased, the RKNB3D simulations shows less error accumulation over the entire integration.

This relatively simple configuration does not thoroughly test most of the functional improvements included in RKNB3D. As a second trial, we increase the eccentricity of the asteroid to 0.5. These simulations reveal a large degradation in the performance of Mercury for all time steps. In simulations using 100 force evaluations per orbit, the phase error in both codes reaches order unity before the end of the integration. Using 300 force evaluations per orbit reduces the phase errors to reasonable values; the results of these simulations are plotted in Figure 2.2. Here RKNB3D exhibits less error overall as well as a similar rate of accumulation as Mercury. This improvement is likely due to the ability of RKNB3D to spend extra computational time resolving the periapse passage of the asteroid, and less time integrating the weaker perturbations at apoapse.

Our final test is a simulation of two very small protoplanets separated by about 10 Hill radii. The relative motion between these two protoplanets is slow since their orbital periods are almost equal. Their interactions occur only during conjunctions, otherwise the acceleration each provides on the other is very weak and changes very slowly. The adaptive time steps of our scheme are enormously beneficial to this configuration. The two protoplanets have mass ratios of $\mu = 10^{-12}$ of the central star. They initially follow circular coplanar orbits, one at 1 AU and the other separated by $x = 2\mu^{2/7}a = 0.00372759$ AU. This separation was chosen to be large enough that the dynamics were not chaotic; chaos occurs when the separation is less than about $1.3\mu^{2/7}a$ (Wisdom, 1980). As in Figures 2.1 and 2.2, a reference simulation with much higher accuracy was used as the benchmark for the eccentricity vector. In this case, our reference simulation uses 126 force evaluations per orbit on average, and the maximum step size is limited to 0.016 years. We compared this reference integration to two other simulations with different tolerances and no step size limitations.

The top panel of Figure 2.3 plots the root-mean-squared of the error in the eccentricity vector of one of the protoplanets. The two simulations use 1 and 7 force evaluations per orbit on average (solid and dashed lines respectively). When the two bodies are nearing conjunction, the time step

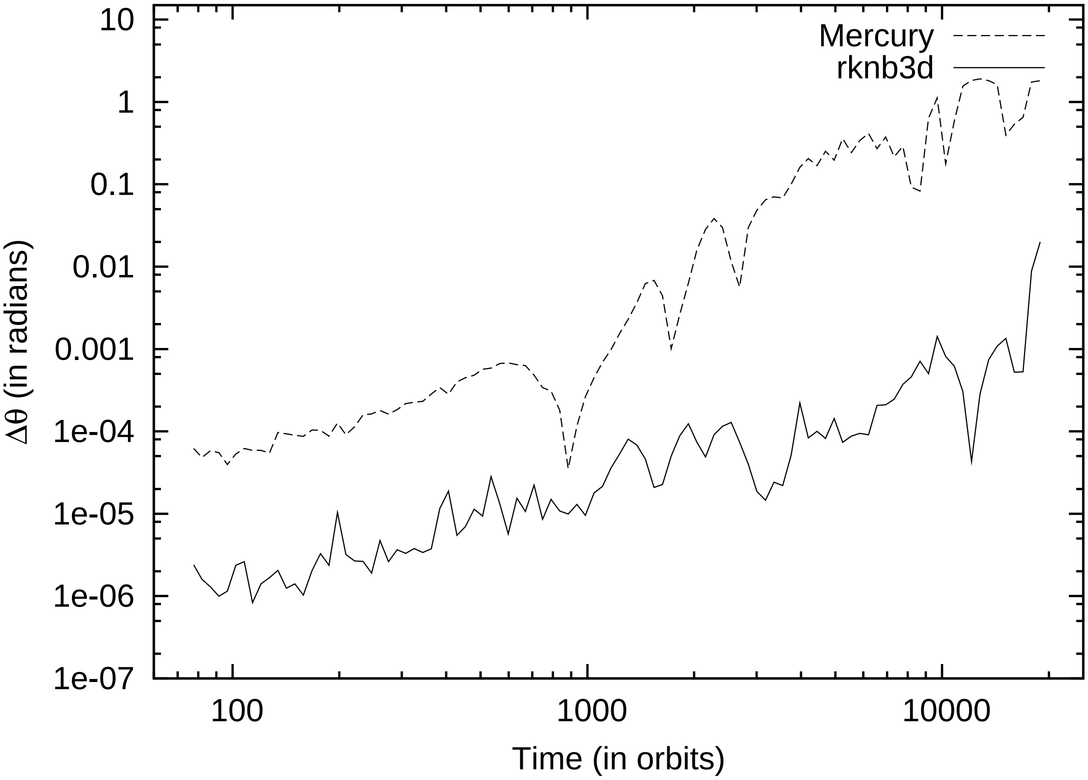

Figure 2.2 Root-mean-square error in orbital phase as a function of time for Jupiter and an asteroid with eccentricity 0.5. The solid line is the error found using RKNB3D, and the dashed is the error found using Mercury. These integrations each use, on average, 300 force evaluations per orbit.

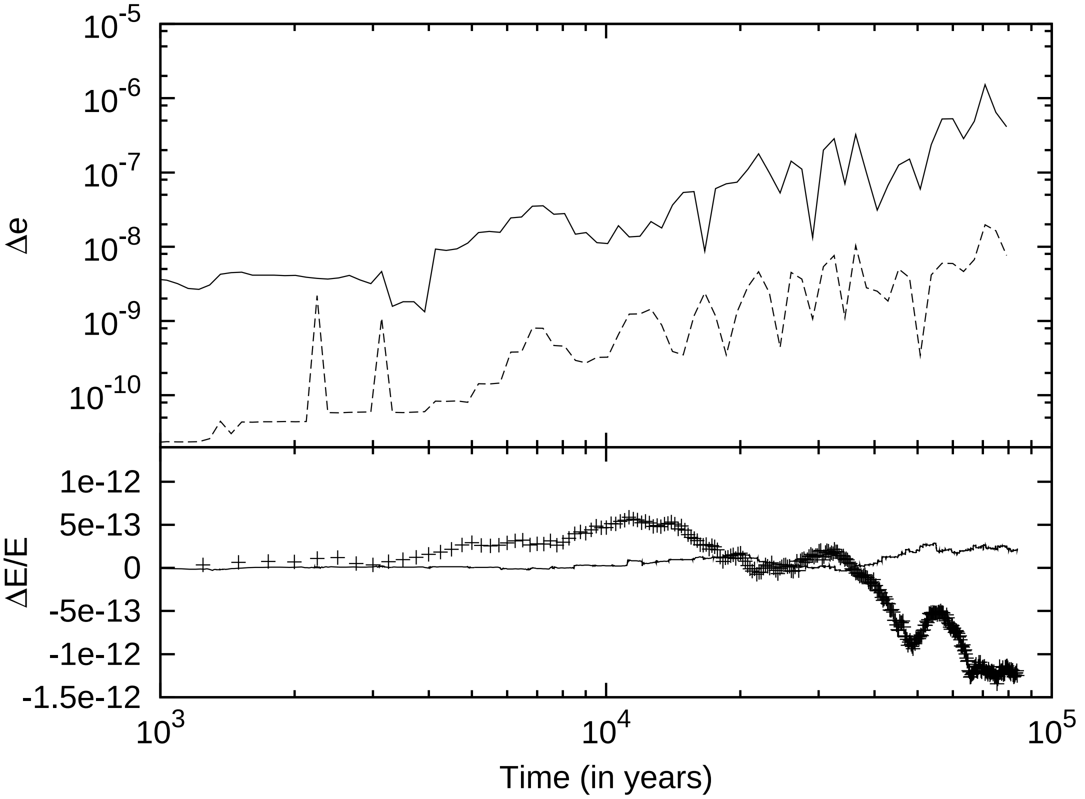

Figure 2.3 Top panel: RMS error in the eccentricity vector in integrations of two small protoplanets ($\mu = 10^{-12}$), separated by 10 R_{H}, and simulated in RKNB3D with an average of 1 and 7 force evaluations per orbit (solid and dashed, respectively). The error in the integrations was measured against a reference simulation with an average of 126 force evaluations per orbit and an enforced maximum time step of 0.016 years. Bottom panel: In the solid line, the relative change in total energy of the system in the 1 force evaluation per orbit RKNB3D simulation. The crosses show the relative energy change in a simulation with Mercury with 100 force evaluations per orbit.

decreases to between around 0.1–0.01 years; when the bodies are apart, the time steps increase to as high as 100 years for the integration shown in the solid line. The more accurate integration, shown in the dashed line, increases the step size to only 1–2 years between conjunctions.

The bottom panel of Figure 2.3 compares the total energy conservation of the system when integrated with RKNB3D to the same system integrated in Mercury. The solid line corresponds again to the RKNB3D integration with an average of 1 force evaluation per orbit. The crosses show the performance of a Mercury integration that uses 100 force evaluations per orbit. Even though both codes conserve the error well, the accuracy of RKNB3D, even when it is taking steps of up to 100 years, demonstrates the usefulness of our numerical approach.

2.5 Conclusions

In this chapter, we have outlined a new scheme for integrating the orbits of many particles around a more massive central object. We have designed this code with several optimizations for studying planet formation, such as a robust handling of close encounters between particles, and an algorithm with adaptive time steps. Tests of its performance against popular symplectic codes have showed that it is outperforms those codes in some circumstances.

Several research projects using this code have already been completed. Chapter 3 describes a numerical study of the configuration of protoplanets in a protoplanetary disk. This study benefited greatly from the ability to include arbitrary force terms in the integration. One such term was the effect of dynamical friction caused by a population of protoplanets. We also introduced a restoring force at the edges of the simulation region. By pushing the protoplanets back in as they are scattered out, we keep their surface mass density more constant.

In Chapters 4 and 5 we present an analytic technique to study the eccentricities of protoplanets. However, to confirm our results, we perform numerical integrations to measure the distribution function of the eccentricity directly. In these simulations we placed 120 particles in a small annular region, with mass ratios of 10^{-10} to 10^{-8} of the central star. With such a high number density, close encounters between protoplanets were common. The inclusion of an analytic dynamical friction term was necessary to find the steady-state distribution function of the protoplanet eccentricities. Here we take the complement of the conclusion stated in Chapter 4: the agreement of the simulations with the analytic results is a great verification of the accuracy of our numerical scheme.

Chapter 3

Co-Orbital Oligarchy

The early stages in the formation of planetary systems are well described by statistical calculations of the evolution of mass distributions and velocity dispersions. As larger bodies accumulate from the swarm of protoplanetary material, their individual dynamics begin to dominate their evolution. Lissauer (1987) pointed out that the finite crosssection for accretion limits the growth of each protoplanet. This is now known as the "oligarchic phase." (Kokubo & Ida, 1998). Numerical (Kenyon & Bromley, 2006; Ford & Chiang, 2007; Levison & Morbidelli, 2007) and analytical (Goldreich et al., 2004a) work has explored the transition from oligarchic growth to the chaotic final assembly of the planets. In this chapter we examine the interactions of a moderate number of protoplanets in an oligarchic configuration and find that neighboring protoplanets stabilize co-orbital systems of two or more protoplanets. We present a new picture of oligarchy in which each part of the disk is not ruled by one but by several protoplanets having almost the same semimajor axis.

Our approach is to systematize the interactions between each pair of protoplanets in a disk where a swarm of small icy or rocky bodies, the planetesimals, contain most of the mass. The planetesimals provide dynamical friction that circularizes the orbits of the protoplanets. The total mass in planetesimals at this stage is more than that in protoplanets so dynamical friction balances the excitations of protoplanets' eccentricities. We characterize the orbital evolution of a protoplanet as a sequence of interactions occurring each time it experiences a conjunction with another protoplanet. The number density of protoplanets is low enough that it is safe to neglect interactions among three or more protoplanets.

To confirm our description of the dynamics and explore its application to more realistic protoplanetary situations we perform many numerical N-body integrations. We use an algorithm optimized for mostly circular orbits around a massive central body. As integration variables we choose six constants of the motion of an unperturbed Keplerian orbit. As the interactions between the other bodies in the simulations are typically weak compared to the central force, the variables evolve slowly. We employ a fourth-order Runge-Kutta integration algorithm with adaptive time steps (Press et al., 1992) to integrate the differential equations. During periods of little interaction, the slow evolution of our variables permits large time-steps.

During a close encounter, the interparticle gravitational attraction becomes comparable to the

---

These results were previously published as Collins, B. F., & Sari, R. 2009, AJ, 137, 3778.

force from the central star. In the limit that the mutual force between a pair of particles is much stronger than the central force, the motion can be more efficiently described as a perturbation of the two-body orbital solution of the bodies around each other. We choose two new sets of variables: one to describe the orbit of the center of mass of the pair around the central star, and another for relative motion of the two interacting objects. These variables are evolved under the influence of the remaining particles and the central force from the star.

Dynamical friction, when present in the simulations, is included with an analytic term that damps the eccentricities and inclinations of each body with a specified timescale. All of the simulations described in this chapter were performed on Caltech's Division of Geological and Planetary Sciences Dell cluster.

We review some basic results from the three-body problem in Section 3.1 and describe the modifications of these results due to eccentricity dissipation. In Section 3.2, we generalize the results of the three-body case to an arbitrary number of bodies, and show the resulting formation and stability of co-orbital subsystems. Section 3.3 demonstrates that an oligarchic configuration with no initial co-orbital systems can acquire such systems as the oligarchs grow. Section 3.4 describes our investigation into the properties of a co-orbital oligarchy, and Section 3.5 places these results in the context of the final stages of planet formation. The conclusions are summarized in Section 3.6.

3.1 The Three-Body Problem

The circular-restricted planar three-body problem refers to a system of a zero mass test particle and two massive particles on a circular orbit. We call the most massive object the star and the other the protoplanet. The mass ratio of the protoplanet to the star is μ. Their orbit has a semimajor axis a and an orbital frequency Ω. The test particle follows an initially circular orbit with a semimajor axis $a_{\rm tp} = a(1+x)$ with $x \ll 1$. Since the semimajor axes of the protoplanet and the test particle are close, the two objects rarely approach each other. For small x, the angular separation between the two bodies changes at the rate $(3/2)\Omega x$ per unit time. Changes in the eccentricity and semimajor axis of the test particle occur only when it reaches conjunction with the protoplanet.

The natural scale for xa is the Hill radius of the protoplanet, $R_{\rm H} \equiv (\mu/3)^{1/3}a$. For interactions at impact parameters larger than about 4 Hill radii, the effects of the protoplanet can be treated as a perturbation to the Keplerian orbit of the test particle. These changes can be calculated analytically. To first order in μ, the change in eccentricity is $e_k = A_k \mu x^{-2}$, where $A_k = (8/9)[2K_0(2/3) + K_1(2/3)] \approx 2.24$ and K_0 and K_1 are modified Bessel functions of the second kind (Goldreich & Tremaine, 1978; Petit & Henon, 1986).

The change in semimajor axis of the test particle can be calculated from an integral of the motion, the Jacobi constant: $C_{\rm J} \equiv E - \Omega H$, where E and H and are, respectively, the energy and angular momentum per unit mass of the test particle. Rewriting C_{J} in terms of x and e, we find that

$$\frac{3}{4}x^2 - e^2 = \text{ const.} \tag{3.1}$$

If the encounter increases e, $|x|$ must also increase. The change in x resulting from a single interaction on an initially circular orbit is

$$\Delta x = (2/3)e_k^2/x = (2/3)A_k^2\mu^2 x^{-5}. \tag{3.2}$$

The contributions of later conjunctions add to the eccentricity as vectors and do not increase the magnitude of the eccentricity by e_k. Because of this, the semimajor axis of the test particle generally does not evolve further than the initial change Δx. Two alternatives are if the test particle is in resonance with the protoplanet, or if its orbit is chaotic. If the test particle is in resonance, the eccentricity of the particle varies as it librates. Chaotic orbits occur when each excitation is strong enough to change the angle of the next conjunction substantially; in this case, e and x evolve stochastically (Wisdom, 1980; Duncan et al., 1989).

Orbits with x between 2 and 4 R_{H}/a can penetrate the Hill sphere and experience large changes in e and a. This regime is highly sensitive to initial conditions, so we only offer a qualitative description. Particles on these orbits tend to receive eccentricities of the order of the Hill eccentricity, $e_{\mathrm{H}} \equiv R_{\mathrm{H}}/a$, and accordingly change their semimajor axes by $\sim R_{\mathrm{H}}$. We will call this the "strong-scattering regime" of separations. A fraction of these trajectories collide with the protoplanet; these orbits are responsible for protoplanetary accretion (Greenzweig & Lissauer, 1990; Dones & Tremaine, 1993).

For $x \lesssim R_{\mathrm{H}}/a$, the small torque from the protoplanet is sufficient to cause the particle to pass through $x = 0$. The particle then returns to its original separation on the other side of the protoplanet's orbit. These are the famous horseshoe orbits that are related to the 1:1 mean-motion resonance. The change in eccentricity from an initially circular orbit that experiences this interaction can be calculated analytically (Petit & Henon, 1986): $e_k = 2^{2/3}3^{-3/2}5\Gamma(2/3)\mu^{1/3}\exp(-(8\pi/9)\mu x^{-3})$, where $\Gamma(2/3)$ is the usual gamma function. Since this interaction is very slow compared to the orbital period, the eccentricity change is exponentially small as the separation goes to zero. As in the case of the distant encounters, the conservation of the Jacobi constant requires that x increases as the eccentricity increases (equation 3.1). Then,

$$\Delta x = 2.83\frac{\mu^{2/3}}{x}\exp(-5.58\mu x^{-3}). \tag{3.3}$$

To apply these results to protoplanetary disks, we must allow the test particle to have mass. We now refer to both of the bodies as protoplanets, each having mass ratios with the central object of μ_1 and μ_2. The change in their total separation after one conjunction is given by equations 3.2 and

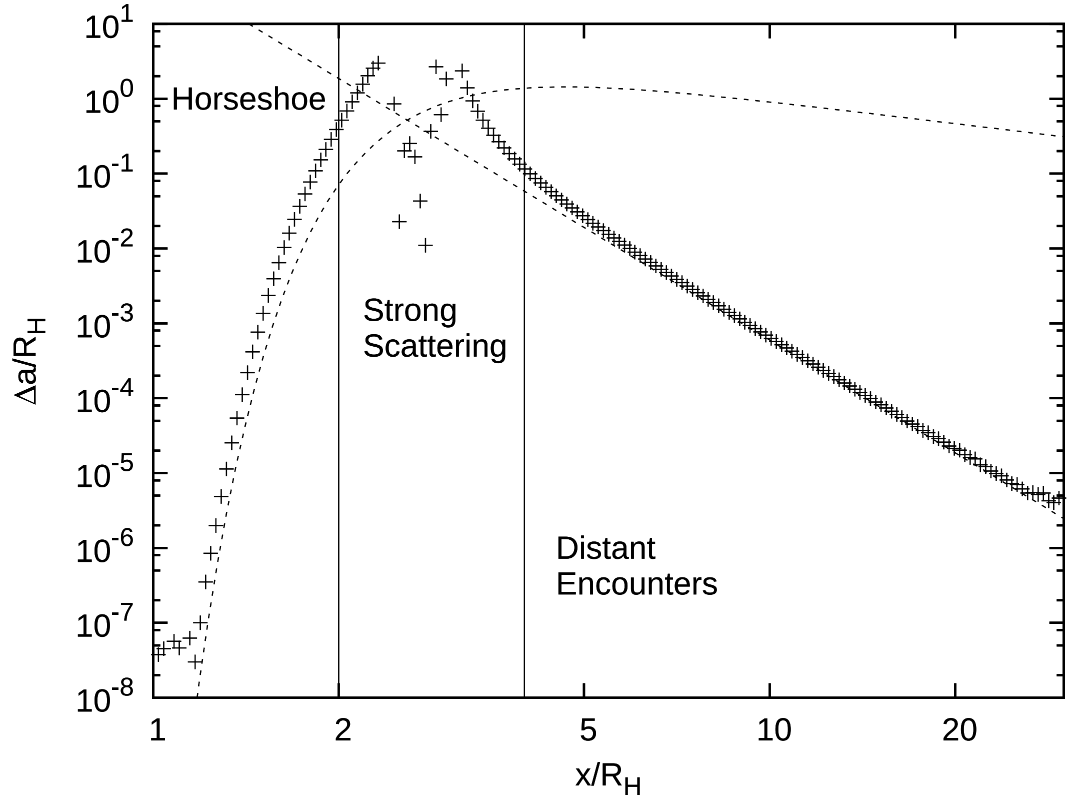

Figure 3.1 Change in semimajor axis after a conjunction of two bodies on initially circular orbits whose masses are smaller than that of the star by the ratio $\mu = 3 \times 10^{-9}$, plotted as a function of the initial separation. The points are calculated with numerical integrations, while the dashed lines show the analytic results, equations 3.2 and 3.3. At the smallest impact parameters the bodies switch orbits; in this case we have measured the change relative to the initial semimajor axis of the other protoplanet. The horizontal lines separate the regions of x that are referred to in the text.

3.3 with $\mu = \mu_1 + \mu_2$.

Figure 3.1 plots the change in a after one conjunction of two equal mass protoplanets as measured from numerical integrations. All three types of interactions described above are visible in the appropriate regime of x. Each point corresponds to a single integration of two bodies on initially circular orbits separated by x. For the horseshoe-type interactions, each protoplanet moves a distance almost equal to x; we only plot the change in separation: $\Delta a_{\mathrm{H.S.}} = |\Delta a| - |x|a$. The regimes of the three types of interactions are marked in the figure. The dashed line in the low x regime plots the analytic expression calculated from equation 3.3. The separations that are the most strongly scattered lie between $2 - 4R_{\mathrm{H}}$, surrounding the impact parameters for which collisions occur. For larger separations the numerical calculation approaches the limiting expression of equation 3.2, which is plotted as another dashed line.

The sea of planetesimals modifies the dynamics of the protoplanets. If the planetesimals have radii less than ~ 1 km, their own collisions balance the excitations caused by the protoplanets.

At the same time, the planetesimals provide dynamical friction that damps the eccentricities of the protoplanets. When the typical eccentricities of the protoplanets and the planetesimals are lower than the Hill eccentricity of the protoplanets, this configuration is said to be shear dominated: the relative velocity between objects is set by the difference between the orbital frequency of nearby orbits. In the shear-dominated eccentricity regime, the rate of dynamical friction is (Goldreich et al., 2004b):

$$-\frac{1}{e}\frac{de}{dt} = C_d \frac{\sigma\Omega}{\rho R}\alpha^{-2} = \frac{1}{\tau_{\mathrm{d}}}, \tag{3.4}$$

where R and ρ are the radius and density of a protoplanet, σ is the surface mass density in planetesimals, α is the ratio R/R_{H}, and C_d is a dimensionless coefficient of order unity. Recent studies have found values for C_d between 1.2 and 6.2 (Ohtsuki et. al. 2002; H. Schlichting and R. Sari, private communication). For this work, we use a value of 1.2. For parameters characteristic of the last stages of planet formation, $\tau_d \gg 2\pi/\Omega$. The interactions of the protoplanets during an encounter are unaffected by dynamical friction and produce the change in e and a as described above. In between protoplanet conjunctions, the dynamical friction circularizes the orbits of the protoplanets. The next encounter that increases e further increases x to conserve the Jacobi constant. The balance between excitations and dynamical friction keeps the eccentricities of the protoplanets bounded and small, but their separation increases after each encounter. This mechanism for orbital repulsion has been previously identified by Kokubo & Ida (1995), who provide a timescale for this process. We alternatively derive the timescale by treating the repulsion as a type of migration in semimajor axis. The magnitude of the rate depends on the strength of the damping; it is maximal if all the eccentricity is damped before the next encounter, or $\tau_d \ll 4\pi/(3\Omega x)$. In this case, a protoplanet with a mass ratio μ_1 and semimajor axis a_1 interacting with a protoplanet with a mass ratio μ_2 in the regime of distant encounters is repelled at the rate:

$$\frac{1}{a_1}\frac{da_1}{dt} = \frac{A_k^2}{2\pi}\mu_2(\mu_1+\mu_2)x^{-4}\Omega. \tag{3.5}$$

For protoplanets in the horseshoe regime, the repulsion of each interaction is given by equation 3.3. These encounters increase the separation at an exponentially slower rate of:

$$\frac{1}{a_1}\frac{da_1}{dt} = 0.67\mu_2(\mu_1+\mu_2)^{-2/3}\exp(-5.58(\mu_1+\mu_2)x^{-3})\Omega. \tag{3.6}$$

If instead $\tau_d \gg 4\pi/(3\Omega x)$, the eccentricity of the protoplanet is not completely damped away before the next conjunction restores the protoplanet to $e \sim e_k$. The rate at which the separation increases is then related to the rate of dynamical friction, $\dot{a} \propto e_k\dot{e}/x$. Qualitatively, this rate is slower than those of equations 3.5 and 3.6 by $(\tau_d\Omega x)^{-1}$. We focus on the maximally damped case where $\tau_d \ll 4\pi/(3\Omega x)$.

3.2 The Damped N-Body Problem

Having characterized the interactions between pairs of protoplanets, we next examine a disk of protoplanets with surface mass density Σ. Each pair of protoplanets interacts according to their separations as described in Section 3.1. If the typical spacing is of order $R_{\rm H}$, the closest encounters between protoplanets cause changes in semimajor axes of about $R_{\rm H}$ and eccentricity excitations to $e_{\rm H}$. The strong scatterings may also cause the two protoplanets to collide. If the planetesimals are shear dominated and their mass is greater than the mass in protoplanets, the eccentricities of the protoplanets are held significantly below $e_{\rm H}$ by dynamical friction (Goldreich et al., 2004b), and the distribution of their eccentricities can be calculated analytically (Collins & Sari, 2006; Collins et al., 2007). If the scatterings and collisions rearrange the disk such that there are no protoplanets with separations of about $2 - 4R_{\rm H}$, the evolution is subsequently given by only the gentle pushing of distant interactions (Kokubo & Ida, 1995). However, there is another channel besides collisions through which the protoplanets may achieve stability: achieving a semimajor axis very near that of another protoplanet.

A large spacing between two protoplanets ensures that they will not strongly-scatter each other. However, a very small difference in their semimajor axes can also provide this safety (see Figure 3.1 and Equation 3.6). Protoplanets separated by less than $2R_{\rm H}$ provide torques on each other during an encounter that switch their semimajor axes and reverse their relative angular motion before they can get very close. Their mutual interactions are also very rare, since their relative orbital frequency is proportional to their separation. Protoplanets close to co-rotation are almost invisible to each other; however, these protoplanets experience the same $\dot{a}/a$ from the farther protoplanets as given by equation 3.5. We call the group of the protoplanets with almost the same semimajor axis a "co-orbital group" and use the label N to refer to the number of protoplanets it contains. The protoplanets within a single group can have any mass, although for simplicity in the following discussion we assume equal masses of each.

Different co-orbital groups repel each other at the rate of equation 3.5. For equally spaced rows of the same number of equal mass protoplanets, the migration caused by interior groups in the disk exactly cancels the migration caused by the exterior groups. We say that the protoplanets in this configuration are separated by their "equilibrium spacing." We define a quantity, y, to designate the distance between a single protoplanet and the position where it would be in equilibrium with the interior and exterior groups. The near cancellation of the exterior and interior repulsions decreases y, pushing displaced protoplanets toward their equilibrium spacing. The migration rate of a single protoplanet near the equilibrium spacing of its group can be calculated by expanding equation 3.5

to first order in y and taking the difference between interior and exterior contributions:

$$\frac{1}{y}\frac{dy}{dt} \approx \frac{a}{y}\sum_{i=1}^{\infty} 8N\frac{\dot{a}}{a}\frac{y}{ix\ a} \approx 131N\left(\frac{x\ a}{R_{\rm H}}\right)^{-5} e_{\rm H}\Omega, \tag{3.7}$$

where we assume that the other co-orbital groups in the disk are regularly spaced by $\Delta a = x\ a$ and contain N protoplanets of a single mass ratio. Each term in the summation represents a pair of neighboring groups for which $\dot{a}$ is evaluated at the unitless separation ix. Since the repulsion rate is a sharp function of the separation, the nearest neighbors dominate. The coefficient in equation 3.7 takes a value of 121 when only the closest neighbors are included ($i = 1$ only). Including an infinite number of neighbors increases the coefficent by a factor of $1 + 2^{-5} + 3^{-5} + \cdots$, only about 8 %.

The above dynamics describe an oligarchic protoplanetary disk as a collection of co-orbital groups each separated by several Hill radii. It is necessary though to constrain such parameters as the typical spacing between stable orbits and the relative population of co-orbital systems. To determine these quantities, we perform full numerical integrations. Given a set of initial conditions in the strong-scattering regime, what is the configuration of the protoplanets when they reach a stable state?

We have simulated an annulus containing 20 protoplanets, each with a mass ratio of $\mu = 1.5\times10^{-9}$ to the central star. The protoplanets start on circular orbits spaced uniformly in semimajor axis. We dissipate the eccentricities of the protoplanets on a timescale of 80 orbits; for parameters in the terrestrial region of the solar system and using $C_d = 1.2$, this corresponds to a planetesimal mass surface density of about 8 g cm^{-2}. We allow the protoplanets to collide with each other setting $\alpha^{-1} = 227$; this corresponds to a density of 5 g cm^{-3}.

We examine two initial compact separations: 1.0 $R_{\rm H}$ (set A) and 2.5 $R_{\rm H}$ (set B). For each initial separation, we run 1000 simulations starting from different randomly chosen initial phases. After 6×10^3 orbital periods the orbits of the protoplanets have stabilized and we stop the simulations. To determine the configuration of the protoplanets, we write an ordered list of the semimajor axis of the protoplanets in each simulation. We then measure the separation between each adjacent pair of protoplanets (defined as a positive quantity). If the semimajor axes of two or more protoplanets are within 2 $R_{\rm H}$, we assume that they are part of the same co-orbital group. The average semimajor axis is calculated for each group. We call the distance of each member of a group from the average semimajor axis the “intra-group separation.” These values can be either positive or negative and, for the co-orbital scenarios we are expecting, are typically smaller than $1R_{\rm H}$.

When one protoplanet is more than 2 $R_{\rm H}$ from the next protoplanet, we assume that the next protoplanet is either alone or belongs to the next co-orbital group. We call the spacing between the average semimajor axis of one group and the semimajor axis of the next protoplanet or co-orbital group the “inter-group spacing.” These separations are by definition positive.

Finally we create a histogram of both the intragroup separations and the intergroup separations

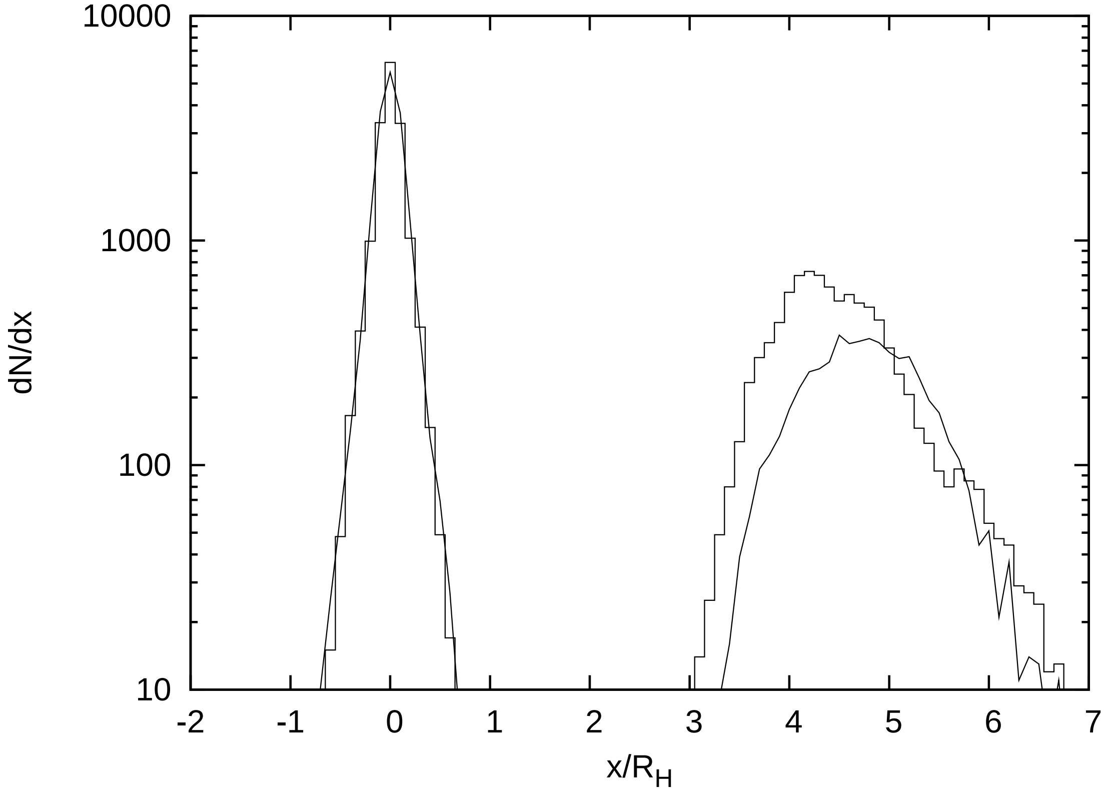

Figure 3.2 Histogram of the intragroup and intergroup separations between protoplanets in two sets of numerical simulations. Each simulation integrates 20 protoplanets with mass ratios of 3×10^{-9} compared to the central mass. They begin on circular orbits with uniform separations in semimajor axis; each set of simulations consists of 1000 integrations with random initial phases. The eccentricities of the protoplanets are damped with a timescale of 80 orbits. The smooth line represents the simulations of set A, with an initial spacing of 1.0 R_{H}, and the stepped line shows simulations of set B, which have an initial spacing of 2.5 R_{H}.

of all the simulations in the set. For reference, the initial configuration of the simulations of set B contains no co-orbital groups. The resulting histogram would depict no intragroup separations, and have only one nonzero bin representing the intergroup separations of $x = 2.5 R_{\mathrm{H}}$.

Figure 3.2 shows the histograms of the final spacings of the two sets of simulations. The spacings in set A are shown in the smooth line, and those of set B are shown in the stepped line. The initial closely spaced configurations did not survive. The distributions plotted in Figure 3.2 reveal that none of the spacings between neighboring protoplanets are in the strong scattering regime, since it is unstable. This validates the arbitrary choice of 2 R_{H} as the boundary in the construction of figure 2; any choice between 1 and 3 R_{H} would not affect the results.

The size of the peak of intragroup spacings shows that most of the protoplanets in the disk are co-orbital with at least one other body. The shape shows that the spread in the semimajor axes of each co-orbital group is small. This is consistent with equation 3.7, since the endpoint of these simulations is late enough to allow significant co-orbital shrinking. The second peak in Figure 3.2 represents the intergroup separation. The median intergroup separation in the two sets are $4.8R_{\rm H}$ and $4.4R_{\rm H}$. This is much less than the $10R_{\rm H}$ usually assumed for the spacing between protoplanets in oligarchic planet formation (Kokubo & Ida, 1998, 2002; Thommes et al., 2003; Weidenschilling, 2005).

Figure 3.2 motivates a description of the final configuration of each simulation as containing a certain number of co-orbital groups that are separated from each other by $4-5R_{\rm H}$. Each of these co-orbital groups is further described by its occupancy number N. For the simulations of set A, the average occupancy $\langle N\rangle = 2.8$, and for set B, $\langle N\rangle = 1.8$. Since the simulated annulus is small, the co-orbital groups that form near the edge are underpopulated compared to the rest of the disk. For the half of the co-orbital groups with semimajor axes closest to the center of the annulus, $\langle N\rangle$ is higher: $\langle N\rangle = 3.5$ for set A and $\langle N\rangle = 2.0$ for set B.

3.3 Oligarchic Planet Formation

The simulations of Section 3.2 demonstrate the transition from a disordered swarm of protoplanets to an orderly configuration of co-orbital rows, each containing several protoplanets. The slow accretion of planetesimals onto the protoplanets causes an initially stable configuration to become unstable. The protoplanets stabilize by reaching a new configuration with a different average number of co-orbital bodies. To demonstrate this process we simulate a disk of protoplanets and allow accretion of the planetesimals.

We use initial conditions similar to the current picture of a disk with no co-orbital protoplanets, placing 20 protoplanets with mass ratios $\mu = 3\times10^{-9}$ on circular orbits spaced by $5R_{\rm H}$. This spacing is the maximum impact parameter at which a protoplanet can accrete a planetesimal (Greenberg et al., 1991) and a typical stable spacing between oligarchic zones (Figure 3.2). For the terrestrial region around a solar-mass star, this mass ratio corresponds to protoplanets of mass 6×10^{24} g, far below the final expected protoplanet mass (see Section 3.5). Our initial configuration has no co-orbital systems. We include a mass growth term in the integration to represent the accretion of planetesimals onto the protoplanets in the regime where the eccentricity of the planetesimals e_p obeys $\alpha^{1/2}e_{\rm H} < e_p < e_{\rm H}$ (Dones & Tremaine, 1993):

$$\frac{1}{M}\frac{dM}{dt} = 2.4\frac{\sigma\Omega}{\rho R}\frac{1}{\alpha}\frac{e_{\rm H}}{e_p}. \tag{3.8}$$

Protoplanet-protoplanet collisions are allowed. For simplicity we assume that the planetesimal disk does not evolve in response to the protoplanets. Eccentricity damping of the protoplanets from dynamical friction of the planetesimals is included. The damping timescale, 80 orbits, and growth timescale, 4800 orbits, correspond to a planetesimal surface density of 10 g cm^{-2} and a typical

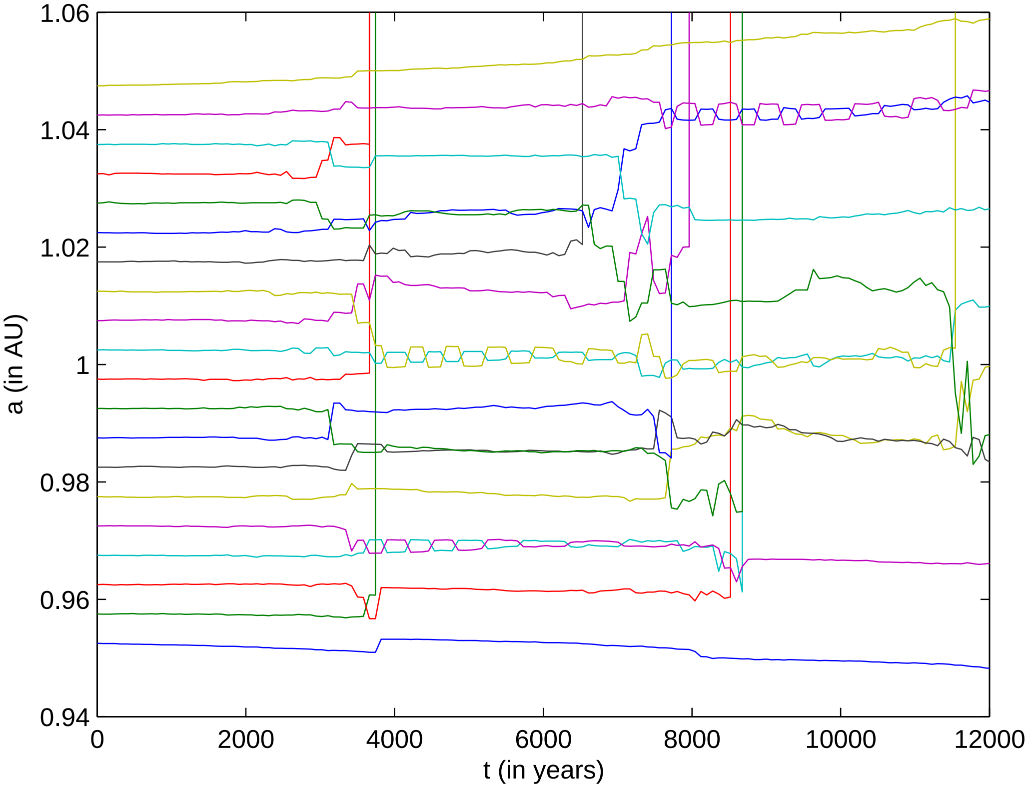

Figure 3.3 Semimajor axes of the protoplanets vs. time in a simulation of oligarchic growth around a solar-mass star. The initial mass of each protoplanet is 6×10^{24} g and each is spaced 5 $R_{\rm H}$ from its nearest neighbor. The planetesimals have a surface density of 10 g cm^{-2} and an eccentricity $e_p = 5 \times 10^{-4}$. These parameters correspond to a damping timescale of 80 years and a growth timescale of 4800 years. The sharp vertical lines indicate a collision between two bodies; the resulting protoplanet has the sum of the masses and a velocity chosen to conserve the linear momentum of the parent bodies.

planetesimal eccentricity of $e_p = 5 \times 10^{-4}$. We have again used the value $C_d = 1.2$. These parameters imply a planetesimal radius of ~ 100 m, assuming that the planetesimal stirring by the protoplanets is balanced by physical collisions. Each protoplanet has a density of 5 g cm^{-3}. The annulus of bodies is centered at 1 AU. We simulate 1000 systems, each beginning with different randomly chosen orbital phases. Figure 3.3 shows the evolution of the semimajor axis of the protoplanets in one of the simulations as a function of time; other simulations behave similarly.

If there were no accretion, the protoplanets would preserve their original spacing indefinitely, aside from a slow spreading at the edges of the annulus. However, the spacing in units of Hill radii decreases as the protoplanets grow. Eventually their interactions become strong enough to cause collisions and large scatterings. This epoch of reconfiguration occurs after a time of approximately 4000 orbits in the simulation plotted in Figure 3.3. At this point the mass of protoplanets has increased by roughly a factor of 2.3, meaning that the spacing in units of Hill radii has decreased by a factor of 1.3. We would expect the chaotic reconfiguration to restore the typical spacing to about $5R_{\rm H}$ by reducing the number of oligarchic zones. The figure, in fact, shows 13 zones after the first reconfiguration, compared to 20 before. Three protoplanets have collided and four have formed co-orbital groups of $N = 2$. The co-orbital pairs are visibly tightened over the timescale predicted by equation 3.7, which for the parameters of this simulation is about $\Delta t \approx 3 \times 10^3$ years. The configuration is then stable until the growth of the bodies again lowers their separation into the strong-scattering regime at a time of 1.1×10^4 years.

The other realizations of this simulation show similar results. We find an average co-orbital population of $\langle N \rangle = 1.2$ in the middle of the annulus after the first reconfiguration. This value is lower than that found in Section 3.2 because the protoplanets begin to strongly scatter each other when they are just closer than the stable spacing. Only a few protoplanets can collide or join a co-orbital group before the disk becomes stable again. As described in the paradigm of Kokubo & Ida (1995), a realistic protoplanetary disk in the oligarchic phases experiences many such epochs of instability as the oligarchs grow to their final sizes.

3.4 The Equilibrium Co-Orbital Number

As the protoplanets evolve, they experience many epochs of reconfiguration that change the typical co-orbital number. The examples given in previous sections of this chapter show the result of a single reconfiguration. Our choices of initial conditions with the initial co-orbital number $\langle N \rangle_i = 1$ have resulted in a higher final co-orbital number $\langle N \rangle_f$. If instead, $\langle N \rangle_i$ is very high, the final co-orbital number must decrease. As the disk evolves, $\langle N \rangle$ is driven to an equilibrium value where each reconfiguration leaves $\langle N \rangle$ unchanged. This value, $\langle N \rangle_{\rm eq}$, is the number that is physically relevant to the protoplanetary disk.

We use a series of simulations to determine $\langle N \rangle_{\rm eq}$ at a fixed value of Σ and σ. Each individual simulation contains 40 co-orbital groups separated by 4 $R_{\rm H}$. This spacing ensures that each simulation experiences a chaotic reconfiguration. The number of oligarchs in each group is chosen randomly to achieve the desired $\langle N \rangle_i$. All oligarchs begin with $e = e_{\rm H}$ and $i = i_{\rm H}$ to avoid the maximal collision rate that occurs if $e < \alpha^{1/2} e_{\rm H}$ (Goldreich et al., 2004b). The initial orbital phase, longitude of periapse, and line of nodes are chosen randomly. We set a lower limit to the allowed inclination to prevent it from being damped to unreasonably small values. The results of the simulations are insensitive to the value of this limit if it is smaller than $i_{\rm H}$; we choose 10^{-3} $i_{\rm H}$.

We include an additional force in the simulations to prevent the initial annulus from increasing in width. This extra force pushes the semimajor axis of a protoplanet back into the annulus at a specified timescale. We choose this timescale to be longer than the typical time between encounters,

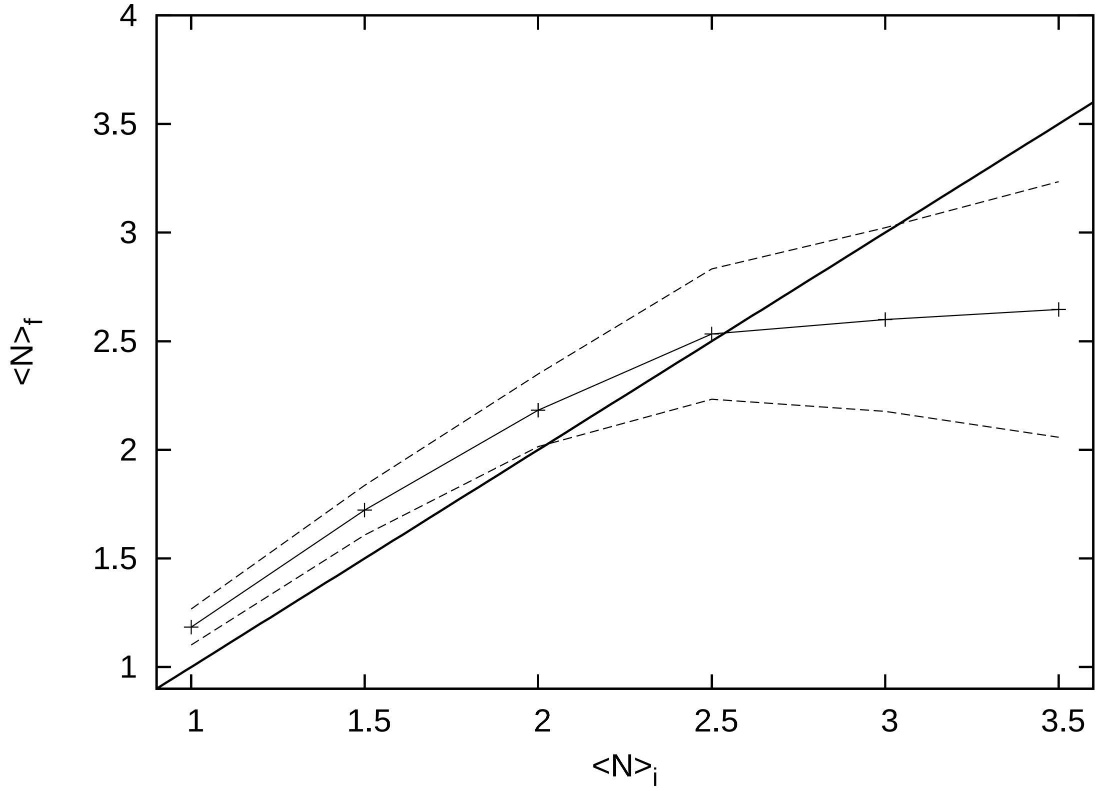

Figure 3.4 Final $\langle N \rangle$ of simulations against the initial $\langle N \rangle$ for $\Sigma = 0.9$ g cm^{-2} and $\sigma = 9.1$ g cm^{-2}. For each value of $\langle N \rangle_i$ the mass of each protoplanet is adjusted to keep Σ constant. The dashed lines denote the average value plus and minus one standard deviation of the measurements. The solid line illustrates where $\langle N \rangle_i = \langle N \rangle_f$.

$(\Omega x)^{-1}$, so that multiple protoplanets are not pushed to the boundary of the annulus without having the chance to encounter a protoplanet a few Hill radii away. Collisions between protoplanets are allowed, but the protoplanets are not allowed to accrete the planetesimals. Each simulation is stopped when there has not been a close encounter for 1.6×10^4 orbits. Inspection of the simulation results reveals that this stopping criterion is sufficient for the disk to have reached an oligarchic state. We measure the final semimajor axes of the protoplanets to determine N for each co-orbital group. For each set of parameters (Σ, σ, and $\langle N \rangle_i$), we perform 100 simulations.

The numerical values we have chosen for these simulations reflect planet formation in the terrestrial region. We center the annulus of the simulations at 1 AU. We adopt the minimum mass solar nebula for total mass of solids in the annulus, $\Sigma + \sigma = 10$ g cm^{-2} (Hayashi, 1981), and keep this value fixed throughout all the simulations. Figure 3.4 plots the results of simulations for $\Sigma/\sigma = 1/10$. The points connected by the solid line show the average $\langle N \rangle_f$ of each set of simulations, while the dashed lines show the average value plus and minus one standard deviation of those measurements. For reference, we plot another solid line corresponding to $\langle N \rangle_i = \langle N \rangle_f$. The points at low $\langle N \rangle_i$

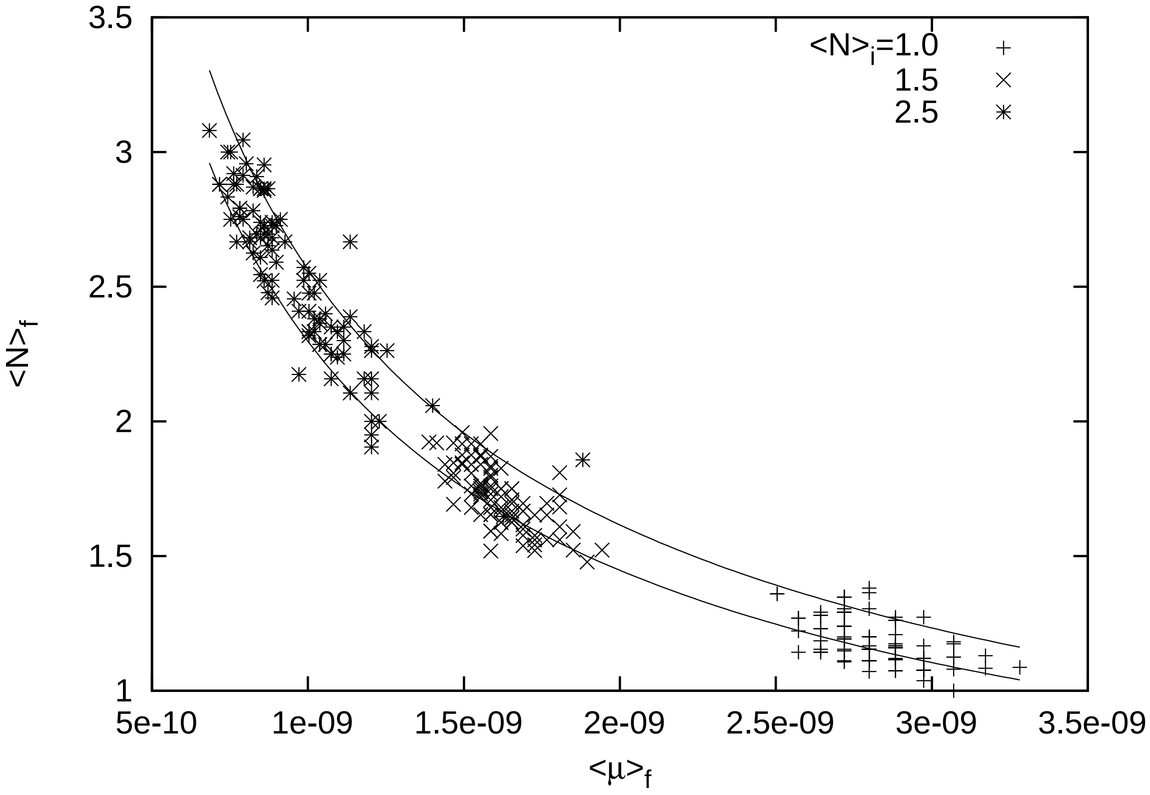

Figure 3.5 Final average mass ratio, $\langle\mu\rangle$, of the protoplanets plotted against the final $\langle N\rangle$ for the ratio of surface densities of $\Sigma/\sigma = 1/10$. Each symbol corresponds to a value of $\langle N\rangle_i$. The solid lines plot lines of constant Σ for values of $\langle x\rangle$ one standard deviation away from the best-fit curve of constant Σ to the simulations with $\langle N\rangle_i = 2.5$.

show a similarity to the results of the simulations of Sections 3.2 and 3.3: stability is reached by increasing the number of oligarchs in each co-orbital group. Once $\langle N\rangle_i$ is too high, the chaotic reconfiguration results in an oligarchy with lower $\langle N\rangle$. Figure 3.4 depicts a feedback cycle that drives $\langle N\rangle$ toward an equilibrium value that remains unchanged by a reconfiguration. For $\Sigma/\sigma = 1/10$, we find $\langle N\rangle_{\rm eq} \approx 2.5$. The intersection of the dotted lines with $\langle N\rangle_i = \langle N\rangle_f$ yields the one standard deviation range of $\langle N\rangle_{\rm eq}$, $2 - 3.2$.

The cause of the wide distribution of each $\langle N\rangle_f$ is evident from Figure 3.5. In this figure, we plot the values of $\langle N\rangle_f$ against the average mass of each protoplanet in the same simulations of $\Sigma/\sigma = 1/10$. All of the points lie near a single line of $\langle N\rangle_f \propto \langle\mu\rangle^{-2/3}$. This relation is derived from the definition $\Sigma = N m_p/(2\pi\Delta a a)$. We find the relation

$$\langle N\rangle = \frac{2\pi a^2\Sigma}{3^{1/3}M_\odot}\langle x_H\rangle\langle\mu\rangle^{-2/3}, \tag{3.9}$$

where we have defined $x_{\rm H}$ to be dimensionless and equal to $\Delta a/R_{\rm H}$. While the points in Figure 3.5 generally follow the function given by equation 3.9, there is significant scatter. We interpret

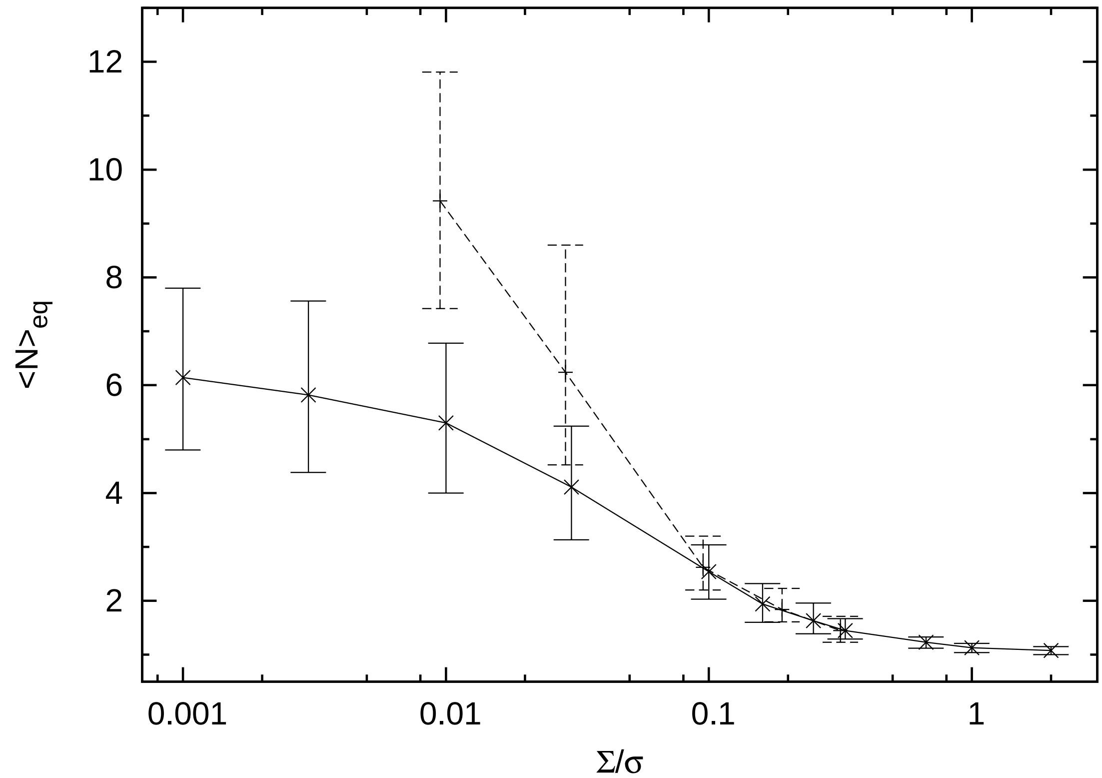

Figure 3.6 Equilibrium average co-orbital number $\langle N\rangle_{\rm eq}$ plotted against the surface mass density ratio of protoplanets to planetesimals, Σ/σ. The error bars represent the standard deviation of $\langle N\rangle_{\rm eq}$ as defined in the text. The solid and dashed points correspond to simulations at 1 AU and 25 AU respectively. The dashed points are offset by 5 % in Σ/σ to distinguish them from the solid points.

this variation as a distribution of the average spacing between rows, $\langle x_H\rangle_f$. For the $\langle N\rangle_i = 2.5$ simulations, we measure an average $\langle x_H\rangle_f = 5.4$, with a standard deviation of 0.2. The solid lines in Figure 3.5 correspond to the lower and upper bounds of $\langle x_H\rangle_f$ given by one standard deviation from the mean. This reaffirms our earlier conclusion that the spacing between rows is an order unity number of Hill radii of an average size body.

The ratio of Σ/σ increases as the oligarchs accrete the planetesimals. To demonstrate the evolution of $\langle N\rangle_{\rm eq}$ and $\langle x_H\rangle_{\rm eq}$, we performed more simulations with values of Σ/σ in the range 0.001–2. At each value, we examine a range of $\langle N\rangle_i$ to determine $\langle N\rangle_{\rm eq}$. We plot the resulting values in Figure 3.6. The error bars on the points show where one standard deviation above and below $\langle N\rangle_f$ is equal to $\langle N\rangle_i$. As the disk evolves and Σ/σ approaches unity, $\langle N\rangle_{\rm eq}$ decreases. For high values of Σ/σ, the equilibrium co-orbital number asymptotes toward 1, its minimum value by definition.

For the simulations with $\langle N\rangle_{\rm f} = \langle N\rangle_{\rm eq} =$, we also measure the average spacing between co-orbital groups directly. The average spacing in units of the Hill radii of the average mass protoplanet,

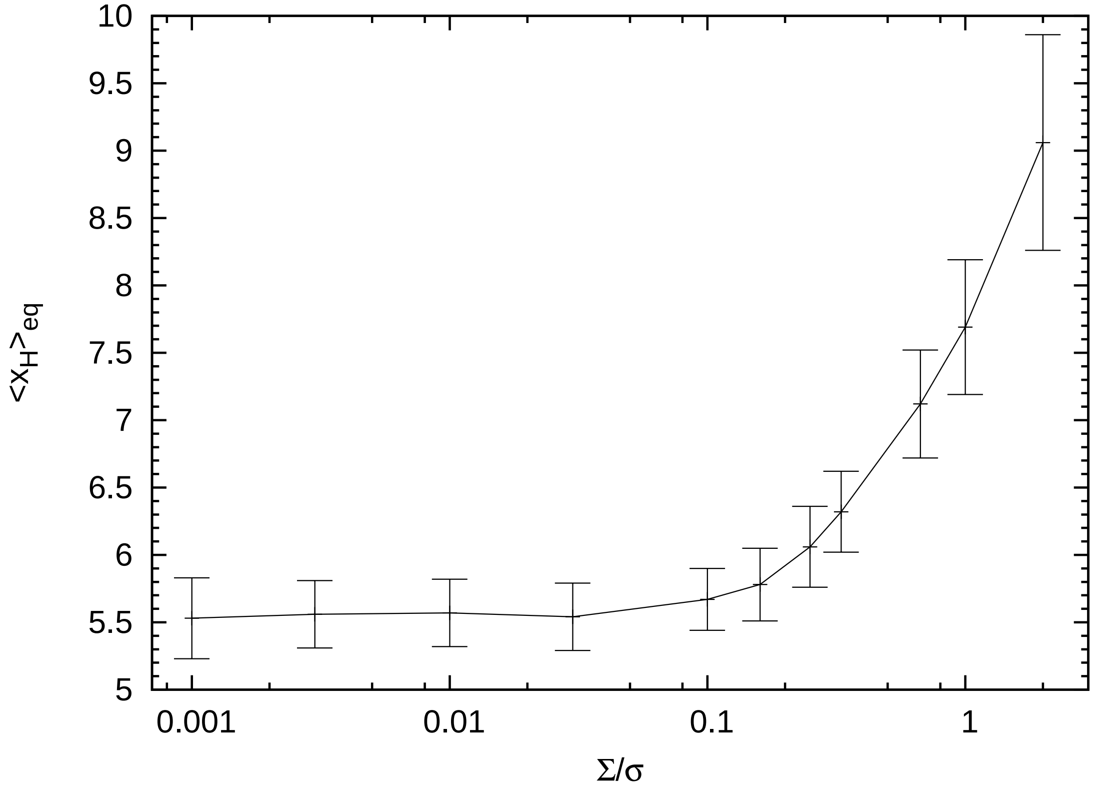

Figure 3.7 Equilibrium average spacing between co-orbital groups, $\langle x_H \rangle_{\rm eq}$ for simulations with $\langle N \rangle_i = \langle N \rangle_{\rm eq}$ plotted against the surface mass density ratio Σ/σ. The error bars reflect the standard deviation of the measurements of $\langle x_H \rangle$ of each simulation.

$\langle x_H \rangle_{\rm eq}$ is plotted against $\langle N \rangle_{\rm eq}$ in Figure 3.7. Early in the disk, when Σ/σ is very small, $\langle x_H \rangle_{\rm eq}$ is approximately constant at a value of 5.5. The average spacing grows however as Σ/σ approaches unity.

Figure 3.5 shows that all oligarchies of a fixed Σ exhibit similar average spacings $\langle x_H \rangle$. The points from simulations of different $\langle N \rangle_i$ confirm that a broad range of $\langle N \rangle$ and $\langle \mu \rangle$ can be achieved, with the relation between $\langle N \rangle$ and $\langle \mu \rangle$ given by equation 3.9. By finding the equilibrium $\langle N \rangle$ reached by the disk after many configurations, we also fix the average mass of the protoplanet, denoted by $\langle \mu \rangle_{\rm eq}$. We plot $\langle \mu \rangle_{\rm eq}/\mu_{\rm Earth}$ as a function of Σ/σ at $a = 1$ AU in Figure 3.8, where $\mu_{\rm Earth}$ is the mass ratio of the Earth to the Sun. The error bars show the standard deviation of $\langle \mu \rangle$ for the simulations with $\langle N \rangle_i = \langle N \rangle_{\rm eq}$.

For comparison, we also plot $\langle \mu \rangle$ as given by equation 3.9 for a constant $\langle N \rangle_i = 1$ and $\langle x_H \rangle = 5$. These parameters reflect the typical oligarchic picture with no co-orbital oligarchs and a fixed spacing in Hill units (Lissauer, 1987; Kokubo & Ida, 1995; Goldreich et al., 2004a). At low Σ/σ, the solid line overestimates the protoplanet mass by over an order of magnitude. This is a result of large $\langle N \rangle_{\rm eq}$, which allows the disk mass to be distributed into several smaller bodies instead of a single

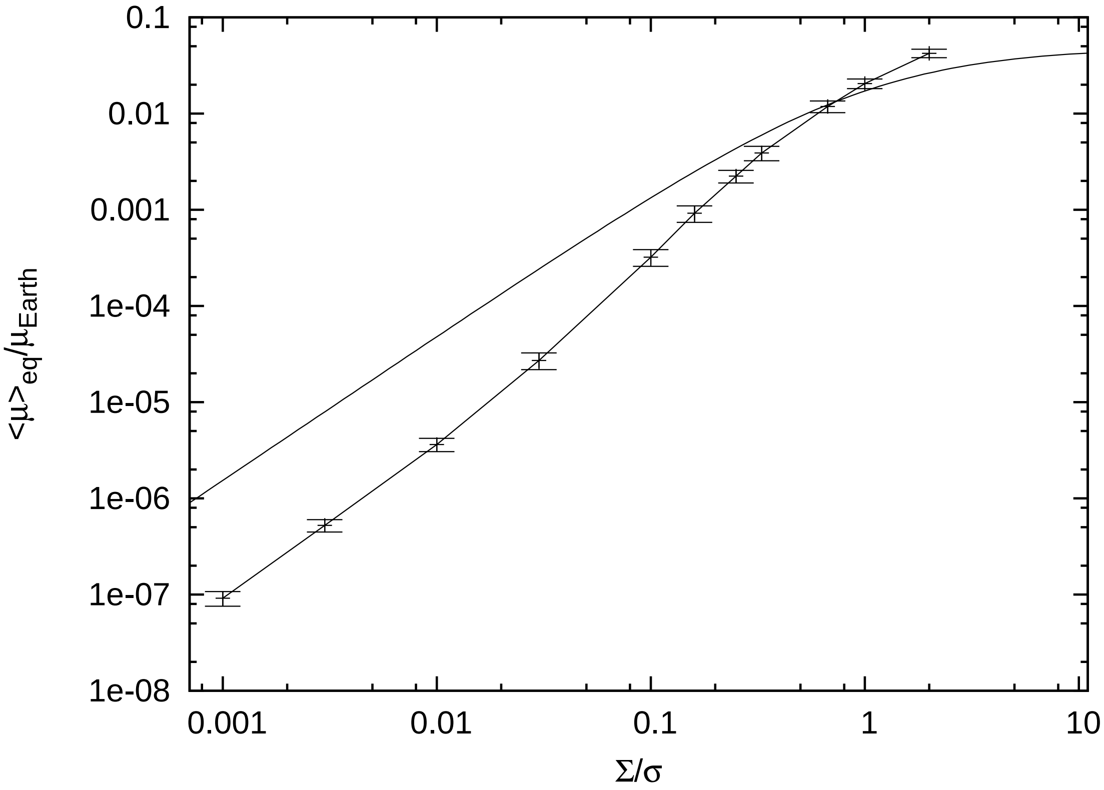

Figure 3.8 Average mass of a protoplanet in an equilibrium oligarchy as a function of the surface mass density ratio Σ/σ at $a = 1$ AU. The error bars are the standard deviation in average mass of the simulations for Σ/σ and $\langle N\rangle_i = \langle N\rangle_{\mathrm{eq}}$. The solid line plots the average protoplanet mass given by an $\langle N\rangle = 1$ and $\langle x_H\rangle = 5$ oligarchy commonly assumed in the literature, described by equation 3.9.

protoplanet in each oligarchic zone. For Σ/σ greater than about 0.5, the lines cross, and the simple picture is an underestimate of $\langle\mu\rangle_{\mathrm{eq}}$. Although $\langle N\rangle_{\mathrm{eq}}$ is close to 1 for these disks, $\langle x_H\rangle_{\mathrm{eq}}$ grows, increasing the relative amount of the total disk mass that has been accreted into each protoplanet.

We performed the same calculations for several sets of simulations with the annulus of protoplanets centered at 25 AU. The values of $\langle N\rangle_{\mathrm{eq}}$ that we find for these simulations are plotted in the dashed line in Figure 3.6. For $\Sigma/\sigma < 0.1$, the co-orbital groups tend to contain more oligarchs at 25 AU than at 1 AU, but the spacing between rows is still $\langle x_H\rangle_{\mathrm{eq}} \approx 5.5$. For larger Σ/σ, the distance of the protoplanets from the star matters less.

3.5 Isolation

Oligarchic growth ends when the protoplanets have accreted most of the mass in their feeding zones and the remaining planetesimals can no longer damp the eccentricities of the protoplanets. The eccentricities of the protoplanets then grow unchecked; this is known as the “isolation” phase. The mass of a protoplanet at this point is referred to as the "isolation mass," and can be found from equation 3.9:

$$\frac{M_{\rm iso}}{M_{\rm star}} = \frac{1}{3^{1/2}}\left[\left(\frac{\Sigma/\sigma}{\Sigma/\sigma+1}\right)\frac{M_{\rm disk}}{M_{\rm star}}\frac{\langle x_H\rangle}{\langle N\rangle}\right]^{3/2}. \tag{3.10}$$

The literature typically assumes that at isolation all of the mass is in protoplanets. This is equivalent to the limit of $\Sigma/\sigma \gg 1$.

The results of Section 3.4 show that oligarchy at a fixed semimajor axis is uniquely described by Σ/σ. For the terrestrial region then, $M_{\rm iso}$ is given by the parameters we calculate in Section 3.4, and is plotted as a function of Σ/σ in Figure 3.8.

The exact ratio of mass in protoplanets to that in planetesimals that allows the onset of this instability in the terrestrial region is not known; simulations suggest that in the outer solar system this fraction $\Sigma/\sigma \approx 10$ (Ford & Chiang, 2007). It is not straightforward to determine the value of Σ/σ for which isolation occurs. In many of our simulations, the eccentricities of the protoplanets rise above $e_{\rm H}$, yet an equilibrium is eventually reached. We postpone a detailed investigation of the dynamics of the isolation phase for a later work. For any value of Σ/σ at isolation however, the properties of the oligarchy at this stage can be read from Figures 3.6, 3.7, and 3.8.

The fate of the protoplanets after isolation depends on their distance from the star. In the outer parts of the solar system, the nascent ice giants are excited to high eccentricities and may be ejected from the system entirely (Goldreich et al., 2004a; Ford & Chiang, 2007; Levison & Morbidelli, 2007). Their lower rate of collisions also likely increases their equilibrium co-orbital number for a fixed Σ/σ relative to this work performed in the terrestrial region. In contrast to giant impacts, ejections do not change the mass of individual protoplanets, so they must reach their full planetary mass as oligarchs. For an $\langle N\rangle \neq 1$ at isolation, the mass of the disk needs to be augmented proportionally to $\langle N\rangle$ so that $\langle \mu\rangle_{eq}$ at isolation is equal to the mass of an ice giant.

The terrestrial planets tend to collide before they can be ejected, as the escape velocity from their surfaces is smaller than the velocity needed to unbind them from solar orbits (Chambers, 2001; Goldreich et al., 2004a; Kenyon & Bromley, 2006). This process conserves the total mass of protoplanets so $M_{\rm disk}$ is given by the minimum mass solar nebula. Accounting for $\langle N\rangle \neq 1$ in this case reduces the mass of each body at isolation proportionally to $\langle N\rangle^{3/2}$. This in turn increases the number of giant impacts necessary to assemble the terrestrial planets.

3.6 Conclusions and Discussion

We have analyzed the interactions of a disk of protoplanets experiencing dynamical friction. Conjunctions of a pair of protoplanets separated by more than 3 $R_{\rm H}$ increase the separation of that pair. The repulsions from internal protoplanets cancel those from external protoplanets at a specific equilibrium semimajor axis. Several bodies can inhabit this semimajor axis on horseshoe-like orbits. We have shown through numerical simulations that these co-orbital systems do form and survive. We expect the oligarchic phase of planet formation to proceed with a substantial population of co-orbital protoplanets. We present an empirical relation between the ratio of masses in protoplanets to planetesimals, Σ/σ, and the equilibrium average co-orbital number $\langle N \rangle$ and the equilibrium average spacing between co-orbital groups $\langle x_H \rangle$. To form the extra ice giants that populate the co-orbital groups in the outer solar system, the mass of the protoplanetary disk must be enhanced by $\langle N \rangle$ relative to the existing $N = 1$ picture. To form the terrestrial planets requires $\langle N \rangle^{3/2}$ more giant impacts. While we have not calculated the critical value of Σ/σ that initiates the isolation phase, we have completely determined the parameters of a shear-dominated oligarchy of protoplanets up to that point.

In Section 3.2, we have ignored the repulsive distant interactions between a protoplanet and the planetesimals that cause type I migration (Goldreich & Tremaine, 1980; Ward, 1986). The additional motion in semimajor axis is only a mild change to the dynamics. In a uniform disk of planetesimals, an oligarchic configuration of protoplanets migrates inward at an average rate specified by the typical mass of the protoplanets. Mass variation between the protoplanets of different co-orbital groups causes a differential migration relative to the migration of the entire configuration. However, the repulsion of the neighboring co-orbital groups counteracts the relative migration by displacing the equilibrium position between two groups by an amount $\sim (\sigma/\Sigma)(R_{\rm H}/a)R_{\rm H}$. Differential migration also acts on members of a single co-orbital group; however, its effects cannot accumulate due to the horseshoe-like co-orbital motion. The ratio of the timescale for migration across the co-orbital group to the interaction timescale sets a minimum safe distance from the equilibrium separation: $y_{\rm safe}/R_{\rm H} \sim \mu^{-1/6}(M_{\rm disk}/M_{\odot})^{1/2}$. For typical co-orbital group, where $y \sim R_{\rm H}$, the migration is never fast enough for a protoplanet to escape the group before the next encounter with a co-orbiting protoplanet brings it to the other side of the nominal equilibrium semimajor axis.

It is also possible that the disk of planetesimals is not uniform. The accretional growth of a protoplanet may lower the surface density of planetesimals at that semimajor axis such that the total mass is locally conserved. One might naively expect that the deficit of planetesimals exactly cancels the repulsion caused by the formed protoplanet. However, it can be seen from equation 3.5 that the rate of repulsion of a protoplanet from another protoplanet of comparable mass is twice that of the same mass in planetesimals. The net rates of repulsion of the protoplanets in this scenario are reduced by a factor of 2; the dynamics are otherwise unchanged.

One important question is that of the boundary conditions of a planet-forming disk. The initial conditions of the simulations we present only populate a small annulus around the central star. We artificially confine the bodies in this region to force the surface mass density to remain constant. The behavior of Σ over a larger region of the disk may not be similar to that of our annulus. The presence of gas giants or previously formed planets may prevent any wide-scale diffusion of protoplanets across the disk. On the other hand, the dynamics in a logarithmic interval of semimajor axis may not be affected by the populations internal and exterior to that region. The behavior of protoplanets in the oligarchic phase in a full size protoplanetary disk is an open question.

Earlier analytical work has examined the interactions between oligarchs that share a feeding zone (Goldreich et al., 2004b). These authors conclude that protoplanets in an oligarchic configuration are always reduced to an $\langle N \rangle = 1$ state. However, we have shown that for a shear-dominated disk, the collision rate between protoplanets is suppressed as the protoplanets are pushed toward almost the same semimajor axis. The growth rate of the protoplanets of each co-orbital group depends on the eccentricity of the planetesimals. For $e_p < \alpha^{1/2} e_{\rm H}$ the growth rate of a protoplanet scales as R^{-1}. This is called "orderly" growth since all of the protoplanets approach the same size. In the intermediate shear-dominated regime of $\alpha^{1/2} e_{\rm H} < e_p < e_{\rm H}$, the growth rate is independent of R. The protoplanets then retain the relative difference in their sizes as they grow. For shear-dominated disks, which are the focus of this chapter, the co-orbital groups are not disrupted by differential growth.

The spacing between co-orbital groups that we observe for most Σ/σ is smaller than the $10R_{\rm H}$ that is typically assumed (Kokubo & Ida, 1998, 2002; Thommes et al., 2003; Weidenschilling, 2005) based on the simulations by Kokubo & Ida (1998). Their simulations are in the dispersion-dominated eccentricity regime, where the maximum distance at which an oligarch can accrete a planetesimal is set by the epicyclic motion of the planetesimals, $\sim ea$. This motion sets the width of the feeding zones; the figures of Kokubo & Ida (1998) indicate that the typical eccentricity of the smaller bodies corresponds to a distance of $10R_{\rm H}$. Dispersion-dominated disks with different values for protoplanet sizes and planetesimal eccentricities should undergo oligarchy with a different spacing. In shear-dominated disks, we have shown that separations of about $5R_{\rm H}$ are set by the distant encounters with the smallest impact parameters.

The simulations of Kokubo & Ida (1998) do not contain any co-orbital groups of protoplanets; this is expected due to the small number of protoplanets that form in their annulus and the fact that their eccentricities are super-Hill. Thommes et al. (2003) examined a broad range of parameters of oligarchic growth, but the number of planetesimals are not enough to damp the protoplanet eccentricities sufficiently. However, upon inspection of their Figure 17 we find hints of the formation of co-orbital groups. Also, even though a range of separations is visible, many adjacent feeding zones are separated by only $5R_{\rm H}$, as we are find in our simulations.

Simulations by Ford & Chiang (2007) of the oligarchic phase and the following epoch of isolation included only five bodies that were spaced safely by $5R_{\rm H}$. We would not expect the formation of co-orbital oligarchs from an initial state of so few. Interestingly, Levison & Morbidelli (2007) used a population of "tracer particles" to calculate the effects of planetesimals on their protoplanets and find a strong tendency for these objects to cluster both in co-orbital resonances with the protoplanets and in narrow rings between the protoplanet orbits. This behavior can be understood in light of our Equation 3.2 with the dynamical friction of our simulations replaced by the collisional damping of the tracer particles.

Simulations of moderate numbers of protoplanets with eccentricity damping and forced semimajor axis migration were studied by Cresswell & Nelson (2006); indeed they observed many examples of the co-orbital systems we have described. We offer the following comparison between their simulations and this work. Their migration serves the same purpose as the growth we included in the simulations of Section 3.3, namely to decrease the separations between bodies until strong interactions rearrange the system with stable spacings. The co-orbital systems in their simulation likely form in the same way as we have described: a chance scattering to almost the same semimajor axis as another protoplanet. They attributed the tightening of their orbits to interactions with the gas disk that dissipates their eccentricity, however, this is unlikely. Although very close in semimajor axis, in inertial space the co-orbital protoplanets are separated by $\sim a$ for most of their relative orbit. Since the tightening of each horseshoe occurs over only a few relative orbits, it must be attributed to the encounters with the other protoplanets, which occur more often than the encounters between the co-orbital pairs.

Cresswell and Nelson also found that their co-orbital pairs settle all the way to their mutual L4 and L5 Lagrange points; the systems that we describe do not. In our simulations a single interaction between neighbors moves each protoplanet a distance on the order of the width of the largest possible tadpole orbit, $\Delta a/a \sim \mu^{1/2}$. The objects in the simulations by Cresswell and Nelson have much larger mass ratios with the central star and larger separations. In their case a single interaction is not strong enough to perturb the protoplanets away from the tadpole-like orbits around the Lagrange points. We have performed several test integrations with parameters similar to those run by Cresswell and Nelson and confirmed the formation of tadpole orbits. Finally, their simulations model the end of the planet formation and hint at the possibility of discovering extrasolar planets in co-orbital resonances. In a gas-depleted region, we do not expect the co-orbital systems that form during oligarchic growth to survive the chaos following isolation.

In the terrestrial region of the solar system, geological measurements inform our understanding of the oligarchic growth phase. Isotopic abundances of the Martian meteorites, in particular that of the hafnium (Hf) to tungsten (W) radioactive system, depend on the timescale for a planet to separate internally into a core and mantle. Based on these measurements, Halliday & Kleine (2006) calculated that Mars differentiated quickly compared to the timescale of the Hf-W decay, 9 Myr. The oligarchic picture of equation 3.9 with $\langle N \rangle = 1$ shows that at 1.5 AU with $\langle N \rangle = 1$, and $\Sigma \sim \sigma$, $\langle \mu \rangle \approx M_{\rm Mars}/M_{\odot}$; accordingly these authors inferred that Mars was fully assembled by the end of the oligarchic phase and did not participate in the giant impacts that assembled Earth and

Venus. A co-orbital oligarchy, however, lowers the mass of each protoplanet at isolation by a factor of $\langle N \rangle^{3/2}$. In this picture Mars formed through several giant impacts. This scenario is consistent with the isotopic data if Mars can experience several collisions in 10 Myr; the collisional timescales for $\langle N \rangle > 1$ systems merit further investigation.

The rate and direction of the rotation of Mars, however, provide further evidence of a history of giant impacts. Dones & Tremaine (1993) calculated the angular momentum provided by the collisionless accretion of planetesimals and showed that, for any planetesimal velocity dispersion, this process is insufficient to produce the observed spins. The moderate prograde rotation of Mars is thus inconsistent with pure accretionary growth. Schlichting & Sari (2007) showed that the collisions of planetesimals inside the Hill sphere as they accrete produce protoplanets that are maximally rotating, which is still inconsistent with the current rotation of Mars. Giant impacts later redistribute the spin-angular-momentum of the protoplanets but with a prograde bias; this then implies that Mars did participate in the giant impact phases of the terrestrial region. Again, further studies are necessary to characterize the timescale of the collisional period following the isolation phase in an $\langle N \rangle > 1$ scenario.

The compositions of the planets offer more clues to their formation. As protoplanets are built up from smaller objects in the protoplanetary disk, their composition approaches the average of the material from which they accrete. Numerical simulations by Chambers (2001) showed that the collisional assembly of protoplanets through an $\langle N \rangle = 1$ oligarchy mixes material from a wide range of semimajor axes. The composition of the planets then reflects some average of all available material. The three stable isotopes of oxygen are thought to be initially heterogeneous across the protoplanetary disk, and offer a measurable probe of compositional differences between solar system bodies. In the case of the Earth and Mars, a small but finite difference in the ratios of these isotopes is usually attributed to the statistical fluctuations of the mixing process (Franchi et al., 2001; Ozima et al., 2007). An $\langle N \rangle > 1$ oligarchy requires more collisions; the same isotopic variance between Earth and Mars may require a larger dispersion in the composition of the smallest protoplanetary materials. However, it is necessary to determine the extent of spatial mixing in the $\langle N \rangle > 1$ picture and to understand the changes in composition resulting from a single giant impact (Pahlevan & Stevenson, 2007) before we can estimate the primordial compositional variations allowed by this model.

We thank D. Stevenson for enlightening discussions. Insightful comments by our referee, E. Kokubo, motivated significant improvements to this work.

Chapter 4

Protoplanet Dynamics in a Shear-Dominated Disk

Terrestrial planets, ice giants, and the cores of the gas giants are thought to form by accretion of planetesimals into protoplanets. The protoplanets emerge from the swarm of planetesimals after an epoch of runaway accretion. The subsequent dynamics of the protoplanets set several important features of the final planetary configuration, such as the mass and number of planets or cores. It is difficult to constrain this evolution, however, without constraining the properties of the disk in which they are embedded.

One important yet uncertain parameter is the size of the planetesimals, the building blocks. The outer solar system and the later stages of formation in the inner solar system likely lack gas, allowing the formation of kilometer-size bodies through gravitational instabilities. Those bodies collide and grind each other down to even smaller sizes in a collisional cascade. The existence of bodies small enough to damp their own velocity dispersion is an inevitable conclusion from the existence of Uranus and Neptune (Goldreich et al., 2004b). Without such small bodies, the ability of a growing protoplanet to gravitationally focus the planetesimals becomes inefficient, and the growth timescale becomes too long, of order 10^{12} years in the outer solar system.

The unavoidable influence of the planetesimals make numerical studies of planet formation difficult to carry out accurately. Despite modern computational power, an integration of the equations of motion for each body in a protoplanet and planetesimal swarm is impossible. Even without allowing planetesimal fragmentation, the number of kilometer-size bodies needed to comprise a Neptune-size mass is humongous, of order 10^{12}. Kokubo & Ida (1996) performed numerically feasible but physically less appropriate N-body simulations of a protoplanetary disk in which the size of planetesimals is larger than the value required to form the ice giants of our solar system. Although interesting from a dynamical viewpoint, the results of such simulations can not be extrapolated to the scenario of smaller planetesimals since they lack collisional damping.

An alternative numerical approach to studying these systems is a coagulation code (Lee, 2000; Kenyon & Luu, 1998) in which the bodies are divided into size bins and the interaction of each pair of bins is calculated statistically. This approach fails once the number of bodies in any bin is not sufficiently large. Kenyon & Bromley (2006) have developed a hybrid code that treats planetesimals statistically while a small number of large bodies are integrated individually.

These results were previously published in Collins, B. F., & Sari, R. 2006, AJ, 132, 1316.

In this chapter, we examine the processes that shape the eccentricity distribution of the large bodies. We assume, simply, that the planetesimals constitute a cold disk due to sufficiently frequent collisions. As a first step, we include the dynamical friction that the planetesimals exert on the large bodies but ignore the much slower process of their accretion onto those bodies. The rates of cooling from dynamical friction and heating from mutual excitations are discussed in Section 4.1. We write a Boltzmann equation to show the change in the distribution function of eccentricities due to each process in Section 4.2, and discuss the solution to that equation. In Section 4.3 we present the results of complementary N-body simulations designed to measure the eccentricity distribution directly. A discussion of the results follows in Section 4.4.

4.1 Shear-Dominated Cooling and Heating Rates

The eccentricities of the protoplanets represent a kind of "thermal" energy in their orbits, relative to perfectly circular motion. The extra non-circular velocity itself varies in magnitude and direction over an orbital period; it is simpler to use the eccentricity, a constant of motion for the two-body problem. Specifically, we calculate the vector eccentricity,

$$\mathbf{e} = \frac{\mathbf{v}\times\mathbf{H}}{GM_p} - \hat{\mathbf{r}}. \tag{4.1}$$

This expression relates the eccentricity of the particle, $\mathbf{e}$, to the particle's position, $\mathbf{r}$, its velocity, $\mathbf{v}$, its orbital angular momentum vector, $\mathbf{H}$, and its mass, M_p. In general, a protoplanet can have an inclination relative to the disk plane, and the eccentricity vector can have three components. However, we show in Section 4.1.4 that the shear-dominated regime strongly inhibits the growth of inclinations. Two dimensions then suffice to describe the configuration space of $\mathbf{e}$.

We use the quantity of the Hill radius repeatedly in this work; for reference we define its value as

$$R_{\rm H} \;\equiv\; \left(\frac{M_p}{3M_\odot}\right)^{1/3} a \;=\; R/\alpha, \tag{4.2}$$

where M_p is the mass of a particle, a is its semimajor axis, R is its radius, ρ is its mean density, and

$$\alpha \;=\; \left(\frac{3M_\odot}{M_p}\right)^{1/3} \frac{R}{a} \;=\; \left(\frac{3\rho_\odot}{\rho}\right)^{1/3} \frac{R_\odot}{a}. \tag{4.3}$$

The Hill radius in turn specifies an eccentricity, the Hill eccentricity,

$$e_{\rm H} = R_{\rm H}/a. \tag{4.4}$$

We restrict this study to disks where the majority of the bodies have eccentricities lower than $e_{\rm H}$, known as the shear-dominated regime.

For most of this chapter, we employ the "two groups" approximation (Wetherill & Stewart, 1989; Goldreich et al., 2004b) and split the disk into two uniform populations. One group is the numerous smaller bodies, or "planetesimals." We denote their surface mass density as σ. The other group, the "protoplanets", consists of the bodies that dominate the excitations of the disk particles. Each protoplanet has a radius R, mass M, mean density ρ, and eccentricity e. We write the total surface mass density in protoplanets as Σ. We assume that $\sigma > \Sigma$, which keeps the protoplanets in the shear-dominate regime. It is likely that the violation of this assumption due to the growth of the protoplanets begins the final stages of planet formation (Goldreich et al., 2004a).

4.1.1 Eccentricity Excitation of Protoplanets

We analyze the interaction of two protoplanets from a frame rotating with a reference orbit at a semimajor axis a. The difference between the Keplerian angular velocity at each radius induces a shearing motion between particles on nearby circular orbits. For an orbit interior to a by a distance b,

$$\Omega_{\mathrm{rel}}(b) = \Omega(a+b) - \Omega(a) \approx \frac{3}{2}\Omega\frac{b}{a}, \tag{4.5}$$

in the limit of $b \ll a$. This angular frequency also specifies the rate of conjunctions for the two bodies with orbits separated by b.

The change in their eccentricity from each conjunction can be calculated analytically for two nearly circular orbits when $b \gg R_{\mathrm{H}}$:

$$e_k = A_k\, e_{\mathrm{H}} \left(\frac{b}{R_{\mathrm{H}}}\right)^{-2}, \tag{4.6}$$

$$A_k = \frac{16}{3}\left[K_0(\frac{2}{3}) + \frac{1}{2}K_1(\frac{2}{3})\right] \approx 6.7. \tag{4.7}$$

K_0 and K_1 are modified Bessel functions of the second kind (Goldreich & Tremaine, 1980; Petit & Henon, 1986; Duncan et al., 1989). We note that e_k refers to the perturbed body, while e_{H} and R_{H} refer to the Hill parameters of the perturbing one. The kick, viewed as a change in the eccentricity vector, is independent of the original eccentricity of the particle. Its orientation is perpendicular to the line connecting the two protoplanets and the sun at conjunction; we therefore assume it is random.

The eccentricity kick given by one protoplanet is strongest for the particles that approach with an impact parameter on the order of the Hill radius. Interactions from a greater distance, however, occur more often. In a shear-dominated disk, eccentricities are small, $e \ll e_{\mathrm{H}}$; to change that eccentricity significantly only requires small perturbations. These frequent but weaker perturbations dictate the overall velocity evolution of the protoplanets (Goldreich et al., 2004b; Rafikov, 2004).

Specifically, the average differential rate that one protoplanet receives eccentricity kicks of strength e from other protoplanets is given by

$$d\mathcal{R}_{\rm ex}(e) = 2\ n_{\rm big}\ \frac{3}{2}\Omega b(e)\ \frac{db}{de}\ de, \tag{4.8}$$

where $n_{\rm big}$ is the number surface density of protoplanets and $\frac{3}{2}\Omega b(e)$ is the velocity of encounters at those separations (given by eq. 4.5). The factor of two accounts for the combination of interior and exterior encounters. The excitation rate of a protoplanet with eccentricity e is then the rate of kicks comparable in magnitude to its current eccentricity:

$$\left.\frac{1}{e}\frac{de}{dt}\right|_{\rm ex} \sim e\left|\frac{d\mathcal{R}_{\rm ex}(e)}{de}\right| \sim \frac{\Sigma\Omega}{\rho R}\frac{1}{\alpha^2}\frac{e_{\rm H}}{e}. \tag{4.9}$$

The inverse of this rate can be interpreted as the timescale for a protoplanet's eccentricity to change by an amount e.

4.1.2 Dynamical Friction

As each protoplanet moves through the disk, it scatters and excites the eccentricities of the planetesimals that surround it. Cold planetesimals that approach a protoplanet with impact parameters of about a Hill sphere leave with $\sim m\ e_{\rm H}$ of additional momentum. This can either add to or subtract from the eccentricity of the protoplanet depending on the relative orientation between the pre-encounter eccentricities of the protoplanet and planetesimal. We write the net effect (Goldreich et al., 2004b)

$$M\frac{de}{dt} \sim -n_s R_{\rm H} e_{\rm H} m(e_{\rm H}+e) + n_s R_{\rm H} e_{\rm H} m(e_{\rm H}-e), \tag{4.10}$$

for a number surface density of planetesimals n_s. This formula yields the damping rate, or the inverse damping time,

$$\tau_d^{-1} \equiv \left.\frac{1}{e}\frac{de}{dt}\right|_{\rm d.f.} = C_d\frac{\sigma\Omega}{\rho R}\frac{1}{\alpha^2}. \tag{4.11}$$

Calculating the coefficient C_d requires a more precise analysis of planetesimal scattering. We adopt the value $C_d \approx 10$ found by Ohtsuki et al. (2002), who measure the coefficient numerically.

4.1.3 Planetesimal Interactions

The distribution of planetesimal eccentricities does not affect our results, as neither the excitation nor the damping rates depend on their eccentricity as long as the planetesimals remain in a shear-dominated state. In this work, we focus on a range of parameters such that collisional cooling keeps the eccentricities of planetesimals below $e_{\rm H}$ and enforces the condition of shear domination.

4.1.4 Inclinations

An orbit with a small inclination angle i carries its particle out of the disk plane on vertical excursions of size $\sim ia$. An interaction that excites that particle's eccentricity also affects its inclination, but with a magnitude inhibited by the geometry of the distant encounter:

$$\frac{i_k}{e_k} \sim \frac{a\ i}{b} \ \Rightarrow\ \frac{i_k}{i} \sim \left(\frac{e}{e_{\rm H}}\right)^{3/2} \frac{e_k}{e}, \tag{4.12}$$

where b is the impact parameter of the perturber and i_k is the resulting change in inclination from an encounter. In contrast, planetesimals just entering the Hill sphere of a protoplanet damp the protoplanet's non-circular velocity in all dimensions; no equivalent geometric factor inhibits the damping of inclinations. With the growth of inclinations suppressed, shear-dominated protoplanet disks are effectively two-dimensional (Wetherill & Stewart, 1993; Goldreich et al., 2004b; Rafikov, 2003).

4.1.5 The Eccentricity Distribution — a Qualitative Discussion

The dynamical friction rate sets a characteristic time over which the eccentricities of all of the bodies are changed significantly. In this sense, the eccentricity distribution of the protoplanetary swarm is reset every τ_d. The excitation rate, however, varies with e. Equating the excitation rate, Equation 4.9, and the damping rate, Equation 4.11, yields an important reference value, $e_{\rm eq}$:

$$e_{\rm eq} \sim \frac{\Sigma}{\sigma} e_{\rm H}. \tag{4.13}$$

Statistically, each protoplanet receives one kick of this magnitude every damping timescale. We note that our restriction to disks where $\sigma > \Sigma$ enforces the condition that $e_{\rm eq} < e_{\rm H}$, or that the planetesimal damping effectively balances the protoplanet stirring.

We deduce the distribution of eccentricities on each side of $e_{\rm eq}$ by examining the dependence of the kicking rate on eccentricity. Excitation to $e \gg e_{\rm eq}$ requires a kick $e_k \gg e_{\rm eq}$. Such strong kicks occur less often in one damping timescale than kicks of strength $e_{\rm eq}$ by a factor of $e_{\rm eq}/e_k$. With fewer kicks to populate the high eccentricity distribution, the number of bodies with such eccentricities echoes the rate of kicks and falls off with eccentricity as e^{-1}(Goldreich et al., 2004b).

Kicks of order $e \ll e_{\rm eq}$ occur frequently in each damping timescale, thereby overwhelming the effects of dynamical friction on the lowest eccentricity bodies. A dynamic equilibrium dominated by only the stirring mechanism implies that kicks to and from every eccentricity vector occur at the same rate. For this to be true the distribution must be constant over the configuration space. The number of bodies with an eccentricity of order $e \ll e_{\rm eq}$ then scales as the area of configuration space available, $\sim e^2$.

4.2 A Boltzmann Equation

In the following section we develop a differential equation to describe analytically the distribution function of protoplanet eccentricities. We construct this equation in the spirit of the Boltzmann equation, examining the change in the number of bodies with a particular eccentricity due to the effects of dynamical friction and viscous stirring.

The space of possible eccentricities is inherently two-dimensional (eq. 4.1), since inclinations can be neglected (Section 4.1.4). Additionally, the interaction rates depend only on the magnitude of the protoplanet eccentricity, forcing the distribution function to share this dependence: $f(\mathbf{e}) = f(e)$. The two dimensional $f(e)$ is related to the number of bodies with velocity on the order of e by its integral, roughly $e^2 f(e)$.

Dynamical friction lowers the eccentricities of all bodies proportionally to their eccentricity. Equivalently, the number of bodies with a certain e changes as the protoplanets with that value are damped to lower eccentricities and replaced by bodies from a higher eccentricity. We write this as:

$$\left.\frac{\partial f(e)}{\partial t}\right|_{\rm d.f.} = -\,{\rm div}\left(f(e)\frac{\partial \mathbf{e}}{\partial t}\right) = \frac{\partial f(e)}{\partial e}\frac{e}{\tau_d} + \frac{2f(e)}{\tau_d}, \tag{4.14}$$

where we have used $\partial \mathbf{e}/\partial t = -\mathbf{e}/\tau_d$ for the effects of dynamical friction.

At a given $\mathbf{e}$, particles are kicked to a new eccentricity $\mathbf{e}_n$ at an average rate that depends on the magnitude of the kick, $|\mathbf{e}_n - \mathbf{e}|$. Also, particles with an initial eccentricity $\mathbf{e}_n$ are kicked to $\mathbf{e}$ at the same rate. The total flux of particles to and from a given eccentricity is:

$$\left.\frac{\partial f(e)}{\partial t}\right|_{\rm kicks} = \int\!\!\int p(|\mathbf{e}_n - \mathbf{e}|)[f(e_n) - f(e)]\; d^2\mathbf{e}_n, \tag{4.15}$$

where $p(e)$ describes the rate at which bodies experience changes in their eccentricities by an amount e. This is the two-dimensional analog of the excitation rate Equation 4.9:

$$p(e) = \frac{1}{2\pi\; e}\left|\frac{\partial \mathcal{R}_{\rm ex}}{\partial e}\right| = A_k\;\frac{9}{16\pi^2}\frac{\Sigma\Omega}{\rho R}\frac{1}{\alpha^2}\;e_{\rm H}\;\frac{1}{e^3}. \tag{4.16}$$

The sum of the dynamical friction terms and the kicking integral describes the dynamics of shear-dominated protoplanets interacting with each other in a smooth disk of planetesimals. The combined influence of these two processes can bring the protoplanets into an equilibrium state, where the number of particles with eccentricity $\mathbf{e}$ remains constant in time:

$$0 = \frac{\partial f(e)}{\partial e}\frac{e}{\tau_d} + \frac{2f(e)}{\tau_d} + \int\int p(|\mathbf{e}_n - \mathbf{e}|)\,[f(e_n) - f(e)]\,d^2\mathbf{e}_n. \tag{4.17}$$

4.2.1 The Solution

We show in Appendix A that

$$\begin{aligned} f(e) &= \frac{1}{2\pi e_*^2}\left[1 + \left(\frac{e}{e_*}\right)^2\right]^{-3/2}, \\ e_* &= \frac{9A_k}{8\pi C_d} e_{\rm eq} \approx 0.24\frac{\Sigma}{\sigma}e_{\rm H} \end{aligned} \tag{4.18}$$

satisfies the equilibrium equation, Equation 4.17 for all e. This function is the equilibrium eccentricity distribution of shear-dominated protoplanets.

The solid line in Figure 4.1 shows a distribution function for $\Sigma \approx 0.002$ g cm^{-2} and $\sigma = 0.1$ g cm^{-2}. Although the function formally extends above $e_{\rm H}$, we stress that it is only accurate for eccentricities $e \ll e_{\rm H}$. Both the dynamical friction and the excitation rates (eqs. 4.14 & 4.16) are not valid for $e \gtrsim e_{\rm H}$.

Several moments of the distribution can be calculated in terms of the only free parameters:

$$\frac{e_{\rm median}}{e_{\rm H}} = 0.41\frac{\Sigma}{\sigma}, \quad \frac{\langle e\rangle}{e_{\rm H}} = 0.24\frac{\Sigma}{\sigma}\log(3\frac{\sigma}{\Sigma}), \quad \frac{\langle 1/e\rangle^{-1}}{e_{\rm H}} = 0.24\frac{\Sigma}{\sigma}. \tag{4.19}$$

According to Equation 4.18, $\langle e\rangle$ is infinite. However, the largest single kick in eccentricity from an almost circular protoplanet encounter is of order $e_{\rm H}$. Truncating the integral at $e_{\rm H}$ produces the logarithmic term in the expression above. Moments higher than the mean also diverge; realistically, they are dominated by the bodies with the highest eccentricities, of order $e_{\rm H}$.

It is easy to see that this solution, in the high- and low-eccentricity limits, produces the same power-laws discussed in Section 4.1.5. In fact, it can be shown directly from Equation 4.17 that any solution to this differential equation reduces to those limiting power-laws.

4.3 Numerical Simulations

Here we describe a direct measurement of the eccentricity distribution from gravitational N-body simulations that include an additional force to represent dynamical friction.

The N-body part of our simulation uses Gauss's equations to evolve a set of orbital constants chosen to vary slowly under small perturbations. A modified version of Kepler's equation produces the orbital phase for each body at each time step. The IDA solver from the SUNDIALS software package (Hindmarsh et al., 2005) integrates the dynamical equations. During close encounters of two protoplanets, we integrate their motion relative to the center of mass of the pair.

We represent the planetesimal population in these simulations with an extra force term that damps the non-circular velocities of the protoplanets at the rate $\mathcal{R}_d(e)$, given by Equation 4.11. An ad-hoc transition between the damping rate for $e < e_{\mathrm{H}}$ and the appropriate rate for $e > e_{\mathrm{H}}$ prevents unphysical enhancements of the damping force during close encounters. The growth of protoplanets in mass due to planetesimal accretion is not included; the accretion rate is always lower than the dynamical friction rate and will not affect the eccentricity evolution (Goldreich et al., 2004b).

Each simulation begins with the protoplanets on circular orbits with random phases and random semimajor axes, within a chosen annulus. The average spacing between bodies, $M/(\Sigma 2\pi a)$, is several Hill radii. The protoplanets interact for several damping timescales τ_d before the distribution reaches equilibrium.

We record the eccentricity of the protoplanets every $\Delta t \approx 0.1\tau_d$ starting at about 100 τ_d. The bodies in the inner and outer edges of the disk are not measured, to avoid artificial boundary effects that inhibit excitations. We bin all of the measured eccentricities logarithmically; a well populated histogram is produced with several hundred orbits of measurement. Errors are assigned to each bin according to a Poisson distribution with the sample size defined as the product of the number of bodies measured and the sampling time in units of the damping timescale τ_d. Since each protoplanet suffers a significant change in eccentricity every τ_d, one measurement of the eccentricity distribution is independent from a previous measurement if they are separated in time by τ_d. We sample faster than τ_d to increase the resolution of the histogram slightly.

The statistical error bars do not take into account the inhomogeneity of the protoplanet disk on small length scales. Given a surface density, the mass of a single protoplanet sets a typical radial separation between bodies. This length scale corresponds to an eccentricity scale through Equation 4.6 (in the simulations presented here, this value is slightly below e_{H}). As the disk evolves, the viscous stirring causes migrations in the semimajor axes of the particles that smooth the average radial distribution. If measured only over intervals shorter than the migration timescale, the eccentricity distribution may vary for eccentricities above the eccentricity set by the typical separation. Fluctuations from this effect are visible in Figures 4.1 and 4.2.

Several simulations of disks with different protoplanet mass distributions are presented below.

4.3.1 Equal Mass Protoplanets

Figure 4.1 shows the eccentricity distribution measured from a simulated disk of 120 equal mass protoplanets ($M = 2.5 \times 10^{-9} M_{\odot}$) with surface densities $\Sigma \approx 0.002$ g cm^{-2} and $\sigma = 0.1$ g cm^{-2}. A single population of protoplanets best reflects the “two groups” approximation we use to derive

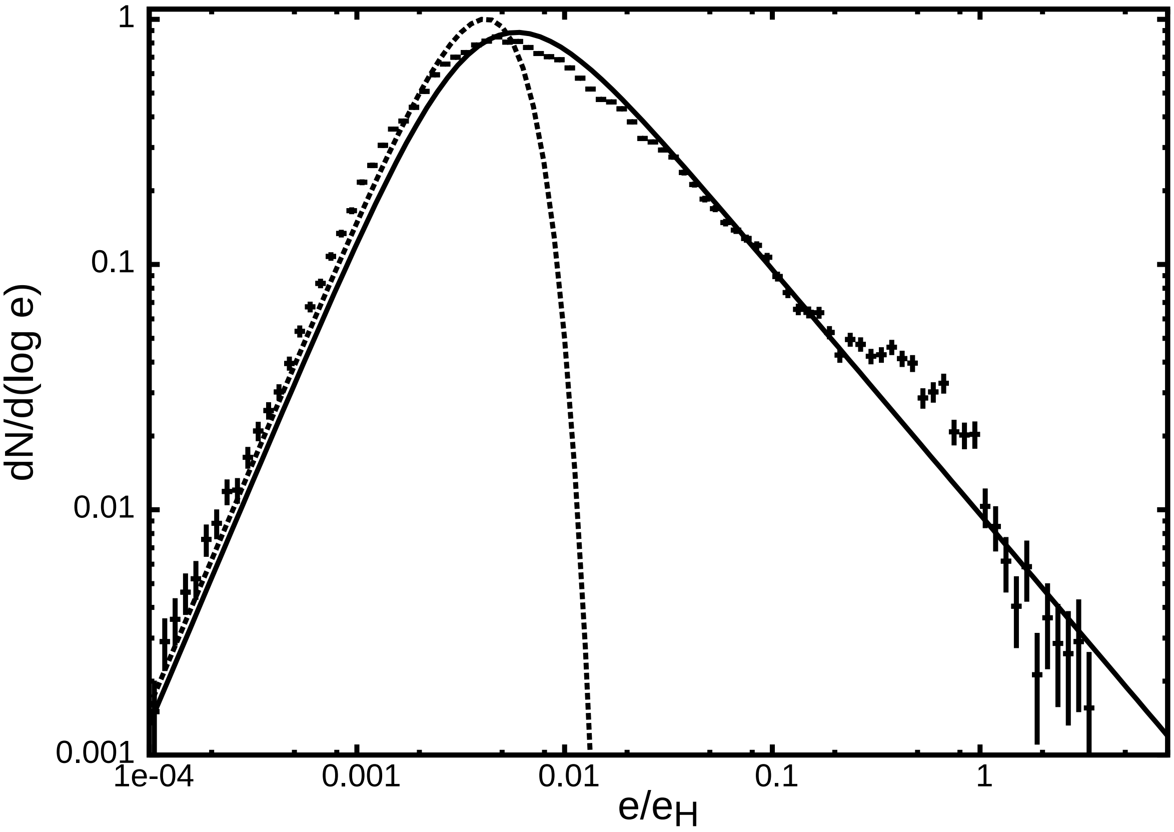

Figure 4.1 Plot of Equation 4.18 superposed with the results of a numerical simulation. The simulated disk contains 120 bodies of mass $M = 5 \times 10^{24}$g, or $\Sigma \approx 0.002$ g cm^{-2}. A planetesimal surface density of $\sigma = 0.1$ g cm^{-2} is included. We assume each bin obeys Poisson statistics and assign errors based on a population size of $N_b N_{\tau_d}$, where N_b is the number of bodies in the simulation, and N_{τ_d} is the total measurement time in units of damping timescales. The solid line shows the distribution as given by Equation 4.18, using the same values of Σ and σ. A Rayleigh distribution with a similar peak eccentricity is plotted with the dashed line.

Equations 4.9 and 4.11. The analytic solution, Equation 4.18, for the same parameters in the simulation is superposed on Figure 4.1. While the overall match is not perfect, the shape of each curve is strikingly similar. The two curves match extremely well if one is shifted by around 15 percent in the e direction. This difference is attributable to the difficulty of assigning a correct value of Σ to the simulation given a finite number of protoplanets.

We note that there are no free parameters in this comparison. The numerical distribution is a direct counting of the number of bodies within each eccentricity bin, while a choice of Σ, σ, and M completely specifies the analytical curve.

4.3.2 Mass Distributions

Naturally occurring protoplanet populations exhibit non-trivial distributions in mass. Before describing such a disk in the framework we have developed, we clarify several points.

Protoplanets with different masses, or equivalently, different radii, experience different viscous stirring rates. We decompose the total surface density in protoplanets, Σ, into a differential quantity, $d\Sigma/dR$, and write the excitation rate of a body with radius R as

$$\mathcal{R}_x(e,R) \sim \int \frac{d\Sigma}{dR'}\frac{\Omega}{\rho R'}\frac{1}{\alpha^2}\frac{e_{\rm H}(R')}{e}\, dR'. \tag{4.20}$$

The identity $e_{\rm H}(R') = (R'/R)e_H(R)$ when substituted into Equation 4.20 yields

$$\mathcal{R}_x(e,R) \sim \frac{\Omega}{\rho R}\frac{1}{\alpha^2}\frac{e_{\rm H}(R)}{e}\int \frac{d\Sigma}{dR'}\, dR'. \tag{4.21}$$

In words, the excitation rate of one body only depends on the total surface density of all other bodies, regardless of the specific mass distribution. This differs from the assertion by Goldreich et al. (2004b) that only the most massive bodies contribute to the viscous stirring rate. Equation 4.21 seems to indicate that there should be no distinction between big bodies and small bodies since every body contributes to the viscous stirring. A closer investigation uncovers the mass range of bodies that provide significant stirring.

Eccentricity kicks of strength e_k can occur at any combination of M and b that satisfies the inverse square law of gravitation: $e_k \sim M(R')b(R')^{-2}$. However, the smallest impact parameter that contributes to a body's excitation is about $R_{\rm H}$. A minimum $b(R') \sim R_{\rm H}$ sets a minimum mass for bodies to kick a body with mass M by an amount e_k:

$$M_{\rm min}(e_k,R) \sim \frac{e_k}{e_{\rm H}}M \tag{4.22}$$

Likewise, a body can only be as far away as its radial position in the disk, a. This sets a maximum mass,

$$M_{\rm max}(e_k,R) \sim \left(\frac{e_k}{e_{\rm H}}M\right)\frac{a^2}{R_{\rm H}^2}. \tag{4.23}$$

For a choice of the most relevant kick strength, e_k, these limits define the sizes of bodies that participate in the excitation of a body with size R.

As a numerical confirmation of these results, we simulate a disk of planetesimals with a surface mass density $\sigma = 0.2$ g cm^{-2} and 120 protoplanets. In this case, we divide the protoplanets into two groups of different mass: sixty of mass $m_1 = 2 \times 10^{24}$ g, and sixty of mass $m_2 = 3.8 \times 10^{25}$ g. These masses are within the limits set by Equations 4.22 & 4.23. We plot the absolute eccentricity distribution of each mass group binned separately in Figure 4.2. Additionally, we plot the analytic distributions given by the σ, as specified above, and Σ, the sum of the surface densities of both groups.

It is clear that each group of protoplanets with the same mass matches the analytic distribution

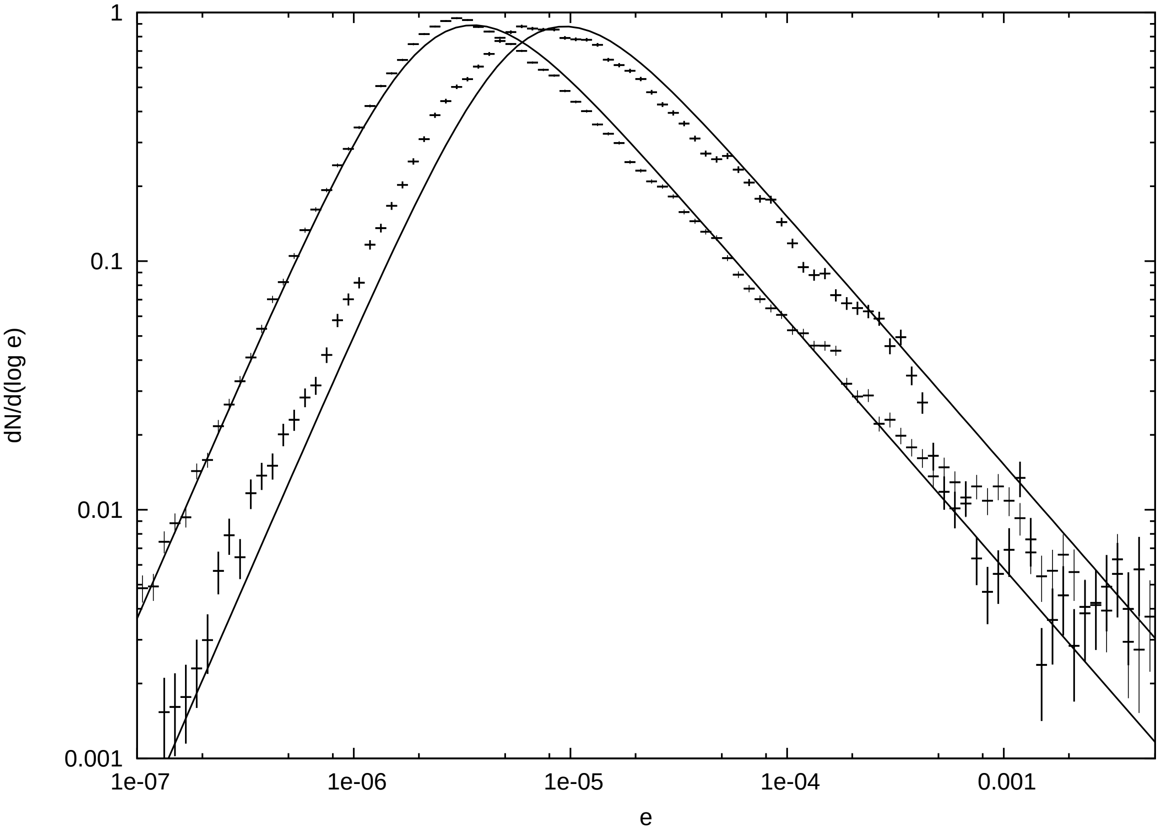

Figure 4.2 Comparison of the results of a numerical simulation of protoplanets in a perfectly bimodal mass distribution ($m_1 = 2 \times 10^{24}$ g, $m_2 = 3.8 \times 10^{25}$ g). We simulate sixty bodies of each mass, for a total surface density in protoplanets of $\Sigma \approx 0.003$ g cm^{-2} and a planetesimal surface density of $\sigma = 0.2$ g cm^{-2}. The eccentricities of each mass group are binned separately; each distribution is a good match to Equation 4.18 when scaled to the appropriate Hill eccentricity. The distribution for bodies of mass m_1 therefore peaks on the left, and the distribution for the higher mass bodies peaks on the right. The error bars are assigned following the same algorithm as Figure 4.1.

well. The offset between the peak of each group is due to the dependence of the distribution on the Hill eccentricity of each body. In general, the distribution for a swarm of protoplanets with a mass distribution is merely the sum of individual distributions for protoplanets of each mass.

4.4 Conclusions

We presented an analytic model for the distribution function of the eccentricities of a protoplanet population embedded in a shear-dominated planetesimal disk. The eccentricity distribution measured with numerical simulations matches the analytic result very well.

Since we have manually inserted the dynamical friction rate that we expect into the numerical simulations, this work does not test our prescription of dynamical friction. However, the numerical and analytic representations of viscous stirring are completely independent. Equation 4.17 uses a viscous stirring rate that includes only distant encounters. In our numerical simulations, Newton's laws dictate the protoplanet interactions directly without any simplifying assumptions. The consistency of the two calculations proves that in a two-dimensional shear-dominated disk, interactions between non-crossing orbits are entirely responsible for setting the eccentricities of the protoplanets.

Several features of the distribution highlight interesting properties of the dynamics. We reason in Section 4.1.5 that most protoplanets have eccentricities $\sim (\Sigma/\sigma)e_{\mathrm{H}}$, the value of e where the excitation and damping timescales are equal. The distribution function shows this to be true: the median and mean (up to a logarithmic factor) of any distribution are on the order of this equilibrium eccentricity. Higher moments of the distribution are dominated by the highest eccentricity bodies. This differences signal that different statistics of the distribution can reflect different subsets of the overall population. For example, the average "thermal" energy of the protoplanets is represented by their root-mean-squared eccentricity, $\langle e^2 \rangle$. The fractionally fewer bodies with eccentricities close to e_{H} dominate $\langle e^2 \rangle$ and thus, contain most of the energy.

The shape of the distribution also merits discussion. N-body integrations of a group of single mass bodies show that their eccentricities follow a Rayleigh distribution (Ida & Makino, 1992). For reference, we plot a Rayleigh distribution in Figure 4.1. It is entirely inconsistent with our calculations. This is not surprising. In addition to simulating bodies in the regime of eccentricities that are large compared to the Hill eccentricity, Ida & Makino (1992) do not include any effects that can balance the mutual excitations of their particles. The dynamical friction in our simulations balances the viscous stirring and establishes the equilibrium distribution we derive.

Since the accretion timescale is much longer than the dynamical timescale, the balance between eccentricity excitation and damping is maintained as Σ grows relative to σ. The peak of the distribution, set by Σ/σ, mirrors this growth and moves closer to e_{H}; the shape remains the same. Our assumptions fail, however, when $\Sigma \sim \sigma$. At this epoch, the typical velocities are close to e_{H} and the disk is no longer shear-dominated. Additionally, the damping rate can no longer balance the viscous stirring rate, and the eccentricities of the protoplanets will grow. The chaotic evolution that follows likely sets the final spacing and number of the resulting solar system (Goldreich et al., 2004a).

It is possible to extend this result to other scenarios. One situation with the same dynamics is planetesimals in the outer solar system in the presence of a gaseous disk. When the mean free path of the gas is long compared to the radius of a planetesimal, the damping timescale for the eccentricity of the planetesimals is constant. Assuming again that the disk is shear-dominated with respect to a population of larger protoplanets, those protoplanets excite the planetesimals through the same non-orbit crossing interactions discussed in Section 4.1.1. With a known distribution function, the average rate of catastrophic collisions can be calculated even when a typical body does not have enough energy for significant fragmentation. A collisional cascade to smaller planetesimals is crucial for the rapid growth of the protoplanetary cores necessary to form Uranus and Neptune (Goldreich et al., 2004b; Rafikov, 2004).

We thank Scott Kenyon and the anonymous referee for their useful comments.

4.5 Appendix: The Analytic Distribution Function

Here we outline the evaluation of the equilibrium equation, Equation 4.17, using the distribution function, Equation 4.18. To simplify the notation, we rescale all eccentricities by e_* and algebraically manipulate the coefficients of each term in Equation 4.17. We are left with the equivalent burden of proving that

$$g(e) = (1+e^2)^{-3/2} \tag{4.24}$$

satisfies

$$2\pi \frac{\partial g(e)}{\partial e} e + 4\pi g(e) = \int\int \frac{g(e) - g(e_n)}{|\mathbf{e}_n - \mathbf{e}|^3}\; d^2\mathbf{e_n}. \tag{4.25}$$

The left-hand side is easy to compute:

$$\text{L.H.S.} = \frac{4\pi}{(1+e^2)^{3/2}} - \frac{6\pi e^2}{(1+e^2)^{5/2}}. \tag{4.26}$$

To integrate the right-hand side, we translate the origin of the integration variables by $\mathbf{e}$ and rotate them to align $\mathbf{e}$ with one of the coordinate axes. In those coordinates:

$$I = \int_{-\infty}^{\infty}\int_{-\infty}^{\infty} \frac{1}{(k^2+h^2)^{3/2}} \left[\frac{1}{(1+e^2)^{3/2}} - \frac{1}{(1+k^2+(h+e)^2)^{3/2}}\right] dk\; dh, \tag{4.27}$$

with $\mathbf{e}_n = \{k, h\}$.

After the integration over k, we rewrite the integral in terms of a new variable $h' \equiv (1+e^2)/(eh)$,

$$I = \int_{-\infty}^{\infty} \left(\frac{2e}{(1+e^2)^{5/2}} + \frac{8}{(1+e^2)^2} \frac{\partial^2 E(e^2 z/(1+e^2))}{\partial z^2} |h'| h'^2 \right) dh', \tag{4.28}$$

where, $z = -2h' - h'^2$, and $E(e^2 z/(1+e^2))$ is the complete elliptic integral of the second kind.

We change the integration variable to z, taking care to evaluate the integrand with the appropriate branch of the double-valued relation $h'(z)$. The integral evaluates to

$$I = \frac{4\pi}{(1+e^2)^3} + \frac{8}{(1+e^2)^2} \int_0^1 \left[\frac{4-3z}{\sqrt{1-z}}\right] \frac{\partial^2 E(e^2 z/(1+e^2))}{\partial z^2} dz. \tag{4.29}$$

With the second derivative of the elliptic function expressed as a power series, each term can be integrated over z. The remaining power series in $e^2/(1+e^2)$ equals

$$
\begin{aligned}
I = {} & \frac{4\pi}{(1+e^2)^3} \\
& - \frac{3\pi e^4}{(1+e^2)^4}\left[{}_2F_1\left(\frac{5}{2}, 1; 3; \frac{e^2}{(1+e^2)}\right) - \frac{1}{2}\ {}_2F_1\left(\frac{3}{2}, 2; 3; \frac{e^2}{(1+e^2)}\right)\right].
\end{aligned} \tag{4.30}
$$

After additional algebraic manipulation, this result equals the left-hand side of the original equation (eq. 4.26).

Chapter 5

Self-Similarity of Shear-Dominated Viscous Stirring

Modern computational power allows the simultaneous integration of the orbits of increasingly numerous particles. Much of the planet formation process, however, involves particle numbers that exceed the limits of computational efficiency. This limitation is often circumvented with a statistical approach. By monitoring the gravitational interactions of the particles in a time-averaged sense, various properties of the particle population can be calculated without a full N-body simulation.

Collins & Sari (2006), presented in this thesis as Chapter 4, motivate a Boltzmann equation to describe the evolution of the eccentricity distribution of an ensemble of particles in which the relative motion between any two interacting particles is dominated by the shearing motion of close circular orbits. Such a regime of orbital eccentricities is called shear-dominated. The solution of their equation provides a simple analytic expression for the equilibrium eccentricity distribution that results when dynamical friction can balance the mutual interactions of the particles; the analytic expression matches results from numerical simulations remarkably well.

In this chapter we derive analytically the non-equilibrium distribution function of interacting shear-dominated particles in the absence of dynamical friction. Section 5.1 reviews the construction of the Boltzmann equation. In Section 5.2, we show that the distribution function behaves self-similarly, and the shape of the non-equilibrium distribution function is identical to the equilibrium distribution of Chapter 4. Section 5.3 generalizes our Boltzmann equation and its solution to include time-dependent rates of excitation and eccentricity-damping interactions. Section 5.4 corroborates our analytical results with numerical simulations. Conclusions follow in Section 5.5.

5.1 The Time-Dependent Boltzmann Equation

We consider a disk of particles on initially circular orbits around a massive central body. We write their surface mass density Σ and the mass of a single body m. The number density, Σ/m is sufficiently low that three-body encounters are very rare, therefore the orbital evolution of each body is well described as a sequence of pair-wise encounters.

The change in eccentricity due to one such encounter can be calculated analytically. For completeness, we summarize the derivation presented in Chapter 4. Let one particle, with a semimajor axis a, encounter another with semimajor axis $a + b$. In the limit of $b \ll a$, the relative orbital

---

These results were previously published in Collins, B. F., Schlichting, H. E., & Sari, R. 2007, AJ, 133, 2389.

frequency between the pair is $\Omega_r = (3/2)\Omega b/a$, where Ω is the Keplerian orbital frequency for a semimajor axis a. If in addition $b \gg R_{\rm H} = (m/(3M_\odot))^{1/3}a$, the change in eccentricity from one encounter is $e_k = (A_k/3)(m/M_\odot)(b/a)^{-2}$, where $A_k \approx 6.67$ collects the order-unity coefficients (Goldreich & Tremaine, 1978; Petit & Henon, 1986).

The eccentricity is not the only Keplerian element that characterizes the non-circular motion of a particle; the longitude of periapse specifies the relative orientation of a particle's epicycle. The particles may also follow orbits that do not lie in the disk. However, shear-dominated viscous stirring excites inclinations at a rate that is always slower than the excitation of eccentricities (Wetherill & Stewart, 1993; Goldreich et al., 2004b; Rafikov, 2003). The perpendicular velocities are, in this case, always negligible compared to the epicyclic motion in the disk plane.

The magnitude of an orbit's eccentricity and the longitude of periapse together specify a two-dimensional parameter space. We describe the two-dimensional variable with a vector, $\mathbf{e} = \{e\cos\omega, e\sin\omega\}$. The distribution function is a function of this vector and time, $f(\mathbf{e}, t)$. That the changes in $\mathbf{e}$ due to encounters do not depend on the longitude of periapse already shows that the distribution function must be axisymmetric, or $f(\mathbf{e}, t) = f(e, t)$. Then the number of bodies per unit logarithmic interval around e is given by $2\pi e^2 f(e, t)$.

We characterize the eccentricity growth with a differential rate, $p(\mathbf{e}_k)d^2\mathbf{e}_k$, that the eccentricity vector of a particle will be changed by an amount $\mathbf{e}_k$. Since the change in eccentricity experienced by a pair of bodies, when treated as a vector quantity, is independent of the initial eccentricity vector of each body, this function is also axisymmetric and only depends on the magnitude of the change of eccentricity, e_k.

The excitation rate depends on the surface mass density of particles in the disk, Σ, the mass of a single body, m, the mass of the central star, $M_\odot$, the cross section at which a particle experiences encounters of a strength e_k, and the relative speed of those encounters. The impact parameter at which a particle receives an eccentricity e_k scales as $b \propto e_k^{-1/2}$. If the eccentricities are small, the speed at which one particle encounters the others is set only by the shearing of their two orbits, which is proportional to b. Then, as shown in Chapter 4,

$$2\pi p(e_k)e_k de_k = 3\frac{\Sigma}{m}\Omega b(e_k)db(e_k). \tag{5.1}$$

After simplification, we find

$$p(e_k) = \frac{A_k}{4\pi}\frac{\Sigma a^2}{M_\odot}\frac{1}{e_k^3}\Omega. \tag{5.2}$$

An integral over every e_k dictates the rate of change of the number of bodies with a given eccentricity, e:

$$\frac{\partial f(e,t)}{\partial t} = \int\int p(|\mathbf{e}-\mathbf{e}_n|)\left[f(e_n,t)-f(e,t)\right]d^2\mathbf{e_n}. \tag{5.3}$$

Note that this equation implicitly conserves the total particle number, $\int\int f(e,t)d^2\mathbf{e} = 1$. This can be shown by integrating both sides with respect to $\mathbf{e}$.

5.2 The Self-Similar Distribution

Without a specific eccentricity scale to dictate the evolution of $f(e,t)$, we expect a solution of the form,

$$f(e,t) = F(t)g\left(e/e_c(t)\right). \tag{5.4}$$

Replacing $f(e,t)$ in Equation 5.3 with Equation 5.4, we find,

$$\frac{1}{F(t)}\frac{dF(t)}{dt}e_c(t)g(x) - x\frac{dg(x)}{dx}\dot{e}_c(t) = \int\int p(|\mathbf{x}-\mathbf{x}_n|)\left[g(x_n)-g(x)\right]d^2\mathbf{x_n}, \tag{5.5}$$

where $\mathbf{x} = \mathbf{e}/e_c(t)$. The additional constraint that Equation 5.3 conserves particle number implies $F(t)e_c(t)^2$ is constant. This relationship simplifies the left side of Equation 5.5 such that the only possible time-dependence of each term is contained in $\dot{e}_c(t)$. The right-hand side, however, is independent of time. Therefore $\dot{e}_c(t)$ must be constant. Then,

$$e_c(t) = C_e t \text{ and } F(t) = (C_e t)^{-2}. \tag{5.6}$$

The overall normalization of $F(t)$ is arbitrary, as it can be absorbed into $g(x)$. Our choice of $F(t)$ requires $\int\int g(x)d^2\mathbf{x} = 1$ to ensure that $\int\int f(e,t)d^2\mathbf{e} = 1$ for all t. Physically, the typical eccentricity, $e_c(t)$, is set by the eccentricity change that occurs once per particle per time t, or, $e_c(t)^2 p(e_c(t))t \sim 1$. This argument sets $e_c(t)$ only up to a constant coefficient; for simplicity we choose the coefficients such that

$$e_c(t) = \frac{A_k}{2}\frac{\Sigma a^2}{M_\odot}\Omega t. \tag{5.7}$$

Previous order of magnitude arguments by Goldreich et al. (2004b) also show this scaling with Σ and t.

Finally, the profile shape, $g(x)$, is specified by the integro-differential equation

$$2g(x) + x\frac{dg(x)}{dx} + \frac{1}{2\pi}\int\int\frac{g(x_n)-g(x)}{|\mathbf{x}_n-\mathbf{x}|^3}d^2\mathbf{x}_n = 0, \tag{5.8}$$

Equation 5.8 is identical to Equation 17 of Chapter 4. A detailed description of the equation and its solution can be found in that paper. We present here a simpler and more direct derivation of the solution. We define the two-dimensional Fourier transform of $g(x)$ as $G(\mathbf{k}) = \int g(x) e^{i\mathbf{k}\cdot\mathbf{x}} d^2\mathbf{x}$. Since $g(x)$ is isotropic, $G(\mathbf{k}) = G(k)$ with $0 < k < \infty$. By taking the two-dimensional Fourier transform of Equation 5.8, we find $dG(k)/dk = -G(k)$. This simple differential equation is satisfied by $G(k) = e^{-k}$. The boundary condition $G(0) = 1$ is equivalent to our normalization of $g(x)$. The solution $g(x)$ is then

$$g(x) = \frac{1}{2\pi}\left(1 + x^2\right)^{-3/2}, \tag{5.9}$$

5.3 The Generalized Time-Dependent Distribution

In addition to the eccentricity excitation mechanism discussed in Section 5.1, it is reasonable to include a dissipative term in the Boltzmann equation that accounts for processes that reduce the eccentricities of the bodies. One relevant example of such a process is the dynamical friction caused by a collection of small bodies. The analysis of Chapter 4 examines the limit in which this dissipation balances mutual excitation: the distribution is in the shape of Equation 5.9, and its characteristic eccentricity does not evolve with time. Section 5.2 can be considered the complementary limit in which the stirring term dominates the whole expression: the distribution of Equation 5.9 increases linearly with time according to Equation 5.6. In this section we derive how the characteristic eccentricity evolves as a function of time in between these two regimes.

The full time-dependent Boltzmann equation (see Chapter 4) is:

$$\frac{\partial f(e,t)}{\partial t} = \frac{2f(e,t)}{\tau_d} + \frac{e}{\tau_d}\frac{\partial f(e,t)}{\partial e} + \int\int p(|\mathbf{e} - \mathbf{e}_n|)\left[f(e_n,t) - f(e,t)\right] d^2\mathbf{e_n}. \tag{5.10}$$

We substitute Equation 5.4 for $f(e,t)$ and retain the condition $\int\int g(x) d^2\mathbf{x} = 1$ which dictates that $F(t) = e_c(t)^{-2}$. For clarity, we also separate the eccentricity dependence from the excitation term: $p(e) \equiv Ce^{-3}$. This constant C collects the coefficients that can be read from Equation 5.2. Then Equation 5.10 becomes,

$$0 = \frac{1}{C}\left[\frac{e_c(t)}{\tau_d} + \dot{e}_c(t)\right]\left(2g(x) + x\frac{dg(x)}{dx}\right) + \int\int \frac{g(x_n) - g(x)}{|\mathbf{x} - \mathbf{x}_n|^3} d^2\mathbf{x}_n. \tag{5.11}$$

To solve this equation for all x and all t simultaneously, the x- and t- dependence must be the same for each term. Since C and the terms in square brackets contain all of the time dependence, they must together be constant in time. We choose that constant to be 2π so that the solution to this equation is consistent with our earlier definition of $g(x)$, Equation 5.9. Then $e_c(t)$ obeys the ordinary differential equation:

$$\dot{e}_c(t) + \frac{e_c(t)}{\tau_d} = 2\pi C. \tag{5.12}$$

In the limit of no damping, or $\tau_d \to \infty$, we recover the $e_c(t) = 2\pi Ct$ relation found in Section 5.2. The time-independent characteristic eccentricity of Chapter 4 is recovered by setting $\dot{e}_c(t)$ equal to zero, resulting in $e_c = 2\pi C\tau_d$. The two regimes are connected via the solution to Equation 5.12, $e_c(t) = 2\pi C\tau_d(1 - \exp(-\mathrm{t}/\tau_\mathrm{d}))$.

Equation 5.12 can be re-written in a more familiar form:

$$\frac{1}{e_c(t)}\frac{de_c(t)}{dt} = A_k \frac{9}{8\pi}\frac{\Sigma\Omega}{\rho R}\alpha^{-2}\frac{e_\mathrm{H}}{e_c(t)} - \frac{1}{\tau_d}, \tag{5.13}$$

where α is the ratio of the planet's radius to its Hill sphere and e_H is the Hill eccentricity ($e_\mathrm{H} = R_\mathrm{H}/a$). This equation, which now describes the rate at which $e_c(t)$ changes, is identical to the order-of-magnitude analysis reviewed in Goldreich et al. (2004b). However, here we find the exact numerical coefficient for the excitation rate. We also give a definite meaning to $e_c(t)$: it is the eccentricity scale of the distribution set by Equation 5.9.

We note that the derivation of Equation 5.13 does not require that Σ, R, and τ_d are constant. We can, in fact, apply the same Boltzmann equation to scenarios that include time-dependant excitation and damping rates. To demonstrate, we consider again the case of protoplanets embedded in a population of smaller planetesimals with a surface mass density of σ, and take into account the growth of the protoplanets from planetesimal accretion. Assuming that the eccentricities of the planetesimals and protoplanets are smaller than the Hill eccentricities of the protoplanets by more than $\alpha^{1/2}$, each protoplanet's radius grows at a rate (Dones & Tremaine, 1993):

$$\frac{dR}{dt} = 0.51\frac{\sigma\Omega}{\rho}\alpha^{-\frac{3}{2}}. \tag{5.14}$$

For reference, the same planetesimals damp the eccentricities of the protoplanets at a rate (Goldreich et al., 2004b):

$$\frac{1}{\tau_d} = -\frac{1}{e}\frac{de}{dt} = C_d\frac{\sigma\Omega}{\rho R}\alpha^{-2}. \tag{5.15}$$

The best estimates for the numerical coefficient of the damping timescale are from N-body integrations; Ohtsuki et al. (2002) find a value of 1.2.

We further assume that the planetesimal surface density is unaffected by the protoplanet accretion that there are no collisions between the protoplanet. In this case Σ and e_H depend on time only through the increasing radii of the protoplanets; given a constant $\dot{R}$, we have $\Sigma(t) \propto t^3$ and $e_\mathrm{H}(t) \propto t$. Therefore, the solution to Equation 5.12 is

$$e_c(t) = \left(1 + \frac{4}{1.96 C_d \alpha^{-1/2}}\right)^{-1} \frac{A_k}{C_d} \frac{9}{8\pi} \frac{\Sigma(t)}{\sigma} e_{\mathrm{H}}(t). \tag{5.16}$$

The dynamical friction rate is always faster than the growth rate of the protoplanets; thus this $e_c(t)$ is close to that of the equilibrium eccentricity distribution established at a constant R. The small fractional correction of $4/(1.96C_d\alpha^{-1/2})$ accounts for the slight growth of each protoplanet over a damping timescale. Together with Equation 5.9, Equation 5.16 gives a remarkably simple analytic expression for the time-dependent eccentricity distribution of protoplanets that excite each other and are damped by a sea of planetesimals from which they also accrete.

5.4 Numerical Simulations

The non-equilibrium distribution function of eccentricities in the shear-dominated regime can be measured directly from a full numerical simulation of the disk. We use a custom N-body integrator that evolves the changes in the two-body constants of motion of each particle around the central mass. These constants are chosen to vary slowly with small perturbations. Solving Kepler's equation for each body translates each time-step into a change in orbital phase. The constants of motion are then integrated by a fourth-order Runge-Kutta routine with adaptive time-steps (Press et al., 1992). This code is described in more detail in Chapter 2.

For this study we follow a disk of two-hundred equal mass bodies, with $m = 5 \times 10^{-9} M_{\odot}$, on initially circular orbits with randomly determined phases and semimajor axes within a small annulus of width $\Delta a = 0.8a$. To avoid possible artifacts from the edge of the simulation, we only measure the eccentricities of the bodies in the central third of the disk. A histogram of those eccentricities shows the number of bodies with each eccentricity, $e\, dN/de$. To increase the signal-to-noise ratio of the histogram at each time, we add the results of one hundred simulations with randomly generated initial semimajor axes and orbital phases.

Figure 5.1 shows the eccentricity distributions measured after three and ten orbits. The horizontal error bars indicate the width of each bin, and the vertical error bars are determined assuming that each bin is Poisson distributed. The analytic distribution function derived in Section 5.2 for each time is also plotted, as a solid line. The measured distributions agree remarkably with the analytic result.

To emphasize the self-similarity of the distribution shape, we scale the eccentricities measured at each time by the characteristic eccentricity at that time ($e_c(t)$, given by equation 5.6) and plot the shapes added together. Figure 5.2 shows that the resulting distribution shape matches the analytic form of $g(x)$ very well.

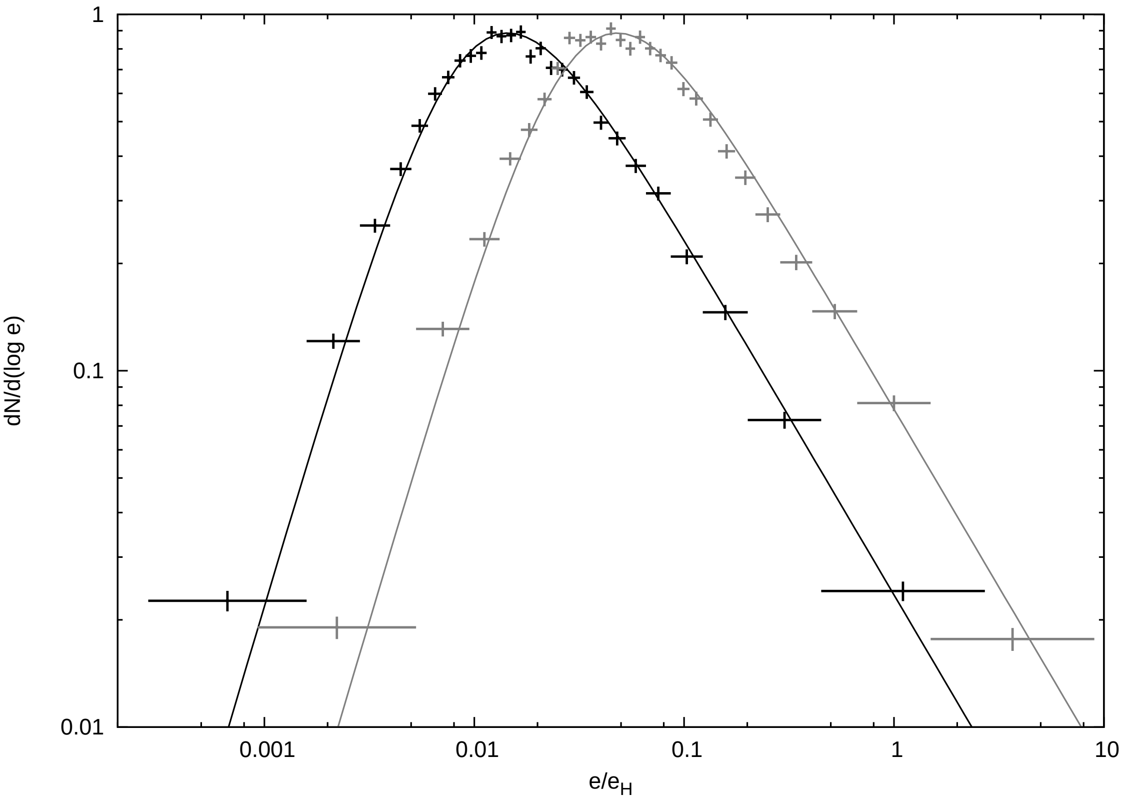

Figure 5.1 Eccentricity distributions of a shear-dominated disk of 200 particles each with a mass $m = 5 \times 10^{-9} M_{\odot}$ after three (black line) and ten (gray line) orbits. The average surface mass density of the simulated annulus is 3×10^{-3}g cm^{-2}. The vertical error bars are estimated by assuming each bin obeys Poisson statistics. The width of each bin has been chosen such that each bin contains a similar number of particles.

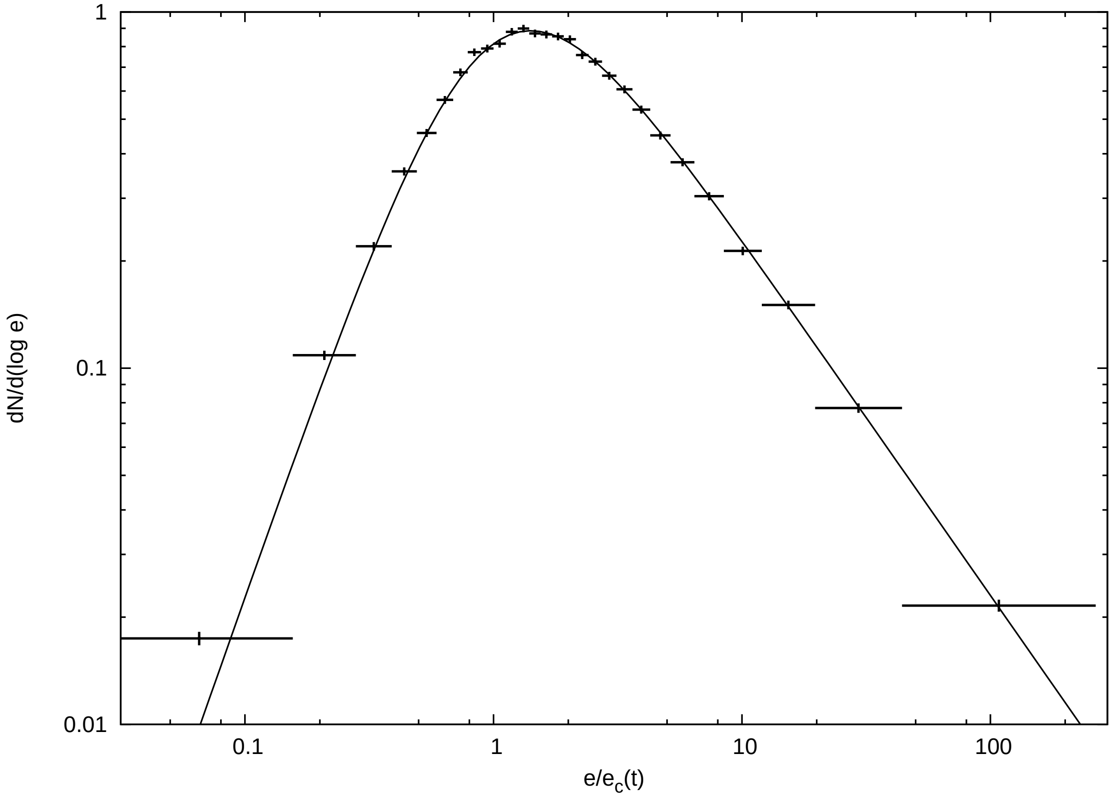

Figure 5.2 The eccentricity distribution of the same numerical simulation of Figure 5.1. Here, the distribution after one, three, and ten orbits, scaled by the characteristic eccentricity at that time are added together. The profile shape is very well described by equation 5.9, plotted as a solid line. The error bars are assigned in the same way as Figure 5.1.

5.5 Discussion

We have written a time-dependent Boltzmann equation that describes the eccentricity distribution function of a population of orbiting particles under the influence of their mutual excitations in the shear-dominated regime. Reasoning that the distribution function of eccentricities should behave self-similarly, that is, retain a constant profile while its normalization and scaling depend on time, we have decoupled the time-dependence of the eccentricity distribution from its shape. The shape is constant even in the presence of a dynamical-friction-like dissipation term. The evolution of the distribution in time can be determined generally with any time-dependent dynamical friction and excitation rates. Numerical experiments confirm this self-similarity and the analytic form of the distribution profile.

Although we have only considered disks of a single particle size, the formalism above applies trivially to disks with mass distributions. In fact, the characteristic eccentricity, equation 5.6, depends only on the total surface mass density of the disk. As long as bodies of every part of the mass spectrum are in the shear-dominated regime, the eccentricities of all bodies are drawn from the same distribution. This is a consequence of the fact that gravitational acceleration is mass-independent. In contrast, the dynamical friction of Chapter 4 depends on the size of each particle. The equilibrium distributions in that case do differ for each mass group.

Most of the disk bodies then have eccentricities of about $e_c(t)$. The mean eccentricity, $\int\int ef(e,t)d^2\mathbf{e}$, is formally infinite; in reality the mean depends logarithmically on the maximum eccentricity achievable from one interaction. Higher moments of the distribution, such as $\langle e^2 \rangle$, are dominated by the bodies with the maximum eccentricity. The random kinetic energy of the disk bodies, for example, is then set by the few bodies with the highest eccentricities regardless of the value of $e_c(t)$.

Since $e_c(t)$ is an increasing function of time, the condition of shear-dominated dynamics will be violated eventually. The interaction rate of the highest eccentricity bodies is low, so up to an order unity fraction of the bodies can have super-Hill eccentricities without affecting the shape of the sub-Hill distribution. This assumes that the disk of protoplanets is uniform to the extent that every impact parameter up to the Hill radius is well-sampled by the interactions. Then, $e_c(t)$ grows linearly all the way to the Hill eccentricity. However, if the typical separation between bodies is substantially greater than a Hill radius, $b_{\min} \gg R_{\mathrm{H}}$, then there is an upper limit in eccentricity that one interaction can provide: $e_{\max} \sim (b_{\min}/R_{\mathrm{H}})^{-2} e_{\mathrm{H}}$. The assumptions of this work then break down as $e_c(t)$ approaches $e_{\max}$.

That the shape of the distribution function is identical in the limits of non-existent or dominating dynamical friction is ultimately not surprising. In both cases the bodies in question excite their orbital parameters via the same shear-dominated viscous stirring mechanism. If dynamical friction is acting on these bodies, their eccentricities decrease with time proportionally to their magnitude. An equilibrium between excitations and this damping produces a characteristic eccentricity around which the eccentricities of all bodies are distributed. Without an agent of dynamical friction, the typical eccentricity of a body in the disk, $e_{\text{typical}} \sim e_c(t)$, grows with time. However, the ratio of the eccentricity of a particle that has not interacted recently, e, to that typical eccentricity shrinks proportionally to itself:

$$\dot{x} \equiv \frac{d}{dt}\left(\frac{e}{e_c(t)}\right) \propto -x. \tag{5.17}$$

This is formally equivalent to the damping provided by the dynamical friction we describe here and in Chapter 4.

The physical scenario we have described in this work can be viewed as a particular case of systems that achieve steady states without reaching a thermodynamic equilibrium. A general model for such behavior is that of a "driven dissipative system": particles that collide inelastically with each other but also gain energy by interacting with an external reservoir. Analytic modeling of these systems with Boltzmann equations have found velocity distributions with the same properties that we presented here, namely non-Maxwellian profiles and self-similar evolution (Ben-Naim & Krapivsky, 2002; ben Avraham et al., 2003; Ben-Naim & Machta, 2005). A more detailed study of the relationship between protoplanetary dynamics, these general models, and the physics that they represent may provide new perspectives for both fields.

We thank Yair Shokef for his enlightening comments, and the anonymous referee for several suggestions that have improved this work.

Chapter 6

Lévy Flights of Binary Orbits Due to Impulsive Encounters

Several binary Kuiper belt objects (KBOs) have well-measured small orbital eccentricities (Noll et al., 2008). Stern et al. (2003) investigate numerically the forcing of the eccentricity of the Pluto-Charon orbit by interloping KBOs. They find that the system almost never possesses an eccentricity as high as the observed value of 0.003 (Tholen et al., 2008); depending on the model of tidal damping used, they find median values of $10^{-5}-10^{-4}$. Our goal is to develop an analytic theory that describes the effects of a population of unbound perturbers on a binary orbit and can be applied simply to any binary, in the Kuiper belt or elsewhere.

The interaction of a binary system with its environment has been studied extensively in the literature (Heggie, 1975; Sigurdsson & Phinney, 1995; Yu, 2002; Matsubayashi et al., 2007; Sesana et al., 2007). One interesting context is white dwarf-pulsar binaries, which are expected to be circular. For these objects pulse timing produces very accurate measurements of their orbital motion; such measurements reveal that their eccentricities are typically very small but finite, around $10^{-4}-10^{-5}$ (Stairs, 2004). Phinney (1992) investigated the effects of passing stars on the orbit of such a binary and found that for Galactic pulsars, the perturbations are sub-dominant compared to the effects of atmospheric fluctuations in the companion star. The higher density environment of a globular cluster however can induce an order of magnitude higher eccentricity. Rasio & Heggie (1995) and Heggie & Rasio (1996) present a detailed account of the changes in orbital parameters for binaries in a stellar cluster. The work of these authors focuses on the regime where a perturbing body interacts with the binary on timescales longer than the orbital period of the binary. In the Kuiper belt, a single interaction between a binary and an unbound object occurs over a shorter timescale than the orbital period of the binary. We focus on this regime, where the perturbations to the orbital dynamics can be approximated as discrete impulses.

The main result of this work is that we have identified the perturbative evolution of the eccentricity and relative inclination of a nearly circular binary orbit as a Lévy flight, a specific type of random walk through phase space (Shlesinger et al., 1995). The entire distribution function of the eccentricity and inclination is then determined by calculating the frequency of perturbations as a function of their magnitude. We find a simple analytic expression for this distribution function.

These results were previously published in Collins, B. F. & Sari, R. 2008, AJ, 136, 2552.

We take the following steps to arrive at our conclusion. In Section 6.1 we calculate the effect of one perturber on a two-body orbit, examining separately the tidal effects of distant scatterings, close encounters with a single binary member, and direct collisions. We describe the effects of many such encounters in Section 6.2, and write a Boltzmann equation that describes the distribution function of the orbital eccentricity and the inclination of the binary relative to its initial plane. The quantitative description of the binary's evolution given by this distribution function reveals its nature as a Lévy flight. In Section 6.3, we allow for a distribution of perturbing masses and discuss the different Lévy distributions that result.

We then use the analytic theory to examine the orbits of binary KBOs being perturbed by the other members of the Kuiper belt. Section 6.4 applies our analysis to several specific Kuiper belt binaries. We briefly discuss the relevance of this theory to other astrophysical systems in Section 6.5, and summarize our conclusions in Section 6.6.

6.1 A Single Encounter

We use the following terminology to describe the geometry of the encounter between a single perturber and a two-body orbit. We refer to the two bound bodies as "the binary." The members of the binary have masses m_1 and m_2, with a total mass labeled $m_b = m_1 + m_2$ and $m_1 \geq m_2$. The position of body 2 relative to body 1 is given by $\mathbf{r}_b$, and the relative velocity by $\mathbf{v}_b$. We distinguish between the magnitude and direction of a vector with the notation $\mathbf{r}_b = r_b \hat{r}_b$. We assume $v_b \approx \Omega r_b$, where Ω is the orbital frequency of the binary. We write the orbital period as $T_{\mathrm{orb}} = 2\pi/\Omega$.

We label the mass of the perturber m_p. The position of the perturber as a function of time, $\mathbf{r}_p(t)$, is described by two vectors: $\mathbf{r}_p(t) = \mathbf{b} + \mathbf{v}_p t$. The vector $\mathbf{b}$ specifies the closest point of the perturber's trajectory to body 1, and $\mathbf{v}_p$ is velocity of the perturber relative to body 1. Each encounter geometry is uniquely specified by $\mathbf{b}$ and $\mathbf{v}_p$ under the constraint $\mathbf{b} \cdot \mathbf{v}_p = 0$. Figure 6.1 depicts the arrangement of the vectors $\mathbf{r}_b, \mathbf{v}_b, \mathbf{r}_p(t), \mathbf{b}$, and $\mathbf{v}_p$. We assume $T_{\mathrm{orb}} \gg b/v_p$ so that we may ignore the motion of the binary during the interaction. We further assume that the effects of the gravity of the binary on the perturber are small; the perturber then travels along a straight path with a constant $\mathbf{v}_p$. This assumption requires the criterion of $v_p^2 \gg G(m_b + m_p)/b$. If b is small, the perturber may collide with a member of the binary. In this case the assumption that the path of the perturber is unaffected by the gravity of the binary is true under the condition that v_p is much greater than the escape velocity of that member of the binary. The escape velocity from body 1 is defined $v_{\mathrm{esc},1}^2 = 2Gm_1/R_1$, where R_1 is the radius of body 1.

We are assuming that the timescale of the interaction is much shorter than the orbital timescale, such that the perturbation instantaneously changes the velocities of the binary objects. The impulse provided to a specific member of the binary is found by integrating the acceleration caused by the

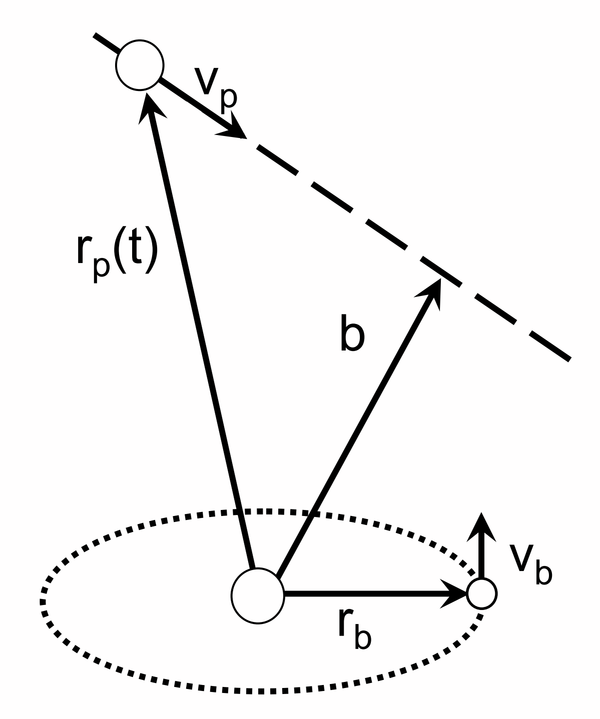

Figure 6.1 Illustration of the notation we use to denote the geometry of each perturbation. The dotted line is the almost circular orbit of the binary viewed at an angle. The dashed line is the path of the perturber, given by $\mathbf{r}_p(t) = \mathbf{b} + \mathbf{v}_p t$.

perturber over its path:

$$\Delta \mathbf{v}_j = \int_{-\infty}^{\infty} \frac{G m_p (\mathbf{b}_j + \mathbf{v}_p t)}{|\mathbf{b}_j + \mathbf{v}_p t|^3} dt = 2 \frac{G m_p}{v_p} \frac{\hat{b}_j}{b_j}, \tag{6.1}$$

where the index j specifies whether the impulse $\Delta \mathbf{v}_j$ and impact parameter $\mathbf{b}_j$ are with respect to either the primary ($j = 1$) or the secondary ($j = 2$). For the primary, $\mathbf{b}_1 = \mathbf{b}$ as we have defined it above. For encounters with the secondary, $\mathbf{b}_2$ is related to $\mathbf{b}$ by enforcing that it is also perpendicular to $\mathbf{v}_p$. Thus we find $\mathbf{b}_2 = \mathbf{b} - \mathbf{r}_b + \hat{v}_p(\mathbf{r}_b \cdot \hat{v}_p)$.

We consider the effects of such impulses on the full Laplace-Runge-Lenz vector, $\mathbf{e} = (\mathbf{v}_b \times \mathbf{H})/G m_b - \hat{r}$, where $\mathbf{H} = \mathbf{r}_b \times \mathbf{v}_b$, the angular momentum per unit mass of the binary. The vector $\mathbf{e}$ has a magnitude equal to the eccentricity of the orbit, and points from body 1 towards the periapse. It responds to a small impulse $\Delta \mathbf{v}$ according to the formula

$$\Delta \mathbf{e} = \frac{1}{G m_b} \left[2 \mathbf{r}_b (\Delta \mathbf{v} \cdot \mathbf{v}_b) - \mathbf{v}_b (\Delta \mathbf{v} \cdot \mathbf{r}_b) - \Delta \mathbf{v} (\mathbf{r}_b \cdot \mathbf{v}_b) \right], \tag{6.2}$$

keeping terms up to linear order in $\Delta \mathbf{v}$. Since we have assumed the binary has very small eccentricity, the third term in Equation 6.2 is negligible compared to the other two.

The orbital plane of the binary is defined by the angular momentum vector $\mathbf{H}$, and evolves according to $\mathbf{\Delta H} = \mathbf{r}_b \times \mathbf{\Delta v}$. The impulses affect the direction of the angular momentum vector, and therefore alter the orientation of the orbital plane of the binary. We use the two-dimensional vector $\mathbf{i}$ to denote the components of $\hat{H}$ in the plane defined by the initial angular momentum. This vector, $\mathbf{i}$, has a magnitude equal to $\sin i$, the sine of the inclination of the binary with respect to the initial orbital plane, and points from body 1 towards the longitude of the ascending node.

The change in relative velocity given by a general gravitational scattering is given by $\mathbf{\Delta v} = \mathbf{\Delta v}_2 - \mathbf{\Delta v}_1$. The resulting change in the eccentricity vector is

$$\mathbf{\Delta e} = 2\frac{m_p}{m_b}\frac{v_b}{v_p}\left[2\hat{r}_b\left(\frac{\hat{b}_2\cdot\hat{v}_b}{b_2/r_b} - \frac{\hat{b}\cdot\hat{v}_b}{b/r_b}\right) - \hat{v}_b\left(\frac{\hat{b}_2\cdot\hat{r}_b}{b_2/r_b} - \frac{\hat{b}\cdot\hat{r}_b}{b/r_b}\right)\right]. \tag{6.3}$$

The change in $\mathbf{i}$ is

$$\mathbf{\Delta i} = -2\frac{m_p}{m_b}\frac{v_b}{v_p}\left[\hat{v}_b\left(\frac{\hat{b}_2\cdot\hat{n}}{b_2/r_b} - \frac{\hat{b}\cdot\hat{n}}{b/r_b}\right)\right], \tag{6.4}$$

where $\hat{n}$ is the unit normal vector to the binary's orbital plane. For both the farthest perturbers and the closest, the dependence of Equations 6.3 and 6.4 on the impact parameter can be simplified. We discuss these limits in the following sections.

6.1.1 Close Encounters

Interactions with impact parameters greater than the radius of the primary or secondary but much less than the semi-major axis of the binary belong to what we call the "close-encounter regime." By definition the encounters in this regime of impact parameter are much closer to one member of the binary than the other. As a result the relative impulse experienced is dominated by the single impulse delivered to that body, $|\mathbf{\Delta v}| \approx |\mathbf{\Delta v}_j|$. The changes in $\mathbf{e}$ and $\mathbf{i}$ are then given not by the difference of the impulses on each body, as in Equations 6.3 and 6.4, but by the effects of only the largest impulse. For the change in eccentricity we find,

$$\mathbf{\Delta e} = 2\frac{m_p}{m_b}\frac{v_b}{v_p}\frac{r_b}{b}\left[2\hat{r}_b(\hat{b}_j\cdot\hat{v}_b) - \hat{v}_b(\hat{b}_j\cdot\hat{r}_b)\right], \tag{6.5}$$

and for the inclination,

$$\mathbf{\Delta i} = -2\frac{m_p}{m_b}\frac{v_b}{v_p}\frac{r_b}{b}\left[\hat{v}_b(\hat{b}_j\cdot\hat{n})\right]. \tag{6.6}$$

6.1.2 Distant Encounters

For interactions where $b \gg r_b$, the impulse delivered to each member of the binary is almost the same. In this limit only the tidal difference in impulse affects the eccentricity of the binary. The perturbation delivered to the lowest order in r_b/b is

$$\begin{aligned}\Delta\mathbf{e} = 2\frac{m_p}{m_b}\frac{v_b}{v_p}\left(\frac{r_b}{b}\right)^2 & \\ \left[\hat{r}_b\left(4(\hat{r}_b\cdot\hat{b})(\hat{v}_b\cdot\hat{b})+2(\hat{r}_b\cdot\hat{v}_p)(\hat{v}_b\cdot\hat{v}_p)\right)+\hat{v}_b\left(1-2(\hat{r}_b\cdot\hat{b})^2-(\hat{r}_b\cdot\hat{v}_p)^2\right)\right].\end{aligned} \tag{6.7}$$

Phinney (1992) derives the special case of this formula for interactions that take place entirely in the plane of the binary. This formula is also equivalent to Equation A24 of Heggie & Rasio (1996).

The change in $\mathbf{i}$ due to distant encounters is given by:

$$\Delta\mathbf{i} = \frac{m_p}{m_b}\frac{v_b}{v_p}\left(\frac{r_b}{b}\right)^2\hat{v}_b\left[4(\hat{r}_b\cdot\hat{b})(\hat{b}\cdot\hat{n})+2(\hat{r}_b\cdot\hat{v}_p)(\hat{v}_p\cdot\hat{n})\right]. \tag{6.8}$$

6.1.3 Collisions

Physical collisions between perturbers and body 1 or 2 cause the orbit to evolve impulsively. We define collisions to be any encounters where the impact parameter is smaller than the radius of the primary or secondary: $b < r_1$ or $b_2 < r_2$. In this case the impulse is given by the conservation of linear momentum of the encounter: $\Delta\mathbf{v} = \chi(m_p/m_j)\mathbf{v}_p$, where m_j is the mass of the binary member involved in the collision ($j = 1$ or 2). The coefficient χ accounts for the final momentum of the perturber. For an inelastic collision with $m_p \ll m_j$, $\chi = 1$. If the perturber is perfectly reflected, $\chi = 2$. The momentum loss from an impact crater can enhance this factor above 2 depending on the properties of the colliding bodies (Melosh et al., 1994). For simplicity we assume that the mass of each binary member remains unchanged after each collision.

The collisional impulse changes the eccentricity according to Equation 6.2 and the orbital plane according to the change in angular momentum $\mathbf{r}_b \times \Delta\mathbf{v}$.

6.2 Boltzmann Equation

The evolution of the eccentricity and inclination (relative to the initial orbital plane) is given by the sum of the perturbations the binary receives as it travels through a swarm of perturbers. From the average properties of the perturbing population, we can calculate a distribution function that describes the evolution of the orbit in a statistical sense.

6.2.1 Eccentricity

Since the perturbation in eccentricity is a two-dimensional vector, each component is added to the components of the existing eccentricity vector separately. As the binary experiences many perturbations, its eccentricity vector travels throughout this two-dimensional space. We write a distribution function $f(\mathbf{e}, t)$ that describes the probability that the binary will have an eccentricity in a small region $d^2\mathbf{e}$. Assuming isotropic perturbations, there is no preferred longitude of periapse for the binary. It follows that $f(\mathbf{e}, t) = f(e, t)$ and the likelihood of finding the eccentricity in a small range de around e is $2\pi e f(e, t) de$.

We define $\mathcal{R}(e')$ to be the frequency at which the binary experiences perturbations of magnitudes between e' and $e' + de'$. The frequency of perturbations with magnitudes on the order of $|\Delta\mathbf{e}| = e'$ is given schematically by $e'\mathcal{R}(e') \sim nvb^2$, where n is the number density of the perturbers, v is the speed at which the binary encounters those perturbers, and b is the distance at which the binary encounters perturbers that cause a perturbation of strength e'. We make this calculation precise with the following integral:

$$\mathcal{R}(e') = \int \delta(|\Delta\mathbf{e}(\mathbf{v}_p, \mathbf{b}, m_p)| - e')\mathcal{F}(\mathbf{v}_p, m_p) v_p \delta(\mathbf{b} \cdot \hat{v}_p) d^3\mathbf{b} d^3\mathbf{v}_p dm_p, \tag{6.9}$$

where $\mathcal{F}(\mathbf{v}_p, m_p)$ is the phase space density per unit mass of the perturbers. The integral of $\mathcal{F}(\mathbf{v}_p, m_p)$ over $d^3\mathbf{v}_p dm_p$ is the number density of the perturbers. We assume this density is uniform in the spatial dimensions and isotropic in velocity. It is normalized such that the total mass density of perturbers is given by $\rho = \int m_p \mathcal{F}(\mathbf{v}_p, m_p) d^3\mathbf{v}_p dm_p$. The factor of v_p in the integrand of Equation 6.9 represents the velocity at which the binary encounters perturbers. The second delta function in Equation 6.9 converts the volume element $d^3\mathbf{b}$ to an element of cross-sectional area. The first delta function, $\delta(|\Delta\mathbf{e}(\mathbf{v}_p, \mathbf{b}, m_p)| - e')$, restricts the integral to include only the combinations of $\mathbf{b}$, $\mathbf{v}_p$, and m_p that cause a $|\Delta\mathbf{e}| = e'$.

The evolution of the distribution function as a result of these perturbations is given by a Boltzmann equation that links the rate of change of $f(e, t)$ to the interaction frequency. We write this equation as:

$$\frac{\partial f(e, t)}{\partial t} = \int p(\mathbf{e}') \left[f(|\mathbf{e}' + \mathbf{e}|) - f(e) \right] d^2\mathbf{e}' \tag{6.10}$$

The function $p(\mathbf{e}')$ describes the frequency per unit of eccentricity space ($d^2\mathbf{e}'$) at which a binary with eccentricity $\mathbf{e}$ is perturbed to the value $\mathbf{e} + \mathbf{e}'$. Since there is no preferred direction for the encounters, this function is axisymmetric, $p(\mathbf{e}') = p(e')$. It is related to $\mathcal{R}(e')$ by integrating over the angular direction of the phase space, $\mathcal{R}(e') = \int p(e') e' d\omega = 2\pi e' p(e')$.

We first derive $p(e')$ for a simple scenario: a population of perturbers each with mass m_p and velocity v_p. To clarify this derivation, we present a qualitative treatment. The eccentricity excited by such a perturber with an impact parameter of order $b \gg r_b$ is about $e' \sim (m_p/m_b)(v_b/v_p)(r_b/b)^2$ (Section 6.1). Since the frequency of encounters with impact parameters b is proportional to b^2, and the size of the perturbation $e' \propto b^{-2}$, the frequency at which the binary is perturbed by an amount of order e' is therefore a power law: $e'^2 p(e') \propto e'^{-1}$. This power law is valid from very low

e', caused by the farthest possible impulsive encounter, to $e' \sim (m_p/m_b)(v_b/v_p)$, the rare encounters with $b \sim r_b$. We take into account the very rare occurrence of a physical collision, which excite eccentricities of order $e' \sim (m_p/m_j)(v_p/v_b)$, in Section 6.1.3.

Evaluating Equation 6.9 using $\Delta\mathbf{e}(\mathbf{v}_p, \mathbf{b}, m_p)$ given by Equation 6.7 provides the exact form of $p(e')$ for this scenario. We find:

$$p(e') = \frac{\langle C_e \rangle}{4\pi} G\rho T_{\rm orb} \frac{1}{e'^3}, \tag{6.11}$$

where $T_{\rm orb}$ is the orbital period of the binary, and $\langle C_e \rangle = 1.89$ is the average value of the angular terms of Equation 6.7 (see Appendix). We note that the frequency of perturbations depends not on m_p, but only on the total mass density of perturbers. It is also independent of v_p, as the lowered effectiveness of the faster perturbations is directly canceled by their higher frequency. These properties are typical of distant encounters with binaries, as evident in earlier work on binary dynamics (Bahcall et al., 1985).

We can generalize Equation 6.10 by including a term to account for dissipation of the binary's eccentricity: $\partial f(\mathbf{e}, t)/\partial t = -{\rm div}(f(\mathbf{e}, t)\dot{\mathbf{e}})$. We restrict our attention to mechanisms that reduce $\mathbf{e}$ at a timescale that is independent of $\mathbf{e}$, $\dot{\mathbf{e}} = -\mathbf{e}/\tau_d$. The tidal dissipation of eccentricity obeys this form and is our main motivation for including such terms.

Since $p(e')$ is a power law, we can look for self-similar solutions to the time-dependent integro-differential Boltzmann equation, Equation 6.10. The frequency of perturbations $p(e')$ does not depend on any special eccentricity, so the distribution function should depend only on the time t. We separate the distribution function into three parts: the time-dependent normalization, $F(t)$, the time-independent shape of the function, $g(x)$, and the time-dependent eccentricity scale, $e_c(t)$. These quantities obey the relation $f(e, t) = F(t)g(e/e_c(t))$. We choose the normalization of $g(x)$ such that $\int g(x) d^2x = 1$. We further choose that $f(e, t)$ be normalized to 1 for all times; this constrains the normalization function to be $F(t) = 1/e_c(t)^2$.

Substituting $f(e, t) = e_c(t)^{-2} g(e/e_c(t))$ into Equation 6.10, we find two equations. The first specifies the time-independent shape of the distribution as a function of the dimensionless parameter $x \equiv e/e_c(t)$:

$$2g(x) + x\frac{dg(x)}{dx} + \frac{1}{2\pi} \int\int \frac{g(x_n) - g(x)}{|\mathbf{x}_n - \mathbf{x}|^3} d^2\mathbf{x}_n = 0, \tag{6.12}$$

The solution to this equation has been presented in several earlier works, where we investigate the eccentricity distribution of the oligarchs in a protoplanetary disk (Collins & Sari, 2006; Collins et al., 2007):

$$g(x) = \frac{1}{2\pi}(1 + x^2)^{-3/2}. \tag{6.13}$$

This function is the two-dimensional Cauchy distribution. The median and mode of this distribution are $x_{\text{med}} = \sqrt{3}$ and $x_{\text{mode}} = 1/\sqrt{2}$. The mean of this distribution is formally divergent; assuming there is a maximum value of x, $x_u \gg 1$, then $x_{\text{mean}} \approx 2.3 \log_{10}(0.74 x_u)$.

The eccentricity scale $e_c(t)$ is set by an ordinary differential equation,

$$\dot{e}_c(t) = -e_c(t)/\tau_d + \langle C_e \rangle G \rho T_{\text{orb}}/2. \tag{6.14}$$

We note that τ_d and the terms on the right hand side of Equation 6.14 do not need to be constant in time; evolution of the binary ($T_{\text{orb}}(t)$), the perturbing swarm ($\rho(t)$), or the damping mechanism ($\tau_d(t)$) can be treated by including the time-dependence of these quantities.

We offer a reminder that $e_c(t)$ is the characteristic value of the entire distribution of eccentricity that the binary may attain. The probability is highest that the binary will have an eccentricity near the mode of the distribution, which is smaller than $e_c(t)$ by a factor of 0.7. The distribution is somewhat wide, and the confidence levels around the median value are large. The 66 percent confidence interval of x is 0.67–5.8, and the 95 percent interval is 0.23–40.0.

Equations 6.13 and 6.14 present a new picture of the stochastic evolution of the binary's eccentricity. Often the evolution of a random variable is characterized by Brownian motion, in which the distribution of the random variable is set by the long term accumulation of many small perturbations. The typical value of such a variable grows as the square-root of time (written $\sqrt{\langle x^2 \rangle} \propto t^{1/2}$), and the probability of finding the system very far away from the typical value is exponentially low. The eccentricity of the binary evolves differently. The probability of finding the binary with an eccentricity larger than $e_c(t)$ only diminishes as a power law (Equation 6.13). Physically, this reflects the probability that the binary received a single large perturbation to that state. The characteristic eccentricity, $\sim e_c(t)$ corresponds to the size of the perturbation that occurs with a frequency of about $1/t$. The linear growth of $e_c(t)$ demonstrated by Equation 6.14 reveals that the eccentricity of the binary does not reflect the accumulation of many small perturbations, but the single largest perturbation occurring in its history. This kind of random walk is called a "Lévy flight" (Shlesinger et al., 1995).

6.2.2 Inclination

The same analysis applies to the changes in angular momentum of the binary. Since $|\Delta \mathbf{i}| \sim |\Delta \mathbf{e}|$, it follows that $p(i') \sim p(e')$. The evolution of inclination differs only in the coefficients that depend on the geometrical configuration of the encounter. The calculation of the coefficients is described in the Appendix. The self-similar distribution shape is a function of the dimensionless variable $i/i_c(t)$, where $i_c(t)$ is the time-dependent characteristic inclination. The following equation describes the evolution of $i_c(t)$:

$$\dot{i}_c(t) = -i_c(t)/\tau_{d,i} + \langle C_i \rangle G\rho T_{\mathrm{orb}}/2 \tag{6.15}$$

where we have used $\tau_{d,i}$ to distinguish the timescale at which the inclination of the binary is damped, and $\langle C_i \rangle = 0.75$, the average of the angular terms in Equation 6.8. The inclination is always measured relative to the orbital plane at $t = 0$. The distribution given by Equation 6.13 then describes the probability of the binary being inclined by $i = x\ i_c(t)$ relative to its original orbital plane.

6.3 A Spectrum of Colliding Perturbers

For many physical applications we must consider a range of perturbing masses and velocities and the effects of collisions onto the binary. In the single mass case discussed in Section 6.2.1, the interaction frequency $p(e')$ is set by the likelihood that the binary encounters a perturber at the impact parameter that causes such a change of e'. For perturbers that have different masses, the chance of experiencing a perturbation of magnitude e' depends on the combined likelihood that the perturber has the required impact parameter and the required mass to excite such a change.

To extend our analysis we set up several pieces of notation. We assume that the mass and velocity distributions are independent: $\mathcal{F}(m_p, v_p) = \mathcal{F}_v(v_p)\mathcal{F}_m(m_p)$. We restrict our analysis to velocity distributions with a characteristic value, v_0, such as a Gaussian distribution. We consider systems with differential mass spectra characterized by a power law: $\mathcal{F}_m(m_p) \propto m_p^{-\gamma}$, valid from a minimum mass m_{min} to a maximum m_{max}. These functions are consistent with conditions in the Kuiper belt, where a power law mass spectrum and roughly Gaussian velocity spectrum are observed (Luu & Jewitt, 2002). We define the differential mass spectrum by

$$\mathcal{F}_m(m_p) = (n_0(\gamma - 1)/m_0)(m_0/m_p)^{\gamma}, \tag{6.16}$$

where n_0 is the number density of bodies larger than mass m_0. In the literature the differential size spectrum of Kuiper belt objects is characterized as a power law in radius with index q; this is related to our index by $\gamma = (q + 2)/3$. In this section we discuss the $p(e')$ and $p(i')$ that result from several values of γ.

6.3.1 $\gamma < 2$

The total mass density of perturbers for $\gamma < 2$ is dominated by the perturbers with the largest mass, m_{max}. While perturbations of size e' are excited by all of the perturbers, the most likely perturber to cause a perturbation of this strength is the largest mass perturber. The dynamics of the binary are then the same as described in Section 6.2.1 with $m_p = m_{\mathrm{max}}$. The power law of $p(e') \propto e'^{-3}$, based on distant encounters, is valid up to the eccentricity excited by a perturber of mass m_{max}

interacting at a $b \sim r_b$, or for $e' \ll (m_{\rm max}/m_b)(v_b/v_p)$ (Equation 6.7). It is necessary only to know the total mass density ρ of the perturbing swarm in order to calculate the excitation frequency in this scenario, given by Equation 6.11.

6.3.2 $\gamma = 2$

The power law $\gamma = 2$ describes a special mass distribution where the frequency of encountering the few large perturbers at large impact parameters is the same as encountering the more abundant smaller perturbers at smaller impact parameters. Thus each logarithmic interval in impact parameter contributes the same amount to the frequency of perturbations by e', $p(e')$. The upper limit of impact parameters that can contribute to excitations of a given e', however, is given by the maximum mass perturber. The total range of contributing impact parameters then diminishes as e' approaches the eccentricity caused by the largest perturber interacting with $b \sim r_b$, $e'_{\rm max} \equiv (m_{\rm max}/m_b)(v_b/v_0)$. Mathematically this behavior is determined by the integral of Equation 6.9, which yields an excitation frequency of:

$$p(e') = \frac{G n_0 m_0 T_{\rm orb}}{e'^3} \frac{\log\left(2.1(e'_{\rm max}/e')\right) \langle C_e \rangle}{4\pi}, \tag{6.17}$$

for $e' \ll e'_{\rm max}$. The equivalent formula for the inclination excitations is:

$$p(i') = \frac{G n_0 m_0 T_{\rm orb}}{i'^3} \frac{\log\left((e'_{\rm max}/i')\right) \langle C_i \rangle}{4\pi}. \tag{6.18}$$

For the smallest e' and i', the entire range of perturbing masses contributes to the interaction frequency. This occurs for excitations of the order $(m_{\rm min}/m_b)(v_b/v_0)$, below which the perturbation frequency is given by Equation 6.11.

6.3.3 $2 < \gamma < 3$

The mass density of the perturbers when $2 < \gamma < 3$ is dominated by perturbers of the smallest mass, $m_{\rm min}$. Distant encounters by perturbers with this mass produce very small perturbations; for very low e' then, $p(e') \propto e'^{-3}$, given by the simple model of Section 6.2.1. The upper limit of e' caused by these perturbers interacting with impact parameters $b \sim r_b$ is $e' \sim (m_{\rm min}/m_b)(v_b/v_p)$.

Perturbers with $m_{\rm min}$ cause eccentricity changes larger than this via close encounters, but these encounters are less frequent than interactions with perturbers of a higher mass and an impact parameter of order r_b. Perturbations with a strength $(m_{\rm min}/m_b)(v_b/v_p) \gg e' \gg (m_{\rm max}/m_b)(v_b/v_p)$ are most often excited by perturbers with impact parameters of $\sim r_b$ and masses $m \sim e'(v_p/v_b)m_b$. In other words the frequency of perturbations is directly proportional to the slope and normalization of the mass spectrum.

In this case, the functions $p(e')$ and $p(i')$ cannot be determined using the simplifications to Equation 6.3 afforded by very small or very large impact parameters. In general, the perturbation frequency for a mass spectrum of $2 < \gamma < 3$ follows the power law $p(e') \propto e'^{-(\gamma+1)}$. As an example we present the perturbation frequency for $\gamma = 25/12$. This corresponds to $q = 4.25$, the best fit to observations of the Kuiper belt size distribution presented by Fraser et al. (2008). We calculate from Equation 6.9,

$$p(e') = 2.6 \frac{G n_0 m_0 T_{\rm orb}}{e'^{37/12}} \left(\frac{m_0}{m_b} \frac{v_b}{v_0} \right)^{1/12}. \tag{6.19}$$

It is simple to understand the relationship between Equations 6.11 and 6.19 with the following argument. A perturbation of size e' that occurs via an interaction at a distance r_b requires a perturber of mass about $m' \sim e'(v_0/v_b)m_b$. If we interpret the total density in Equation 6.11 as only the density in bodies around m', then $\rho' \sim m' \mathcal{F}_m(m') \sim n_o(m_0/m')^{\gamma-1}$, and we recover the scaling of Equation 6.19.

The integral over b and the angular variables of Equation 6.4 yield a different coefficient for the perturbations to inclination:

$$p(i') = \frac{G n_0 m_0 T_{\rm orb}}{i'^{37/12}} \left(\frac{m_0}{m_b} \frac{v_b}{v_0} \right)^{1/12}. \tag{6.20}$$

We relegate to the appendix the details of the integrals that produce the coefficients of Equations 6.19 and 6.20.

6.3.4 Collisional Perturbations

The integral of Equation 6.9 over impact parameters from 0 to r_j produces the frequency of perturbations to the binary by collisions on member j. Since the size of the impulse from a collision does not depend on the impact parameter, it is the mass of the perturber that dictates the size of the eccentricity perturbation. Accordingly, the frequency of perturbations as a function of e' reflects the frequency of collisions as a function of m_p. The frequency of collisional perturbations does not depend on $m_{\rm max}$ or $m_{\rm min}$ regardless of the slope. However, the limits of the mass distribution specify the lowest and highest perturbations achievable via collisions: $\chi(m_{\rm min}/m_j)(v_0/v_b) \leq e' \leq \chi(m_{\rm max}/m_j)(v_0/v_b)$. In this range of e', for any value of γ, the perturbation frequency due to collisions is

$$p(e') = \frac{G n_0 m_b T_{\rm orb}}{e'^{\gamma+1}} \left(\chi \frac{m_0}{m_j} \right)^{\gamma-1} \left(\frac{v_0}{v_b} \right)^{\gamma} \left(\frac{r_j}{r_b} \right)^2 V_\gamma \frac{(\gamma-1)\langle D_e^{\gamma-1} \rangle}{2\pi}, \tag{6.21}$$

where $\langle D_e^{\gamma-1} \rangle$ is the average of the angular dependence of $\Delta \mathbf{e}$ from collisions to the power of $\gamma - 1$, and $V_\gamma \equiv v_0^{-\gamma} \int v_p^{\gamma+2} \mathcal{F}_v(v_p) dv_p$. If $\mathcal{F}_v(v_p)$ is proportional to a delta function, $\delta(v_p - v_0)$, then $V_\gamma = 1$ for all γ. If the velocity spectrum were Gaussian, such that $\mathcal{F}_v(v_p) \propto \exp(-(v_p/v_0)^2)$, then

$V_\gamma = 2\Gamma((3+\gamma)/2)/\sqrt{\pi}$. The frequency of perturbations to the relative inclination by collisions is the same as Equation 6.21, replacing the integrated coefficient $\langle D_e^{\gamma-1}\rangle$ with the appropriate calculation made from the coefficients of $|\Delta\mathbf{i}|$.

Although we use r_j to represent either member of the binary, it is clear from Equation 6.21 that the collisions onto the smallest body have the largest effect on the orbit. The ratio of the perturbation frequency through collisions, $p(e')_{\text{collisions}}$ (Equation 6.21) to the frequency of gravitational scatterings, $p(e')_{\text{gravity}}$ (Equation 6.19), is, for mass distributions of $2 < \gamma < 3$,

$$\frac{p(e')_{\text{collisions}}}{p(e')_{\text{gravity}}} = 0.03\left(\frac{r_j}{r_b}\right)^2\left[\chi\frac{m_b}{m_j}\left(\frac{v_0}{v_b}\right)^2\right]^{\gamma-1}, \tag{6.22}$$

where we have evaluated the coefficients for $\gamma = 25/12$. The choice of γ does not change these coefficients dramatically.

6.3.5 Eccentricity Distributions

The distribution given by Equations 6.13 and 6.14 were derived in the context of $p(e') \propto e'^{-3}$. As long as $p(e')$ follows a power law with e', we can write a self-similar distribution function $f(e,t)$. We write a generic function, $p(e') = P_0 e'^{-(1+\eta)}$, to account for the different slopes caused by different mass distributions (for $3 > \gamma > 2$, $\eta = \gamma$; for $\gamma < 2$, $\eta = 2$). The derivation of the distribution function proceeds analogously as in Section 6.2.1. Equation 6.10 becomes two equations: a dimensionless integro-differential equation that specifies the shape, and an ordinary differential equation to specify the evolution of the eccentricity scale $e_c(t)$. The general version of Equation 6.14 is:

$$\dot{e}_c(t) = -e_c(t)/\tau_d + 2\pi P_0/e_c(t)^{\eta-2}. \tag{6.23}$$

In the limit of no eccentricity dissipation ($\tau_d \to \infty$), Equation 6.23 shows that $e_c(t) \propto t^{1/(\eta-1)}$. For all of the $p(e')$ discussed in Section 6.3, the growth of $e_c(t)$ is always faster than $t^{1/2}$.

The shape of the distribution function is determined through a Fourier transform of the general version of Equation 6.12. For slopes of $1 < \eta < 3$, $g(x) = \int \cos(\mathbf{k}\cdot\mathbf{x})\exp(-|\mathbf{k}|^{\eta-1})d^2\mathbf{k}$ (Sato, 1999; Collins et al., 2007). While there is only a closed form solution for $\eta = 2$, given by Equation 6.13, all of these functions are flat at low x and fall off like $x^{-(\eta+1)}$. In fact, it is easy to show from Equation 6.10 that the high e tail is given by

$$f(e \gg e_c(t)) = p(e)t/(\gamma - 1), \tag{6.24}$$

when $t \ll \tau_d$. For equilibrium distributions where $\dot{e}_c(t) = 0$, t is replaced with τ_d, the timescale for the dissipation.

When $p(e') \propto e'^{-4}$ or steeper, the accumulation of the smallest perturbations over time is more effective at raising the eccentricity of the binary than single large perturbations. In this case, the evolution of the eccentricity follows standard Brownian motion, where the distribution function is a Gaussian, and $e_c(t) \propto t^{1/2}$.

6.4 Kuiper Belt Binaries

In this section we compute $e_c(t)$ and $i_c(t)$ for several Kuiper belt binaries. The "binary" of Section 6.1 now refers to a bound pair of Kuiper belt objects, and the "perturbers" are all of the other members of the Kuiper belt.

For the highest mass KBOs, the size spectrum is well determined to be a power law with an index slightly greater than $q = 4$. The lowest mass bodies, of about 30 km in radius, are less frequent than predicted by a single power law, however the parameters of a more general model are still under investigation (Trujillo & Brown, 2001; Luu & Jewitt, 2002; Pan & Sari, 2005; Fraser et al., 2008; Fuentes & Holman, 2008). For this section we use the best fit of a single power law model to the high mass part of the spectrum provided by Fraser et al. (2008), who find $q = 4.25$ and a number density of 1 body per square degree brighter than magnitude 23.4. We assume an average distance of 40 AU to the Kuiper belt and a depth of 20 AU to find a volumetric number density $n_0 = 3 \times 10^{-41}$ cm^{-3}. To convert the magnitudes of the objects to physical sizes, we assume a constant geometric albedo of 0.04, a constant physical density of 1 g cm^{-3}, and take the R-band apparent magnitude of the Sun to be -27.6. We find that the magnitude 23.4 corresponds to a mass $m_0 = 1.75 \times 10^{21}$ g, equivalent to a radius of 75 km. Most of the objects found between 30–50 AU are inclined by about 5–15 degrees relative to the plane of the solar system, and have heliocentric eccentricities of 0.1–0.2.

6.4.1 Perturbations by a Disk

Our analysis so far has treated the perturbing bodies as unbound objects moving relative to the binary with a constant velocity. When the perturbers are part of a disk orbiting the central star, the orbital elements of the disk set the parameters of the perturbation frequencies we calculate in Section 6.2.

The relative velocity between KBOs, when they interact, is set by the size of their eccentricities and inclinations, $v_p \sim e_H a \Omega_H$, where the subscript "H" denotes a heliocentric orbital quantity. We assume a constant perturbing velocity with $v_p = 1$ km/s, which corresponds to the typical heliocentric eccentricities and inclinations of KBOs. We assume that these encounters occur isotropically in the frame of a binary, however this is not accurate. A more detailed calculation of the angular distribution of relative velocities will only affect the coefficients of the perturbations. The disk does not specify a special direction for the perturbation vector $\mathbf{\Delta e}$, so the perturbing frequency and the distribution function retain their axisymmetry. The influence of the central star on the binary and the perturbers adds another constraint to our assumption of impulsive encounters: the timescale for an interaction must be shorter than the orbital period around the star: $b/v_p \ll 1/\Omega_H$, or equivalently, $b \ll e_H a$. This guarantees that the relative velocity is constant during the interaction.

If the orbit of the binary is much different than the typical KBO orbit, there are several modifications to perturbation frequencies experienced by the binary. One modification is due to the finite height of the disk of perturbers. This height is set by their inclinations around the central star; for the Kuiper belt we refer to the average inclination as $\langle i \rangle_{KB}$. A binary with heliocentric inclination $i_{\rm CoM} \ll \langle i \rangle_{KB}$ never travels above or below the perturbing disk height and therefore experiences the maximal frequency of perturbations. If $i_{\rm CoM} \gg \langle i \rangle_{KB}$, the binary spends most of its orbit outside of the perturbing swarm. The frequency of perturbations to such a binary is reduced by the fraction of the time the binary leaves the disk, proportional to $\langle i \rangle_{KB}/i_{\rm CoM}$. The eccentricity of the binary in the disk reduces the effective density of perturbers in a similar manner if the epicycle of the binary carries it outside of the region populated by perturbers.

If the heliocentric eccentricity or inclination of the binary is much greater than the typical values for the Kuiper belt, the relative velocity between the binary and a perturber is primarily due to the non-circular heliocentric motion of the binary. Gravitational interactions depend weakly on v_0 so their frequency does not change much in this case. Perturbations by collisions, however, become more important if v_0 is increased due to this effect (Equation 6.22).

6.4.2 Pluto et al.

Pluto is the second largest known Kuiper belt object, with a radius of about 1100 km. It has a semi-major axis of 39.5 AU and its orbit is inclined relative to the ecliptic by 17°. Its largest satellite, Charon, contains about one tenth of the total mass of the system. Recent observations have revealed two smaller satellites, Nix and Hydra (Weaver et al., 2006). These satellites have small eccentricities and are roughly co-planar with Charon. Numerical simulations of collisions between similarly sized objects by Canup (2005) produce binaries with orbits similar to Pluto and Charon. The circularity and co-planarity of Nix and Hydra lend additional weight to a collisional origin of the system.

The triple system of Pluto and its moons is a valuable test case for the dynamics we have presented. For an isolated binary it is impossible to know the initial orbital plane. The relative inclinations of the moons of Pluto can be measured directly assuming their formation was co-planar. Furthermore, the perturbing swarm for all three Pluto-moon pairs is the same. A major issue in comparing our analytic calculations to the observations is that the large mass ratio of Charon to Pluto causes significant non-Keplerian effects in the orbits of the outer satellites. We first re-examine the published observational model of their orbits to separate the relevant motion of the outer satellites from the forced motion due to Charon. We then compare the resulting eccentricity with our predicted values.

6.4.2.1 Orbital Model of Tholen et al.

A model of the observations of the Pluto system has been presented by Tholen et al. (2008), who fit the parameters of a four-body numerical integration such that the simulation agrees with the observations. Such work is necessary, as it has been shown that the observations cannot be consistently modeled by three non-interacting two-body orbits (Weaver et al., 2006).

The model of Tholen et al. (2008) presents a full set of osculating elements describing the orbits of Charon, Nix, and Hydra. The orbit of Charon is virtually unaffected by Nix and Hydra; Tholen et al. (2008) measure the eccentricity of Charon to be $3.48 \pm 0.04 \times 10^{-3}$, and the period of its orbit is 6.387 days. Since the combined potential of Charon and Pluto is significantly non-Keplerian, the elements of Nix and Hydra vary significantly during their orbits. Tholen et al. (2008) average the osculating semi-major axis to find an orbital period for these satellites of 25.49 days and 38.73 days for Nix and Hydra, respectively. The osculating eccentricities of Nix and Hydra both oscillate between zero and about 0.2; for each satellite oscillations at the frequencies of its own orbit and that of Charon are visible (their Figure 4). The orbital planes of the satellites relative to Charon's are tilted by 0.15 degrees for Nix and 0.18 degrees for Hydra. Each plane precesses relative to the plane of Charon, however the angle of the offset remains constant.

6.4.2.2 A Different Interpretation

For two body motion, the Keplerian elements are constant and indicate the shape of the orbit in space. Osculating elements that describe motion in significantly non-Keplerian potentials, such as the combined potential of Pluto and Charon, may vary on timescales shorter than the orbital period of the satellite. When this is true, relating the osculating elements to the shape of the orbit can be misleading. The average value of the osculating eccentricity of Nix is 0.015 in the model of Tholen et al. (2008), however the motion of Nix relative to Pluto never resembles an ellipse with such an eccentricity.

We re-examine the model provided by Tholen et al. (2008) by reproducing the numerical integration based on the Pluto-centric positions and velocities of Charon, Nix, and Hydra published in their Table 1. We set the masses of Nix and Hydra to zero to eliminate their secular interactions with each other. Instead of examining the osculating elements, we adopt the approach of Lee & Peale (2006) and characterize the orbits of Nix and Hydra based on their position as a function of time from the Pluto-Charon barycenter, plotted in Figure 6.2. The units of distance are Pluto radii, defined as $R_P = 1147$ km.

Although short oscillations on the timescale of Charon are visible in the top panel of Figure 6.2, they are very small compared to the oscillations that occur on the timescale of Hydra's orbital

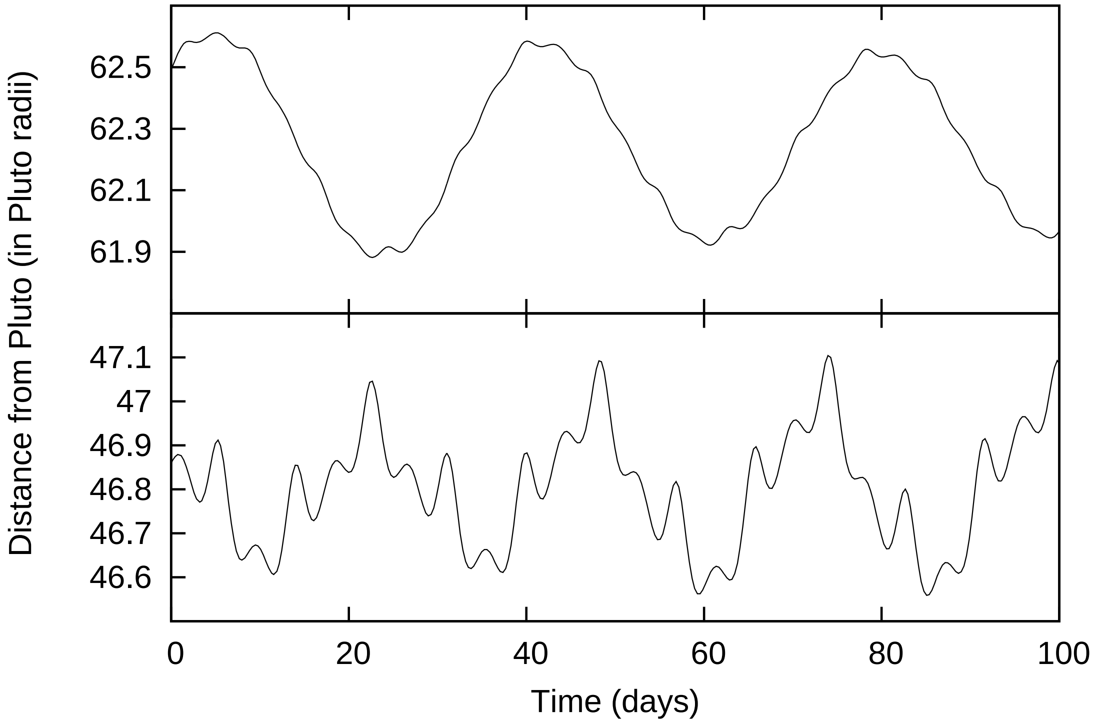

Figure 6.2 Distance of Nix (lower panel) and Hydra (upper panel) from the Pluto-Charon barycenter, in units of Pluto radii, as a function of time, in an integration of the parameters found by Tholen et al. (2008). Nix and Hydra are treated as massless test particles. The origin of the time coordinate is arbitrary.

period. To parametrize Hydra's orbit we fit the function $r_0(1 + e\cos(\kappa_1 t + \omega_1))$ to the first 200 days of the numerical model. Because for a non-Keplerian potential the radial epicyclic frequency differs from the orbital frequency, we calculate the average angular frequency by fitting a straight line to the angular position of Hydra as a function of time, $f(t) = \Omega_1 t + \lambda_0$. The results are written in Table 6.1. We interpret e_1 as the orbital degree of freedom in the combined potential of Pluto and Charon that is analogous to the eccentricity of a two-body orbit.

The motion of Nix (bottom panel of Figure 6.2) appears more irregular than that of Hydra. We find the position of Nix to be well-described by a model of three epicycles with different frequencies: $r(t) = r_0(1 + \sum_{k=1,2,3} e_k \cos(\kappa_k t + \omega_k))$. The best fit values are printed in Table 6.1. We distinguish the cause of each epicycle by its period. The combined potential of Pluto and Charon oscillates with frequency of $\Omega_{\rm Charon} - \Omega_{\rm Nix}$; motion being forced by this potential should occur on integer multiples of this frequency. Using the numbers in Table 6.1, we see that $2\pi/(\Omega_{\rm Nix} + \kappa_2) = 2\pi/(\Omega_{\rm Nix} + \kappa_3/2) = 6.39$ days. The second and third epicycles in our fit correspond to motion at the first and second harmonic of Nix's relative orbital frequency. We therefore interpret the first term, with a size of $e_1 = 3 \times 10^{-3}$

Table 6.1 Best fit values to the epicyclic models of the radial motion of Nix and Hydra

	r_0/R_P	e_1	$2\pi/\kappa_1$	e_2	$2\pi/\kappa_2$	e_3	$2\pi/\kappa_3$	$2\pi/\Omega_1$
		$\times 10^{-3}$	(days)	$\times 10^{-3}$	(days)	$\times 10^{-3}$	(days)	(days)
Nix	46.805(5)	2.96(3)	25.22(2)	1.25(3)	8.599(8)	1.38(3)	4.298(1)	24.8505(5)
Hydra	62.237(1)	5.595(2)	38.535(15)					38.20(1)

Note — The motion of Nix is fit with three epicyclic terms, while the motion of Hydra is only fit with one. The parenthesis indicate the 95% confidence level of the fit around the last digits.

and a period close to Nix's orbital period, as analogous to the two-body eccentricity.

We perform another integration of the best fit initial conditions from Tholen et al. (2008) to investigate the secular effects between Nix and Hydra. We use the best fit masses from Tholen et al. (2008) for the two outer satellites. Since the motion of Hydra is dominated by a single epicyclic frequency, the variation in the size of its epicycle is apparent on the timescale of several years. To determine the effect of secular variations on Nix, we fit the same three-component epicyclic model to five orbits at $t \sim 5$ years. In the best-fit model to these later orbits, the only difference compared to the model of table 6.1 is in e_1, the epicycle with a frequency close to Hydra's orbital frequency. This is further confirmation that the degree of freedom represented by e_1 is analogous to the two-body eccentricity.

6.4.2.3 Theoretical Distribution

To compute the distribution of eccentricities and inclinations expected of Pluto's moons, we solve Equation 6.23 for each of the moons, given the interaction frequencies specified by Equations 6.19 and 6.20. The only remaining parameters to evaluate are the damping timescales for the eccentricity and inclinations of each satellite. We use the standard formula for the damping of eccentricity due to the tidal force of the primary acting on a secondary that is in synchronous rotation (Yoder & Peale, 1981; Murray & Dermott, 1999):

$$\tau_{d,2} = \frac{4}{63} Q_2 (1 + \tilde{\mu}_2) \frac{m_2}{m_1} \left(\frac{r_b}{r_2} \right)^5 \frac{1}{\Omega}, \tag{6.25}$$

where Q_2 is the dissipation function of the secondary, and $\tilde{\mu}_2 = 19 \mu r_2 / (2 \rho G m_2)$ is its effective rigidity, a ratio between the material strength of the secondary and its self-gravity. The damping rate of eccentricity due to tides of the primary acting on the secondary, $\tau_{d,1}$, if the primary is also rotating synchronously with the orbit of the satellite, is given by Equation 6.25 with the quantities specific to the primary switched with those of the secondary and vice versa.

Pluto and Charon are known to be in a double-synchronous state of rotation, where the spin period of each body is equal to the 6.4 day orbital period. In many binaries, only the spin of the secondary is synchronous with the orbital period. Tides on the primary then raise the eccentricity. Double-synchronous systems, however, experience damping due to both the tides on the secondary and those on the primary. Assuming a water-ice composition for Pluto ($\mu = 4 \times 10^{10}$ dynes cm^{-2}), we calculate the eccentricity damping timescale due to tides raised by Charon, $\tau_{d,1}$ from Equation 6.25 to be 5.1 Myrs. The shortest damping timescale due to tides from Pluto acting on Charon, $\tau_{d,2}$ is found by assuming Charon is also made of water-ice; we find in this case a timescale of 8.2 Myr. The longest timescale assumes a rocky composition ($\mu = 6.5 \times 10^{11}$ dynes cm^{-2}); we find this corresponds to 133 Myr. The overall damping of the system is given by the sum of the damping rates. The short damping timescale of tides on Pluto prevents Charon from contributing significantly to the combined effect of both tides, reducing the importance of its composition. The longest eccentricity damping timescale that results from both tides is 4.9 Myr. The inclinations of the outer satellites relative to the Pluto-Charon plane are also damped by tidal dissipation. For a circular synchronous orbit the timescale for inclination damping is longer than the timescale for eccentricity damping by a factor of $\sim i^{-2}$. We ignore the damping of inclinations in Equation 6.15 for all three satellites.

As discussed in Tholen et al. (2008) and Section 6.4.2.2, secular interactions between the satellites are visible in the long term calculations of their orbits. For the best-fit values of the masses of Nix and Hydra, their eccentricities are modulated on the order of 10% over timescales of years; we neglect these fluctuations for this work. It is more important in this model to determine whether secular evolution can cause the eccentricity of Nix or Hydra dissipate via Charon's orbit.

We use linear secular theory to describe the coupled evolution of the eccentricity and longitude of periapse of each satellite (Murray & Dermott, 1999). We find that the undamped secular evolution agrees qualitatively with the numerical orbit determinations. We add a term to the differential equations describing Charon's eccentricity that reduces it at a constant timescale ($\dot{e}_{\text{Charon}} = -e_{\text{Charon}}/\tau_d$). The frequencies of the oscillations of the eigenmodes of the solution are practically unchanged by this term, however each eigenmode gains a dissipative factor. Quantitatively, only one eigenmode is damped on timescales shorter than than 4.5 Gyr. By integrating the damped secular equations with different initial periapses, we determined that the secular interactions do not cause substantial damping of Nix and Hydra.

Equation 6.22 gives the frequency of perturbations due to collisions of perturbers onto each moon relative to the frequency of perturbations caused by gravitational scattering, Equation 6.19. For Charon, the collisional perturbations increase $p(e)$ by only 2 percent. Since Nix and Hydra are smaller, perturbations by collisions have a greater relative effect; however it is only a 20 percent contribution to the total perturbation frequency for Nix and 15 percent for Hydra. We solve Equation 6.23 to find $e_c(t)$ and $i_c(t)$ for each of Pluto's moons.

For Charon we find $e_c = 2.6 \times 10^{-6}$, and $i_c = 0.029°$. This value of e_c corresponds to the most likely perturbation during a damping timescale of 4.9 Myr, and is much smaller than the observed value of 3.5×10^{-3} (Tholen et al., 2008). Using Equation 6.24, we calculate that given this value of e_c, the probability of Charon's eccentricity being as high as its observed value is 0.2 percent.

For Nix we calculate $e_c(4.5 \text{ Gyr}) = 4.8 \times 10^{-3}$ and $i_c(4.5 \text{ Gyr}) = 0.1°$, and for Hydra, 7.1×10^{-3} and $0.15°$, respectively. The distributions specified by these values are quite consistent with the free eccentricity we determine in Table 6.1.

6.4.3 Other Interesting KBOs

Two other Kuiper belt objects have satellites on low eccentricity orbits: 2003 EL$_{61}$, and Eris. Along with Pluto these are three of the four most massive KBOs known, all with radii of about 1000 km. 2003 EL$_{61}$has two known satellites. The largest has a 50 day orbit and a measured orbital eccentricity of 0.050$\pm$0.003 (Brown et al., 2005). An additional smaller satellite orbits 2003 EL$_{61}$ with a period of about 35 days (Brown et al., 2006). The orbital parameters of the inner satellite are unconstrained, however the relative inclination between the two is about 40°. The masses of the satellites are negligible compared to the mass of 2003 EL$_{61}$. The heliocentric inclination of the system is 28°.

Brown et al. (2005) argue that if the tidal response of 2003 EL$_{61}$ and its large satellite are fluid-like, tidal interactions should damp their eccentricity on a timescale of about 300 Myr. With these parameters we use Equation 6.23 to calculate an equilibrium $e_c = 4.3 \times 10^{-4}$. The distribution with this eccentricity scale predicts an observed eccentricity of 0.05 at a probability of three percent. However, for smaller bodies, internal elastic forces dominate the tidal deformation of their shape; it is more reasonable to assume that the tidal response of the satellite is characterized by its material strength. Then, the tides raised on the primary have the greatest effect and the eccentricity of the system grows on the same timescale as the growth of the semi-major axis. Forced eccentricity growth and an evolving orbital period can be incorporated into Equation 6.23. However, these corrections are only an order unity correction since the growth timescale, by definition, is comparable to the age of the system. Assuming T_{orb} is fixed and ignoring the eccentricity growth, we calculate $e_c(4.5 \text{ Gyr}) = 0.0052$. The 95 percent confidence interval around this e_c is 0.001–0.2; the observed eccentricity of 2003 EL$_{61}$is within this range.

The dwarf planet Eris is orbited by the satellite Dysnomia. Observations have shown an upper limit to their eccentricity of 0.013 (Brown et al., 2006). The system has a 15 day orbital period, and orbits the sun at a semi-major axis of 67.7 AU with an eccentricity of 0.44 and a heliocentric inclination of 44°. In addition to the reduction in effective perturbing density caused by the inclination, the high eccentricity reduces the effective perturber density by an additional factor of 0.09. The semi-major axis of the binary is consistent with 4.5 Gyr of tidal evolution away from an initially very close orbit; if the tidal response of the secondary that of a strength-less fluid, then its eccentricity is damped on a timescale of 50 Myr. These parameters yield an $e_c = 2.2 \times 10^{-6}$. However, if the material strength of the secondary is stronger than its own self-gravity, then the tides raised on the primary cause the eccentricity of the satellite to grow. In this case the relevant timescale is the age of the system, and we find that $e_c(4.5 \text{ Gyr}) = 1.0 \times 10^{-4}$. Both values are below the observed upper limit.

In addition to the high mass ratio and low eccentricity Kuiper belt binaries, there are other known binaries of almost equal mass on moderately eccentric orbits. The binary 1998 WW$_{31}$ is an example of such an object: both members have a radius of about 50 km, an orbital period of 574 days, and a mutual eccentricity is 0.817 (Veillet et al., 2002). Even though our analysis is derived in the low eccentricity limit, we can use Equation 6.23 to estimate approximately the eccentricity expected from impulsive encounters; we find $e_c(4.5 \text{ Gyr}) = 0.31$. This moderate characteristic eccentricity is consistent with the high observed value. Other binaries with orbital periods on the order of a year will have acquired large eccentricities through their interactions with the other Kuiper belt objects.

6.5 Other Binary Systems

Our analysis holds for any two-body orbit perturbed isotropically in the impulsive limit. As binary orbits are prevalent in astrophysics, we briefly discuss several other examples.

The asteroid belt harbors many binaries with well determined eccentricities. The mass spectrum of the asteroid belt, however, is much shallower than that of the Kuiper belt: the largest asteroid, Ceres, contains a third of the total mass of all asteroids. A binary asteroid is then perturbed mostly by the largest objects that it encounters. To calculate $p(e')$ accurately, it is necessary to model the neighborhood of that binary. The asteroid belt is also collisionally active so its binaries may not be coeval with the whole solar system. We postpone a detailed analysis of the binary asteroid population for a future work.

A well-measured class of binaries outside the solar system are millisecond pulsars with white dwarf companions. The tidal damping between the pulsar and its companion in the phase before the companion becomes a white dwarf is very short, indicating that during this phase the eccentricity of the binary should be smaller than the observed values of around $10^{-4} - 10^{-5}$ (Stairs, 2004). To explain the observations, Phinney (1992) presents the following model. As the companion star becomes a white dwarf, random fluctuations in the atmosphere of the star cause irregular motion in the orbit of the binary. These motions are reflected by a small eccentricity that remains since the tidal interactions between the white dwarf and the neutron star cannot damp the system. The model of Phinney (1992) produces eccentricities for these systems that match the observations well.

These binaries are perturbed by encounters with other stars in the galaxy; we can calculate the contribution to their eccentricities by the distant stellar interactions. The perturbation of these systems by other stars falls into the simple regime of only distant interactions described in Section 6.2.1. A typical volumetric mass density for field stars is $0.1\text{M}_\odot \text{ pc}^{-3}$ (Holmberg & Flynn, 2000). Given this density, we calculate the characteristic eccentricity of these systems to be

$$e_c(t) = 1.2 \times 10^{-9} \left(\frac{T_{\text{orb}}}{1 \text{ day}}\right) \left(\frac{t}{1 \text{ Gyr}}\right) \left(\frac{\rho}{0.1 M_\odot \text{ pc}^{-3}}\right). \tag{6.26}$$

Typical orbital periods are between 1 and 10 days, and the ages of these systems are on the order of Gyrs. We find then that $e_c(t)$ is several orders of magnitude lower than the observed eccentricities. Phinney (1992) also concludes that the perturbations from other stars cannot be responsible for the eccentricities of the binary pulsars. Since we have calculated the distribution, however, we can estimate more accurately the likelihood of achieving these eccentricities by only distant stellar perturbations: less than 0.1 percent.

Globular clusters can have densities many orders of magnitudes higher than the average galactic density, such that distant perturbations to the binaries may be important. However, in a cluster the interactions between a binary and a star are not typically in the impulsive interaction regime. Instead the orbits of the perturbers are affected by the gravity of the binary, and the interactions occur over several orbital periods. Analytic work on the eccentricity perturbations in this regime has been performed by Rasio & Heggie (1995) and Heggie & Rasio (1996).

The characteristic eccentricity caused by distant stellar passages on the orbits of extra-solar planets is also given by Equation 6.26. These eccentricities are too low to be reflected in the current sample of known extra-solar planets. As with the pulsar binaries, the distant interactions may play a role in setting the eccentricity distribution of long period planets found in a dense stellar cluster. For most extra-solar planets however, planet-disk interactions (Goldreich & Sari, 2003) or planet-planet scatterings (Rasio & Ford, 1996) are probably the source of their eccentricity.

6.6 Conclusions

We have calculated the effects of impulsive perturbations and collisions on a nearly circular Keplerian orbit. If the swarm of perturbers encounter the binary isotropically in space, we can write a distribution function that describes the probability density for the binary to have a given eccentricity or inclination relative to its initial plane. The growth rate of the binary's likeliest eccentricity and inclination depends on the mass spectrum of the perturbers. For shallow mass distributions ($q < 4$) it is the distant encounters that set the binary's eccentricity and only the total mass density of perturbers is important to the evolution of the binary. For steeper mass distributions of $q = 4 - 7$, it is the interactions at about the semi-major axis of the binary that dominate the frequency of perturbations. Only the normalization and slope of the mass spectrum set the distribution of eccentricities in this regime.

The assumptions of this model are valid in the Kuiper belt. Our calculations match the observations of Nix and Hydra very well. For Eris and 2003 EL_{61}, the observations lie within the 95 percent confidence intervals of the distributions we calculate, assuming the tidal response of the secondaries is dominated by material strength. For Charon our theory is consistent with the numerical simulations of Stern et al. (2003), predicting an eccentricity about 3 order of magnitudes smaller than observed. However, our analysis alleviates their need for numerical simulations as well as predicts the entire distribution of the eccentricity. The distributions measured by Stern et al. (2003) are not all correct as their model includes only impact parameters out to twice the semi-major axis. In their simulations where $q = 3.5$ and 4.0 this excludes the impacts that are most relevant over an eccentricity damping timescale. Our results show that for $q = 3.5$ the interactions that dominate Charon's eccentricity are Pluto-sized perturbers interacting at about 200 times the semi-major axis!

Even without eccentricity dissipation through tides, perturbations from other Kuiper belt objects are too weak to excite eccentricities of order 1 or inclination changes of order a radian for binaries that have orbital periods of a few days or weeks. It is not likely that the orbital planes of the close binaries have been affected significantly by other Kuiper belt objects given our current understanding of the history of the Kuiper belt. It falls on theories of binary formation to explain the distribution of orbital inclinations relative to the ecliptic for close binaries. Since $e_c(t)$ grows faster for binaries with large orbital periods, it is plausible that the smaller wide binaries (1998WW$_{33}$ for example) have been brought to large eccentricities and inclinations by interacting with the rest of the Kuiper belt.

When many binaries share the same perturbing swarm, such as in the Kuiper belt, we can use the eccentricities of all the binaries to probe the properties of the entire system. For example, if the mass spectrum is steeper than $q = 4$, the distribution of eccentricity is directly related to the slope and normalization of the mass spectrum. Conversely, the observed eccentricity can be used to place limits on the damping timescale of a binary and therefore the rigidity of those bodies. The small sample of Kuiper belt binaries with well measured eccentricities limits the current effectiveness of such a calculation. However, the Pan-STARRS project plans to detect around 20000 more members of the Kuiper belt (Kaiser et al., 2002); from these the number of orbit-determined Kuiper belt binaries will surely increase.

The distribution we describe with Equation 6.13 is a special case of a Lévy distribution (Sato, 1999). This class of functions arise in the generalization of the central limit theorem to variables distributed with an infinite second moment. Alternatively, these functions can be characterized by the properties of the Lévy flight they describe. For the eccentricity of the binaries discussed in this work, the frequency of a step is inversely proportional to a power of its size that depends on the mass spectrum of perturbers. It follows that the largest single step dominates the growth from accumulated smaller steps, causing, in the absence of damping, the typical eccentricity to grow faster than in a normal diffusive random walk. The slope of the distribution of excitations dictates the shape of the distribution. This explains the coincidence of the distribution we derive in this work being exactly that of the distribution of eccentricity of protoplanets in a shear-dominated planetesimal disk, where the probability of changing the eccentricity of a protoplanet is inversely proportional to the size of that change (Collins & Sari, 2006; Collins et al., 2007).

The authors thank Dmitri Uzdensky and Scott Tremaine for valuable discussions.

6.7 Appendix

To calculate the excitation rates presented in Sections 6.2 and 6.3, it is necessary to integrate over all possible configurations of angles $\mathbf{b}$ and $\mathbf{v}_p$ relative to $\mathbf{r}_b$ and $\mathbf{v}_b$. In this appendix we clarify the relation between the coefficients and Equations 6.3 through 6.8.

We choose spherical polar coordinates for $\mathbf{b}$ and $\mathbf{v}_p$ to integrate Equation 6.9. This requires a polar and azimuthal angle for $\mathbf{b}$, θ_b and ϕ_b, and a polar and azimuthal angle for $\mathbf{v}_p$, θ_v and ϕ_v. By defining θ_v relative to $\mathbf{b}$, the requirement that $\mathbf{b}$ and $\mathbf{v}_p$ be perpendicular fixes $\theta_v = \pi/2$.

The magnitude of the perturbation only depends on the vectors $\mathbf{b}$ and $\mathbf{v}_p$ relative to $\hat{r}_b$ and $\hat{v}_b$, so we use these vectors and their cross product, $\hat{n}$ to describe the components of $\hat{b}$: $\hat{b} = b_r\hat{r}_b + b_v\hat{v}_b + b_n\hat{n}$. The components are related to θ_b and ϕ_b in the typical way: $b_r = \cos\phi_b \sin\theta_b$, $b_v = \sin\phi_b \sin\theta_b$, and $b_n = \cos\theta_b$. We define the components of $\mathbf{v}_p$ relative to the same unit vectors. The angle ϕ_v describes the direction of $\mathbf{v}_p$ in the plane given by $\hat{b}$; the components of $\mathbf{v}_p$ follow from a rotation of this plane to align with $\hat{n}$. We find the relations:

$$\begin{aligned} v_r &= b_n \cos\phi_v - b_v(b_r \sin\phi_v - b_v \cos\phi_v)/(1+b_n), \\ v_v &= b_n \sin\phi_v + b_r(b_r \sin\phi_v - b_v \cos\phi_v)/(1+b_n), \\ v_n &= -b_r \cos\phi_v - b_v \sin\phi_v. \end{aligned} \tag{6.27}$$

The coefficient from Equations 6.11 and 6.17, $\langle C_e \rangle$, is defined to be the integral of $|\Delta\mathbf{e}|/(8\pi^2(m_p/m_b)(v_b/v_p)(r_b/b)^2)$ as given by Equation 6.7:

$$\langle C_e \rangle = \frac{1}{4\pi^2}\int_0^{2\pi}\int_0^{2\pi}\int_0^{\pi} \left[(4b_rb_v + 2v_rv_v)^2 + (1 - v_r^2 - 2b_r)^2\right]^{1/2} \sin\theta_b d\theta_b d\phi_b d\phi_v = 1.89. \tag{6.28}$$

We similarly define $\langle C_i \rangle$ from Equation 6.8:

$$\langle C_i \rangle = \frac{1}{4\pi^2}\int_0^{2\pi}\int_0^{2\pi}\int_0^{\pi} |2b_rb_n + v_rv_n| \sin\theta_b d\theta_b d\phi_b d\phi_v = 0.75. \tag{6.29}$$

To calculate the coefficients used in the collisional excitation rate, Equation 6.21, we use the $|\Delta\mathbf{e}|$ discussed in Section 6.1.3.

$$\langle D_e^{\gamma-1} \rangle = \frac{1}{4\pi^2}\int_0^{2\pi}\int_0^{2\pi}\int_0^{\pi} (4v_v^2 + v_r^2)^{(\gamma-1)/2} \sin\theta_b d\theta_b d\phi_b d\phi_v \tag{6.30}$$

For $\gamma = 2$, the integral has a closed form solution of $\langle D_e \rangle = E(-3)$, the complete Elliptic integral.

For the inclination,

$$\langle D_i^{\gamma-1} \rangle = \frac{1}{4\pi^2} \int_0^{2\pi} \int_0^{2\pi} \int_0^{\pi} |(v_z)^{\gamma-1}| \sin\theta_b d\theta_b d\phi_b d\phi_v = \frac{1}{\gamma} \tag{6.31}$$

The coefficients for the excitation rates in the regime of $2 < \gamma < 3$ are more complicated as the dependence on b/r_b cannot be factored out of the coefficient. In addition to integrating over all angles, we must integrate over impact parameter. For any γ, Equation 6.19 is written:

$$p(e) = \frac{G n_0 m_0 T_{\rm orb}}{e^{\gamma+1}} \left(\frac{m_0}{m_b} \frac{v_b}{v_0} \right)^{\gamma-2} \frac{\gamma-1}{2\pi} V_{2-\gamma} \langle A_e^{\gamma-1} \rangle, \tag{6.32}$$

where $V_{\gamma-2}$ is discussed in Section 6.3.4; for a Gaussian distribution of perturber velocities, $V_{\gamma-2} = 2\Gamma((1+\gamma)/2)$. The term $\langle A_e^{\gamma-1} \rangle$ again contains the angular information. Excitations for $2 < \gamma < 3$ are most important at $b \sim r_b$ so we can not assume that $\mathbf{b}_2 \approx \mathbf{b}$. We introduce explicit notation for the the components of the unit vector $\hat{b}_2 = b_{2,r}\hat{r}_b + b_{2,v}\hat{v}_b + b_{2,n}\hat{n}$. Then the angular average coefficient is:

$$\langle A_e^{\gamma-1} \rangle = \frac{1}{8\pi^2} \int_0^{2\pi} \int_0^{2\pi} \int_0^{\pi} \int_0^{\infty} \tag{6.33}$$
$$\left[16 \left(\frac{b_{2,v}}{x_2} - \frac{b_v}{x_1} \right)^2 + 4 \left(\frac{b_{2,r}}{x_2} - \frac{b_r}{x_1} \right)^2 \right]^{(\gamma-1)/2} x_1 \sin\theta_b dx_1 d\theta_b d\phi_b d\phi_v,$$

with $x_1 = b/r_b$ and $x_2 = b_2/r_b$. The magnitude and components of $\mathbf{b}_2$ are related to $\mathbf{b}$ and $\mathbf{v}_p$ as described in Section 6.1: $\mathbf{b}_2 = \mathbf{b} - \mathbf{r}_b + \hat{v}_p(\mathbf{r}_b \cdot \hat{v}_p)$. For $\gamma = 25/12$ as discussed in 6.3.3, $\langle A_e^{13/12} \rangle \approx 15$. For other γ between 2 and 3, this factor is of the same order, 10–15.

Chapter 7

A Unified Theory for the Effects of Stellar Perturbations and Galactic Tides on Oort Cloud Comets

In the same work as he proposed the existence of a large reservoir of comets in the outskirts of the solar system, Oort (1950) suggested a two-stage process for the creation of such a cloud. First, perturbations from the planets increase the semimajor axes of nearby smaller objects. These interactions leave the periapses of the small bodies in the planetary region, but will eventually deliver enough energy to eject them from the solar system. The second stage of Oort cloud formation requires that perturbations external to the solar system deliver angular momentum to the comets. This raises their periapses out of the realm of planetary influence and saves them from eventual ejection. Further perturbations are necessary to lower their periapses again so that they can return to the planetary region and be observed from Earth.

Oort's original suggestion for both the circularization and delivery mechanisms is the influence of other stars in the Galaxy as they encounter the solar system. Each star that passes the solar system delivers a small kick to each comet that depends on the mass of the star, its velocity, and its distance of closest approach. Heisler & Tremaine (1986) explored the effects of a large scale planar symmetry in the swarm of stellar perturbers to find a smooth torque similar in magnitude to or even dominant over the stochastic stellar perturbations. This effect is known as the "Galactic tidal torque," since it can be attributed to the gradient of the average potential of the Galactic disk. Several groups have used numerical simulations to investigate the formation of the Oort cloud from a combination of stellar perturbations and Galactic tides (Duncan et al., 1987; Dones et al., 2004); in all cases the two effects have been implemented separately.

Recent studies have provided analytic solutions to several other stochastic scattering problems that arise in orbital dynamics and planet formation (Collins & Sari, 2006; Collins et al., 2007). Collins & Sari (2008) investigated the evolution of an initially circular orbit interacting impulsively with unbound perturbers. They showed that the probability per unit time of perturbing a circular orbit to an eccentricity of order e is proportional to e^{-1}. This power law is enough to determine that the eccentricity of the binary diffuses as a Lévy process, and the scale of the distribution grows linearly with time (Shlesinger et al., 1995). Such evolution is fast compared to the common Brownian

---

These results have been submitted to the Astronomical Journal.

motion-type diffusion where the distribution evolves as only the square-root of time.

In this work, we apply the framework developed for perturbations around nearly circular orbits in Collins & Sari (2008), presented in this thesis as Chapter 6, to the case of perturbations around nearly radial orbits. Section 7.1 presents the effects of a single stellar passage on a zero angular momentum comet. In Section 7.2 we derive and solve the Boltzmann equation that describes the accumulation of the changes in angular momentum from an isotropic distribution of perturbers. Section 7.3 describes the perturbations that arise from an anisotropic velocity distribution, and explains the connection between the effects of stellar encounters and the tidal force from the Galactic potential. Section 7.4 summarizes our conclusions.

7.1 A Single Stellar Passage

In this section we discuss the change in angular momentum, eccentricity, and periapse of a comet on a nearly radial orbit. We call the central body of the system the "sun." We denote the position of the comet as $\mathbf{r}_b(t)$, and its velocity $\mathbf{v}_b(t)$. We write the magnitude of $\mathbf{r}_b(t)$ as $r_b(t) = |\mathbf{r}_b(t)|$, and the unit vector as $\hat{r}_b(t) = \mathbf{r}_b(t)/r_b(t)$. Since a radial orbit is by definition a straight line, $\hat{r}_b(t)$ is constant in time. Furthermore, the direction of the velocity, $\hat{v}_b(t)$, is either aligned or anti-aligned with $\hat{r}_b$. The orbital energy per unit mass of the comet, $\mathcal{E}$, sets the semimajor axis, a, and the orbital period, $T_{\rm orb}$. The angular momentum vector, $\mathbf{J}$ is zero, and the eccentricity vector is then given by $\mathbf{e} = \mathbf{v}_b \times \mathbf{J}/(GM_\odot) - \hat{r}_b = -\hat{r}_b$. Finally, determining the position of the comet as a function of time requires specifying the time that the comet passes through periapse, τ.

We call each perturber a "star," and write the velocity of the star $\mathbf{v}_p$. The mass of the star, m_p, will typically be about the same magnitude as $M_\odot$, the mass of the sun; both are very large compared to the mass of the comet, m_c. We focus this analysis on the regime where the path of the star is unaffected by the gravity of the Sun, or $GM_\odot/(bv_p^2) \ll 1$. Then the position of the perturber as a function of time is given by $\mathbf{r}_p(t) = \mathbf{b} + \mathbf{v}_p(t - t_0)$, where $\mathbf{b}$ describes the closest position of the star relative to the sun and t_0 is the time at which the star reaches this position.

We first consider encounters between the star and the sun that occur with $b \gg 2a$, such that the perturbation to the sun-comet system can be treated in the tidal limit. In this case the tidal acceleration as a function of time is given by:

$$\mathbf{a}_T(t') = Gm_p r_b(t') \left[\frac{\hat{v}_p(\hat{r}_b \cdot \hat{v}_p) - \hat{r}_b}{(b^2 + (v_p t')^2)^{3/2}} - 3\frac{(\mathbf{b} + \mathbf{v}_p t)(\mathbf{b} \cdot \hat{r}_b)}{(b^2 + (v_p t')^2)^{5/2}} \right], \tag{7.1}$$

where we have translated the time coordinate by t_0 to simplify the expression.

The acceleration caused by each passing star affects the shape of the comet's orbit. Since the angular momentum is initially zero, the small impulses have a large relative effect on $\mathbf{J}$. In contrast, single perturbations to $\mathbf{e}$ and a are always small compared to their initial magnitudes. The periapse of the comet, which is important for determining the influence of the planets on the comet, is related to the angular momentum, $J = \sqrt{2GM_{\odot}q}$. For these reasons, we focus on understanding the effects of the stellar perturbations on the angular momentum vector.

To find the total change in angular momentum for one stellar passage, we integrate the acceleration over the motion of the star and of the comet: $\mathbf{\Delta J} = \int \mathbf{r}_b(t') \times \mathbf{a}_T(t')dt'$. There are two limiting cases where we can evaluate this integral to find a closed-form solution. The first is the impulsive regime, where $b/v_p \ll T_{\rm orb}$. The comet spends most of its time with $r_b \sim a$; however, for rare interactions that occur when $r_b(t) \ll a$, impulsiveness requires $b/v_p \ll r_b(t)/v_b(t)$. We treat the comet as stationary over the duration of an impulsive perturbation: $r_b(t') = r_b(t_0)$, and find the change in angular momentum to be:

$$\Delta\mathbf{J}(t_0) = \frac{2Gm_p r_b(t_0)^2}{v_p b^2}\left[(\hat{r}_b \times \hat{v}_p)(\hat{r}_b \cdot \hat{v}_p) - 2(\hat{r}_b \times \hat{b})(\hat{r}_b \cdot \hat{b})\right]. \tag{7.2}$$

The other simplifying case is a very non-impulsive encounter ($b/v_p \gg T_{\rm orb}$). When each orbit is very short relative to the timescale of the perturbation, the acceleration at each point along the perturber's path is experienced by the entire span of the comet's orbit. The disparate timescales in this regime allows the integral over the motion of the comet to be separated from the integral over the path of the star. The result is a $\mathbf{\Delta J}$ that is independent of t_0 and τ:

$$\Delta\mathbf{J} = \frac{5}{2}\frac{Gm_p}{v_p}\left(\frac{a}{b}\right)^2\left[(\hat{r}_b \times \hat{v}_p)(\hat{r}_b \cdot \hat{v}_p) - 2(\hat{r}_b \times \hat{b})(\hat{r}_b \cdot \hat{b})\right]. \tag{7.3}$$

This result also follows from replacing $r_b(t_0)^2$ in Equation 7.2 with its time averaged value, $\langle r_b^2 \rangle = (5/2)a^2$.

7.2 Lévy Flight Behavior

Successive perturbations cause the angular momentum delivered to the comet to accumulate. Individual perturbations add to the existing angular momentum vectorially: $\mathbf{J}_{\rm new} = \mathbf{r}_b \times (\mathbf{v}_b + \mathbf{\Delta}v) = \mathbf{J} + \Delta\mathbf{J}$. Holding $\hat{r}_b$ constant restricts the angular momentum vector to a plane. We accordingly treat $\mathbf{J}$ as a two-dimensional vector throughout this work. Since the perturbations by passing stars occur randomly, we employ the same statistical approach as Chapter 6. We study the evolution of $\mathbf{J}$ by deriving a distribution function, $f(\mathbf{J}, t)$, that specifies the probability that the comet will have an angular momentum within the region $d^2\mathbf{J}$ around $\mathbf{J}$ at time t. If we assume that the perturbations occur isotropically, there is no preferred direction for the accumulated angular momentum of the comet. We then expect that $f(\mathbf{J}, t) = f(J, t)$. The probability of finding the comet's angular momentum with a magnitude between J and dJ in any direction is $2\pi f(J, t)JdJ$. We relax the assumptions of isotropy in Section 7.3.

We express the probability density function (PDF) for single perturbations as a frequency per unit angular momentum, $\mathcal{R}(J')$. This function describes the probability per unit time that the comet receives a perturbation with a magnitude between J' and $J' + dJ'$. Given the properties of the ensemble of perturbing stars, we compute the frequency with the following expression:

$$\begin{aligned}\mathcal{R}(J') & \\ &= \int \delta(|\Delta \mathbf{J}(\mathbf{v}_p, \mathbf{b}, t_0, m_p)| - J')\mathcal{F}(\mathbf{v}_p, m_p) v_p \delta(\mathbf{b} \cdot \hat{v}_p) d^3\mathbf{b} d^3\mathbf{v}_p dm_p d(t_0/T_{\mathrm{orb}}).\end{aligned} \tag{7.4}$$

where the function $\mathcal{F}(\mathbf{v}_p, m_p)$ is the combined phase space density of perturbers in $\mathbf{v}_p$ and m_p, normalized such that the total mass density of perturbers in real space is $\rho = \int m_p \mathcal{F}(\mathbf{v}_p, m_p) d^3\mathbf{v}_p dm_p$. This equation is analogous to Equation 9 of Chapter 6, and is a precise formulation of the idea that the frequency at which the comet is perturbed by an amount of order J' is calculated by $J'\mathcal{R}(J') \sim nvb^2$, where n is the number density of perturbers, v is the velocity at which they encounter the sun-comet system, and b^2 is the cross-sectional area for such an encounter. In words, Equation 7.4 integrates over the entire parameter space of the encounter geometry ($\mathbf{v}_p, \mathbf{b}, t_0$, and m_p), weights the integral by the probability density of each parameter, and uses the delta function of $|\Delta J(\mathbf{v}_p, \mathbf{b}, t_0, m_p)|$ to select those geometries that produce a perturbation of size J'.

The frequency of perturbations is linked to the distribution function through a Boltzmann equation:

$$\frac{\partial f(J,t)}{\partial t} = \int p(\mathbf{J}')[f(|\mathbf{J}' + \mathbf{J}|) - f(J)] d^2\mathbf{J}'. \tag{7.5}$$

As in Chapter 6, the function $p(\mathbf{J}')$ describes the frequency per unit angular momentum space ($d^2\mathbf{J}'$) at which a comet with angular momentum $\mathbf{J}$ is perturbed to $\mathbf{J} + \mathbf{J}'$; this is the PDF of $\mathbf{J}'$. We expect this frequency to depend only on the magnitude of the perturbation and not the direction, $p(\mathbf{J}') = p(J')$, for isotropic perturbers. It is related to $\mathcal{R}(J')$ by integrating $p(J')$ over the angular component of $\mathbf{J}'$, $\mathcal{R}(J') = 2\pi J' p(J')$.

We assume that the stellar perturbers have only one mass, m_p, and one velocity, v_p, that can point in any direction. The calculation of $p(J')$ then proceeds similarly to the calculation presented in Chapter 6. Since the angular momentum excited by a perturber is proportional to m_p, v_p, and b in all the same ways as the excitation of eccentricity in a nearly circular binary, $J' \propto m_p/(v_p b^2)$ from Equations 7.2 and 7.3, it follows that $J'\mathcal{R}(J') \propto J'^{-1}$, and $p(J') \propto J'^{-3}$.

The full calculation of $p(J')$ requires choosing the correct expression for $\Delta \mathbf{J}$ given the timescale of the encounters. In the extremely non-impulsive regime (Equation 7.3), $\Delta \mathbf{J}$ is averaged over $r_b(t)$ before being used in Equation 7.4. For the impulsive case, $\Delta \mathbf{J}(t_0)$ retains its dependence on the position of the comet, but the subsequent integral over t_0 in Equation 7.4 averages the contribution of perturbers from all possible r_b. Ultimately we arrive at the same $p(J')$ for both non-impulsive and very impulsive perturbations:

$$p(J') = 0.74 G\rho a^2 \frac{1}{J'^3}, \tag{7.6}$$

where $\rho = nm_p$, the volumetric mass density of the perturbers in space. As noted in Chapter 6, this form of $p(J')$ reveals that the angular momentum of the comet follows a Lévy flight (Shlesinger et al., 1995). The distribution function is then:

$$f(J,t) = \frac{1}{2\pi J_c^2(t)}(1 + (J/J_c(t))^2)^{-3/2}. \tag{7.7}$$

This function is self-similar, meaning that it always has the same shape centered around a characteristic angular momentum scale, $J_c(t)$, that changes with time. We have chosen the normalization such that $\int f(J,t) d^2\mathbf{J} = 1$ at all times. The characteristic angular momentum is near the median of the distribution, $J_{\text{median}} = \sqrt{3} J_c(t)$. Since the probability of finding the comet with an angular momentum of order $J \gg J_c(t)$ falls off like the power law J^{-1}, the mean, variance, and all higher moments of the distribution are undefined. The mean only diverges logarithmically; if there is a maximum angular momentum $J_{\max}$, then $J_{\text{mean}} = 2.3 J_c(t) \log_{10}(0.74 J_{\max}/J_c(t))$.

The time derivative of $J_c(t)$ is related to the perturbation frequency:

$$\dot{J}_c(t) = 4.66 G\rho a^2 \tag{7.8}$$

This equation is derived by substituting the solution for $f(J,t)$ (Equation 7.7) into the Boltzmann equation (Equation 7.5). Equation 7.8 determines $J_c(t)$ even if the parameters of the perturbing swarm (ρ) or the comet (a) are changing with time. During the formation of the Oort cloud, the semimajor axes of the comets evolve as the ice giants deliver orbital energy to them over many interactions. Additionally, a time-varying density of perturbers may be relevant if the Sun formed in a dense cluster (Fernandez, 1997). The high eccentricity but high periapse orbit of Sedna may imply that the Sun was born in such an environment (Morbidelli & Levison, 2004; Brasser et al., 2006; Kaib & Quinn, 2008). A realistic statistical description of the formation of the Oort cloud must incorporate the evolution of ρ and a of the comets.

To provide the following simple numerical example, we assume a constant ρ and a. The angular momentum distribution function in this case grows linearly with time, $J_c(t) = 4.66 G\rho a^2 t$, for $J_c(t) \gg J_c(t=0)$. Using values relevant for the Oort cloud, we find

$$\frac{J_c(t)}{J_{\text{circ}}} = 0.363 \left(\frac{\rho}{0.1 M_\odot \text{pc}^{-3}}\right) \left(\frac{a}{10^4 \text{AU}}\right)^{3/2} \left(\frac{t}{1\text{Gyr}}\right), \tag{7.9}$$

where we have scaled $J_c(t)$ by the angular momentum per unit mass of a circular orbit, $J_{\text{circ}} =$

$\sqrt{GM_\odot a}$, to make it dimensionless. Since our derivations neglect the non-radial motion of the comet's evolving orbit, our theory is only quantitatively correct for $J/J_{\rm circ} \ll 1$.

This mode of growth is qualitatively different from the typical diffusive random walk. The passing stars cause a spectrum of perturbations that occur with frequencies inversely proportional to their size ($J'\mathcal{R}(J') \propto J'^{-1}$). This power law is such that the smallest kicks cannot accumulate fast enough to affect the distribution function. For example, perturbations of about the same size accumulate as a normal diffusive random walk, $\delta J \propto \sqrt{t/t_{\rm small}} J'_{\rm small}$. In that same time, however, the comet receives, on average, a single perturbation of size $\delta J \approx J'_{\rm big} \propto (t/t_{\rm small}) J'_{\rm small}$. Thus the overall growth of the angular momentum is due to the few largest perturbations that occur over a time t.

The distribution in angular momentum (Equation 7.7) can be converted to a distribution for the comet's periapse distance, q, using the relation for nearly radial orbits, $J = \sqrt{2GM_\odot q}$:

$$f(q,t) = \frac{1}{2q_c(t)} (1 + q/q_c(t))^{-3/2}, \tag{7.10}$$

where $q_c(t)$ is the characteristic periapse associated with $J_c(t)$. We have chosen a normalization such that $\int f(q,t)dq = 1$. Since $J_c(t) \propto t$, the typical periapse distance grows as t^2; the timescale for a significant change in periapse then depends on the comet's current q.

These derivations of the distribution of a comet's angular momentum assumed the swarm of perturbers had a single individual mass and single velocity. If there are other massive perturbers with $m_p > M_\odot$, such as giant molecular clouds, Equations 7.7 and 7.9 describe the distribution when ρ includes all of the perturbers: $\rho = \sum n_i m_{p,i}$, where n_i and $m_{p,i}$ are the volumetric number density and masses of the ith group of perturbers. A mass spectrum that extends significantly below the mass of the Sun also affects the probability distribution of the perturbations. In the generalized case, the slope of the perturbation spectrum sets the high J power law of the distribution function. As long as the exponent of $J'\mathcal{R}(J')$ is between 0 and -2, the angular momentum follows a Lévy flight (Shlesinger et al., 1995). For the precise details of deriving $p(J')$ and $f(J',t)$ given a general mass distribution, we refer the reader to Chapter 6.

7.3 Connection to Galactic Tides

In deriving the model presented in Section 7.2, we have assumed that the perturbing stars are distributed isotropically in $\hat{v}_p$ and uniformly in impact parameter. We then expect the angular momentum distribution to be axisymmetric. However, this assumption about the velocity distribution implies a spherically symmetric spatial distribution. This is not an accurate description of the field stars, which are confined to a disk with a height much less than its radial dimensions.

Heisler & Tremaine (1986) investigated the effects of the large scale potential arising from the Galactic disk. We reproduce their derivation of such a torque given a simple planar model of the mass distribution. We approximate the disk as a stack of infinitely thin, infinitely large sheets of mass. Gauss' law shows that the sheets above and below both the sun and the comet produce no net acceleration on the system. The sheets that pass in between the sun and comet however, produce a mean torque given by:

$$\dot{\mathbf{J}} = -2\pi G\rho(\mathbf{r}_b \cdot \hat{z})(\mathbf{r}_b \times \hat{z}), \tag{7.11}$$

where ρ is the local volumetric mass density in perturbers, and $\hat{z}$ is the unit vector normal to the disk plane. To an order of magnitude, this torque is the same as our Equation 7.8, although it is of a completely different nature. Equation 7.11 describes a smooth torque in a fixed direction, while Equation 7.8 is the typical value of a stochastic variable drawn from an axisymmetric distribution with zero mean.

Heisler & Tremaine (1986) also performed numerical experiments to verify that on very long timescales, stellar scattering indeed produces a mean growth on top of the stochastic evolution. The importance of the Galactic tides has been appreciated in subsequent studies of Oort cloud dynamics (Duncan et al., 1987; Heisler, 1990; Dones et al., 2004; Rickman et al., 2008), although the relationship between the stellar encounters and the tidal torques is rarely addressed. Tidal torques are usually treated as separate from the effects of stellar encounters, even though the torque is provided by the same stars that cause the stochastic evolution. By adapting our formalism to reflect a planar distribution of perturbers, we reproduce the effects of the Galactic tides, and in doing so find the distribution function that accounts for both modes of angular momentum growth.

We follow the example of the numerical experiments of Heisler & Tremaine (1986) and approximate the Galaxy locally as a uniform disk of material, with a height much smaller than the scale of the other two dimensions. To create the planar symmetry in the model of stellar encounters, the velocities of the perturbers are restricted to a single direction. While this is not a realistic representation of the directional distribution of field star velocities, it is a simple model to explore and provides a clear example with which to examine the effects of a velocity asymmetry. With $\hat{v}_p$ fixed, the impact parameter $\mathbf{b}$ is confined to a plane, the aspect ratio of which has a much smaller height than width. Both of these properties, a single direction for $\hat{v}_p$ and a non-unity aspect ratio, introduce asymmetries in the distribution function of the comet's angular momentum.

For isotropic perturbers, perturbations of any size J' occur with the same likelihood in all directions in the plane perpendicular to r_b. This ensures that the mean of $\mathbf{J}(t)$ is zero, even though the typical magnitude of the angular momentum increases linearly with time. The cross-section for an interaction in the tidal limit ($b \gg r_b$) scales as b^2, which fixes the power law of the single perturbation PDF. In the planar model, the cross-sectional area that contributes perturbations with small J' is less than b^2 for impact parameters larger than the disk height. The contributions of these regions to each component of $\mathbf{J}'$ depends on the angle between the comet and the disk plane so the axisymmetry is broken. However, these differences manifest only in the lowest J', and their effects on the distribution of accumulated angular momentum are always washed out by the larger perturbations from impact parameters less than the disk height.

Another asymmetry results from the impact parameters of $b \sim r_b$. For $b > r_b$, there is as much cross-sectional area contributing positively to each component as there is negatively. Impact parameters that pass between the sun and the comet, however, impart angular momentum in one direction of one component only, depending on the angle between $\hat{r}_b$ and $\hat{v}_p$. Not coincidentally, the mean torque found in the smooth distribution limit, Equation 7.11, is attributed to the disk of stars passing between the Sun and the comet.

We quantify the effect of this asymmetry by calculating the marginal probability density of each component of the angular momentum vector due to single interactions. Since we have lost the symmetry that admitted the simple analytic solutions, we employ a Monte-Carlo procedure. The position of the comet, which we hold fixed in this example, is $\mathbf{r}_b = \hat{y} + \hat{z}$, so the Sun-comet distance is $r_b = \sqrt{2}$. The perturber velocities are set to the $\hat{z}$ direction: $\hat{v}_p = -\hat{z}$. The possible impact parameters of the perturbers are then restricted to the $x - y$ plane. We randomly choose impact parameters such that they are uniformly distributed over the plane and calculate the $\Delta\mathbf{J}$ delivered to the comet. We assume the other parameters of the system are held constant (v_p and m_p), and to reduce the notation, we use units where $2Gm_p/v_p \equiv 1$. The angular momentum is confined to the plane perpendicular to $\mathbf{r}_b$, which in these coordinates is defined by the basis vectors $\hat{x}$ and $(\hat{y} - \hat{z})/\sqrt{2}$. For simplicity we discuss the x and y components of the perturbation, $\Delta\mathbf{J} \cdot \hat{x} = J'_x$ and $\Delta\mathbf{J} \cdot \hat{y} = J'_y$. In the z-direction, $\Delta\mathbf{J} \cdot \hat{z}$ is exactly the same as J'_y. The positive and negative values for J'_x and J'_y are binned separately; the resulting four histograms then describe the marginal PDF for each component.

Figure 7.1 illustrates the calculation of the single interaction PDF. Panels a and b show logarithmically spaced contours of constant J'_x and J'_y respectively in the plane of possible impact parameters, with the other parameters of the interaction fixed $(\mathbf{r}_b, \mathbf{v}_p, m_b)$. The impact parameter plotted is scaled by $\mathbf{r}_b \cdot \hat{z} = r_z = 1$. The solid contours correspond to positive perturbations and the dashed lines to negative ones. In panel b), the contours for $\pm J'_y$ exhibit an axisymmetric pattern; for each unit of area that contributes perturbations of a given magnitude greater than zero, there is an equivalent area where perturbations have the opposite sign. Thus the single interaction marginal PDF of perturbations in the $\hat{y}$ directions are identical and unchanged from the isotropic case: ${J'_y}^{-1}$ for the distant perturbations, $J'_y(b \gg r_b)$, and ${J'_y}^{-2}$ for the close encounters, $J'_y(b \ll r_b)$. There is no coherent accumulation of angular momentum in the $\hat{y}$ direction.

The contours of panel a), while symmetric at larger $\mathbf{b}$, are not symmetric in the center, where the perturbations only add angular momentum in the negative $\hat{x}$ direction. There is no equivalent area

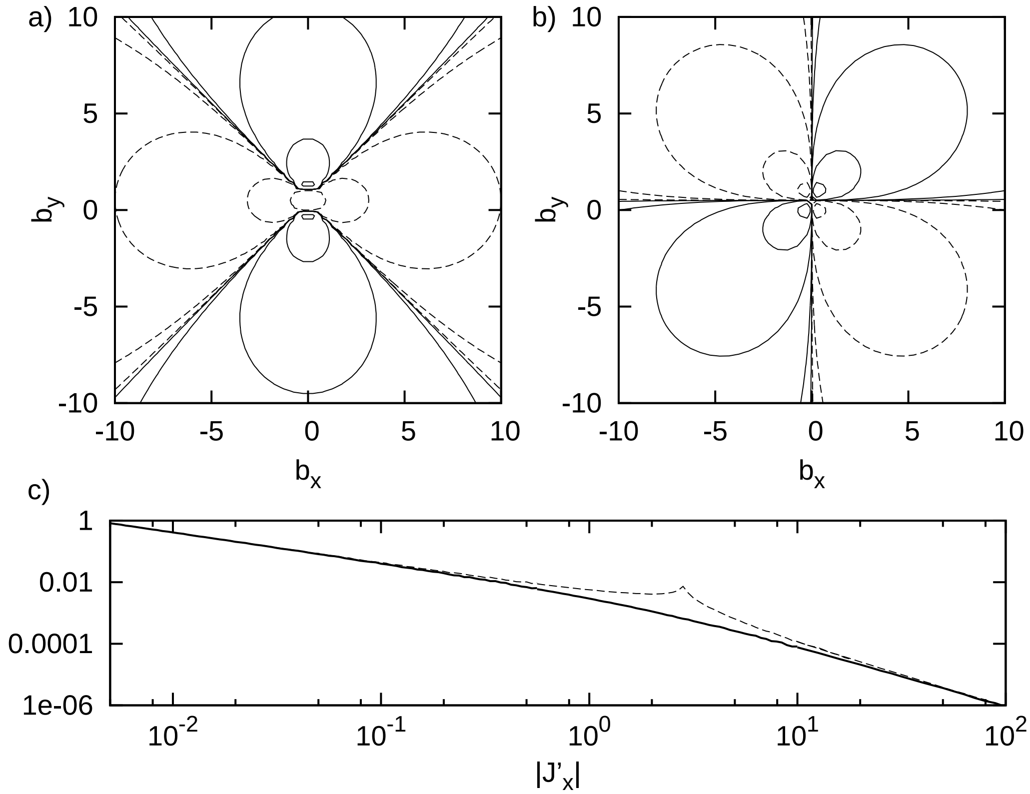

Figure 7.1 Contours of constant J' on the space of impact parameters $\mathbf{b}/(\mathbf{r}_b \cdot \hat{z})$ for positive and negative values of each component of the vector perturbation. The levels are spaced in multiples of ten from $J'/(2Gm_p/v_p) = \pm 10^{-4}$ to ± 1. Panel b, which shows the contours for the $\hat{y}$ direction, is symmetric with respect to positive and negative perturbations. The center of panel a shows an isolated region of negative $\hat{x}$ perturbations that causes an asymmetry in the distribution function. By randomly sampling this space of impact parameters we generate the PDF of the perturbations. The marginal PDF for positive and negative J'_x are plotted in panel c; the spike contains perturbations from the central region of panel a and is the source of the Galactic tidal torques on the comet.

that delivers angular momentum with the opposite sign. We plot the marginal PDF of J'_x, $|J'_x|\mathcal{R}(J'_x)$, in panel c) of Figure 7.1, where the solid line is for perturbations where $J'_x > 0$ and the dashed line is for $J'_x < 0$. The values along the ordinate represent the probability of perturbations with strength of order J'_x relative to the lowest value plotted. In the tidal and close encounter regimes, the two functions are identical. For J'_x of order unity, the contribution of the central region in panel a) is obvious. It is these interactions that give rise to the torque associated with the Galactic tides.

The marginal PDF of $\mathbf{J}'_x$ highlights the source of the Galactic tidal torque. However, it remains to describe how this manifests in the time-dependent distribution function of the comet's angular momentum. In Section 7.2, we used the Boltzmann equation (Equation 7.5) to relate the axisymmetric single perturbation PDF ($p(J')$) to the distribution of angular momentum ($f(\mathbf{J}(t))$). That derivation, however, depends on the simplifications afforded by the single power law form of $p(J')$. For the non-axisymmetric single perturbation PDF depicted in Figure 7.1, an analytic solution to the corresponding Boltzmann equation would be much more difficult to calculate.

Instead, we use a bootstrap technique to estimate the distribution function from a sample of single perturbations. The velocity of the perturbers, v_p, their number density, n, and the area sampled when generating the single interaction PDF, $\pi b_{\max}^2$, set the average time associated with each perturbation, $1/\tau = n\pi b_{\max}^2 v_p$. The angular momentum at a time t is then the sum of t/τ single perturbations. By randomly choosing t/τ perturbations from the PDF and adding them vectorially, we generate a sample of angular momentum vectors that reflect the distribution function at that time t.

To accurately probe the evolution over many orders of magnitude, several single interaction PDFs with different $b_{\max}$ were used. Ignoring large impact parameters increases τ, or equivalently, samples the close encounters more often over a fixed number of perturbations. We verified that the distribution functions calculated with large τ (small $b_{\max}$) are not significantly affected by ignoring the frequent perturbations of smaller J'.

The marginal distribution functions at four different times are shown in Figure 7.2. Each histogram contains 10^6 bootstrapped $\mathbf{J}(t)$, generated from the sum of between 4 and 1000 single perturbations. The distribution of $J_y(t)$ is plotted in the dotted lines for $J_y(t) > 0$ and dash-dotted for $J_y(t) < 0$. For $J_x(t)$, the solid line represents the negative perturbations and the dashed line the positive ones.

The top panel shows the angular momentum distribution at early times, or equivalently, at low typical angular momenta. For reference, we denote this time t_0. Since the single interaction PDF for perturbations of this magnitude is axisymmetric, all four functions are identical. The excess of perturbations to negative J_x' is not visible as the likelihood for those encounters is too low to be sampled in the 10^6 vectors generated for the plot.

The second panel depicts the four distribution functions 100 times later than the time of the top panel. Again both functions show a similar shape, and the typical value for all four has grown linearly with time as predicted by Equation 7.8. The trajectories passing between the sun and the comet have been sampled in a small fraction of the generated $\mathbf{J}(t)$, and the contribution from the spike of Figure 7.1c is apparent. Additionally the normalization of the positive distribution of $J_x(t)$ has fallen to reflect the breaking of the symmetry around $J_x = 0$. The distributions in the first and second panel can be said to be dominated by the influence of the stellar perturbations, and are not strongly affected by Galactic tides. Although the mean of the distribution is always set by the tides (see Equation 7.11), here this value of angular momentum is only realized after rare but strong interactions. The most likely angular momentum vectors, at early times, are distributed axisymmetrically around the origin.

In the third panel the non-axisymmetric growth is manifest. Due to the higher slope of the single encounter PDF, the distribution of the y component of the angular momentum has begun to grow

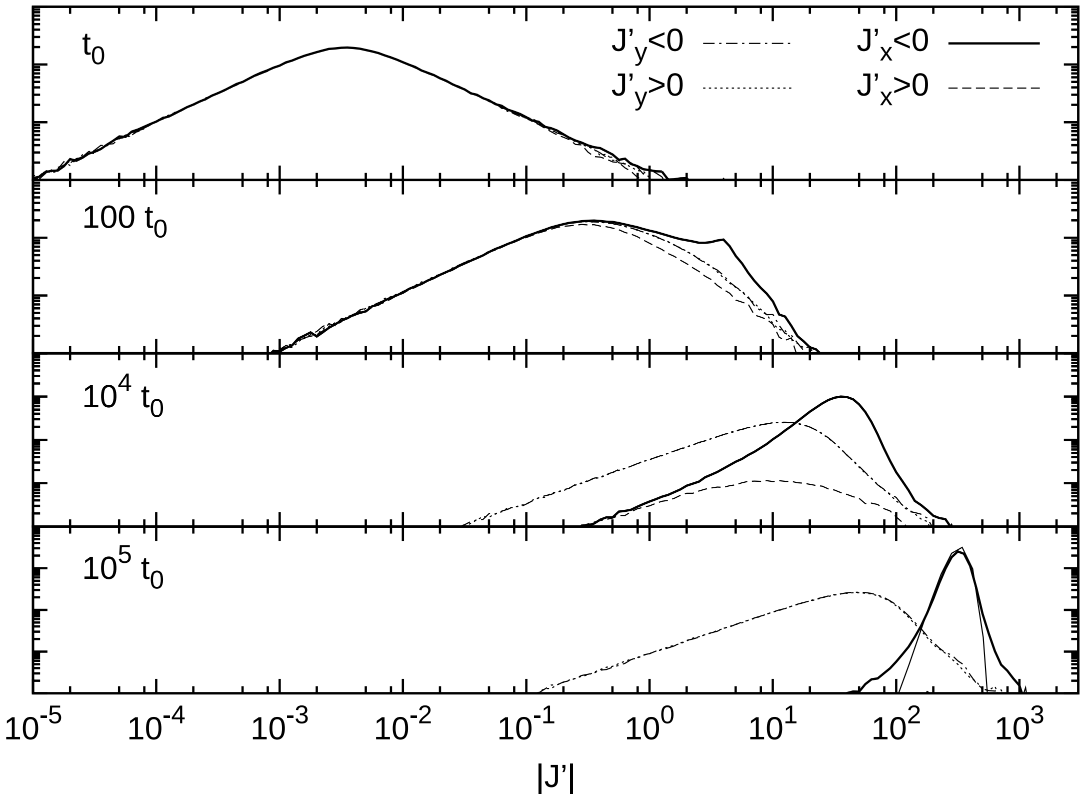

Figure 7.2 Marginal distribution functions of two components of the angular momentum as a function of time. The dotted and dot-dashed lines plot the marginal distribution, $dN/d(\log|J_y|)$, of the $\hat{y}$ component of the angular momentum $\mathbf{J}(t)$. The thick line is the distribution of the $\hat{x}$ component when it is negative, and the dashed line is the positive side. In the top two panels, the comet's angular momentum is best described by the Lévy flight behavior caused by stochastic stellar perturbations. In the bottom two, the coherent torque attributed to the Galactic tides dominates the evolution, causing a visibly asymmetric distribution. The thin line in the bottom panel is a Gaussian distribution with the mean given by the Galactic tidal torques and the variance given by the variance of the single interaction PDF multiplied by the number of encounters.

only as $t^{1/2}$; the accumulations of kicks from all of the impact parameters smaller than r_b contribute to the shape of this distribution. Unfortunately a PDF of this slope does not admit a self-similar distribution function; asymptotically, the distribution approaches a Gaussian logarithmically over time (Shlesinger et al., 1995).

The perturbers passing between the sun and the comet deliver angular momentum in the $-\hat{x}$ direction coherently and thus the typical $-J_x(t)$ continues to increase linearly in time. The normalization of the histogram for positive $J_x(t)$ has decreased substantially, which is another indicator that the total distribution of $J_x(t)$ is no longer centered on the origin. In the fourth panel, only 10 times later than the third, the marginal distribution function for $J_x(t)$ is entirely dominated by the accumulated effects of non-canceled encounters. There are no values of $J_x(t) > 0$ in the sample at this time. Again, the distribution function does not admit an analytic form. For reference, we plot a Gaussian distribution with the mean described by Equation 7.11, and the variance expected given the single encounter PDF, $\sigma^2 = \sigma^2_{\mathrm{PDF}} t$. The distribution function only approaches this approximated shape logarithmically in time.

Figure 7.2 reveals the nature of the coherent torque by Galactic tides as merely the long term effects of anisotropic stellar encounters. It is only a matter of principle what to call the interactions of the comets with field stars. To determine the relevant behavior, one must specify which impact parameters are the most important for the behavior of the comet. On shorter timescales, or for smaller angular momenta, the distant perturbations create the axisymmetric distribution function associated with stochastic stellar encounters. Over timescales long enough that many trajectories have sampled the region between the Sun and comet, the system is best characterized as evolving under the Galactic tides.

As a physical example, we again examine the formation of the Oort cloud, where a proto-comet must gain enough angular momentum to raise its periapse q by Δq to avoid perturbations from the planets. The influence of the planets falls off rapidly with increasing q, so a reasonable value for $\Delta q/q$ is on the order of 10% (Duncan et al., 1987). The distant stellar encounters will be responsible for building the Oort cloud if a single interaction at an impact parameter $b \sim a$ can provide enough angular momentum to increase the periapse. If these single encounters are too weak, the coherent growth due to Galactic tides is required. We find the following inequality for when the mean tidal growth, rather than stochastic evolution, dominates:

$$\left(\frac{\Delta q}{q}\right)\left(\frac{M_\odot}{m_p}\right)\left(\frac{v_p}{v_q}\right) \gg 1, \tag{7.12}$$

where $v_q = (Gm_p/q)^{1/2}$ is the local rotational velocity at periapse. At the semimajor axis of Jupiter, this velocity is about 15 km s^{-1}, and near Neptune it is about 5 km s^{-1}. Typical velocity dispersions of stars in the solar neighborhood are $15 - 40$ km s^{-1} (Binney & Tremaine, 1987). Then in the inner solar system, the tidal torque is less important than the stellar encounters for freeing the comets from planetary perturbations. In the outer solar system, the left-hand side of Equation 7.12 is close to unity, meaning the stellar encounters and the tidal torque play a comparable role.

Our new understanding of the relationship between stellar encounters and tides presents a clearer picture of the most appropriate way to model the excitation of angular momentum in an Oort cloud comet. If the prescription for stellar encounters includes the planar symmetry of the stars, then no extra torque is required to represent the Galactic tides. If the stellar encounter model has an isotropic velocity distribution, then an extra term representing the torque should be included, but only at late enough times that encounters passing between the sun and the comet are common.

7.4 Conclusions

In this work we have shown that the angular momentum delivered to nearly radial comets by passing stars follows a Lévy flight. From the properties of a single scattering between the comet and the star, we derive the distribution function of the angular momentum of the comet as a function of time. Our calculations agree with the estimates made in earlier work on Oort cloud formation, that stellar perturbations can raise the periapses of comets significantly in only several hundred Myrs. A careful examination of the scattering process for an anisotropic velocity distribution reveals the presence of the coherent angular momentum growth that is usually attributed to the large scale potential of the Galaxy. The effects of stellar encounters and the Galactic tidal torques then cannot be treated as two distinct processes. On shorter timescales the distribution function of the comet is unaffected by the tidal torque; on long timescales the distribution is entirely dominated by it. Since the presence of the tidal torque depends on the perturber velocity distribution, simulations of cometary evolution that include stellar encounters must be careful not to double-count the Galactic tides by either including an explicit torque or enforcing a planar symmetry, but not both.

These results provide a formal understanding of the effects of stellar encounters on nearly radial comets. However, it is only the first step towards a complete statistical picture of the formation of the Oort cloud. The effects of the stellar perturbations must be convolved with the diffusion of the comets' semimajor axes caused by planetary perturbations. This type of diffusion is not without complications, as orbital resonances between the comet and the planet must be accounted for to produce accurate diffusion coefficients (Malyshkin & Tremaine, 1999; Pan & Sari, 2004). Additionally, the diffusion of the semimajor axis for a comet whose orbit crosses that of a planet has been shown to exhibit properties of a Lévy flight (Zhou et al., 2002).

We thank the Institute for Advanced Study for their hospitality while some of this work was completed.

Bibliography

Bahcall, J. N., Hut, P., & Tremaine, S. 1985, ApJ, 290, 15

ben Avraham, D., Ben-Naim, E., Lindenberg, K., & Rosas, A. 2003, Phys. Rev. E, 68, 050103

Ben-Naim, E., & Krapivsky, P. L. 2002, Phys. Rev. E, 66, 011309

Ben-Naim, E., & Machta, J. 2005, Physical Review Letters, 94, 138001

Binney, J., & Tremaine, S. 1987, Galactic dynamics (Princeton, NJ, Princeton University Press, 747 p.)

Brasser, R., Duncan, M. J., & Levison, H. F. 2006, Icarus, 184, 59

Brown, M. E., Bouchez, A. H., Rabinowitz, D., Sari, R., Trujillo, C. A., van Dam, M., Campbell, R., Chin, J., Hartman, S., Johansson, E., Lafon, R., Le Mignant, D., Stomski, P., Summers, D., & Wizinowich, P. 2005, ApJ, 632, L45

Brown, M. E., van Dam, M. A., Bouchez, A. H., Le Mignant, D., Campbell, R. D., Chin, J. C. Y., Conrad, A., Hartman, S. K., Johansson, E. M., Lafon, R. E., Rabinowitz, D. L., Stomski, Jr., P. J., Summers, D. M., Trujillo, C. A., & Wizinowich, P. L. 2006, ApJ, 639, L43

Canup, R. M. 2005, Science, 307, 546

Cash, J. R., & Karp, A. H. 1990, ACM Trans. Math. Softw., 16, 201

Chambers, J. E. 1999, MNRAS, 304, 793

—. 2001, Icarus, 152, 205

Collins, B. F., & Sari, R. 2006, AJ, 132, 1316

—. 2008, AJ, 136, 2552

Collins, B. F., Schlichting, H. E., & Sari, R. 2007, AJ, 133, 2389

Cresswell, P., & Nelson, R. P. 2006, A&A, 450, 833

Danby, J. M. A. 1988, Fundamentals of Celestial Mechanics

Dones, L., & Tremaine, S. 1993, Icarus, 103, 67

Dones, L., Weissman, P. R., Levison, H. F., & Duncan, M. J. 2004, Oort cloud formation and dynamics (Comets II), 153–174

Duncan, M., Quinn, T., & Tremaine, S. 1987, AJ, 94, 1330

—. 1989, Icarus, 82, 402

Duncan, M. J., Levison, H. F., & Lee, M. H. 1998, AJ, 116, 2067

Duncan, M. J., & Quinn, T. 1993, ARA&A, 31, 265

Fernandez, J. A. 1997, Icarus, 129, 106

Ford, E. B., & Chiang, E. I. 2007, ApJ, 661, 602

Franchi, I. A., Baker, L., Bridges, J. C., Wright, I. P., & Pillinger, C. T. 2001, Royal Society of London Philosophical Transactions Series A, 359, 2019

Fraser, W. C., Kavelaars, J. J., Holman, M. J., Pritchet, C. J., Gladman, B. J., Grav, T., Jones, R. L., Macwilliams, J., & Petit, J.-M. 2008, Icarus, 195, 827

Fuentes, C. I., & Holman, M. J. 2008, AJ, 136, 83

Goldreich, P., Lithwick, Y., & Sari, R. 2004a, ApJ, 614, 497

—. 2004b, ARA&A, 42, 549

Goldreich, P., & Sari, R. 2003, ApJ, 585, 1024

Goldreich, P., & Tremaine, S. 1980, ApJ, 241, 425

Goldreich, P., & Tremaine, S. D. 1978, Icarus, 34, 227

Greenberg, R., Bottke, W. F., Carusi, A., & Valsecchi, G. B. 1991, Icarus, 94, 98

Greenzweig, Y., & Lissauer, J. J. 1990, Icarus, 87, 40

Halliday, A. N., & Kleine, T. 2006, in Meteorites and the Early Solar System II, ed. D. S. Lauretta & H. Y. McSween, Jr., 775–801

Hayashi, C. 1981, Progress of Theoretical Physics Supplement, 70, 35

Heggie, D. C. 1975, MNRAS, 173, 729

Heggie, D. C., & Rasio, F. A. 1996, MNRAS, 282, 1064

Heisler, J. 1990, Icarus, 88, 104

Heisler, J., & Tremaine, S. 1986, Icarus, 65, 13

Hindmarsh, A. C., Brown, P. N., Grant, K. E., Lee, S. L., Serban, R., Shumaker, D. E., & Woodward, C. S. 2005, ACM Transactions on Mathematical Software, 31, 363

Holmberg, J., & Flynn, C. 2000, MNRAS, 313, 209

Ida, S., & Makino, J. 1992, Icarus, 96, 107

Kaib, N. A., & Quinn, T. 2008, Icarus, 197, 221

Kaiser, N., Aussel, H., Burke, B. E., Boesgaard, H., Chambers, K., Chun, M. R., Heasley, J. N., Hodapp, K.-W., Hunt, B., Jedicke, R., Jewitt, D., Kudritzki, R., Luppino, G. A., Maberry, M., Magnier, E., Monet, D. G., Onaka, P. M., Pickles, A. J., Rhoads, P. H. H., Simon, T., Szalay, A., Szapudi, I., Tholen, D. J., Tonry, J. L., Waterson, M., & Wick, J. 2002, in Presented at the Society of Photo-Optical Instrumentation Engineers (SPIE) Conference, Vol. 4836, Survey and Other Telescope Technologies and Discoveries. Edited by Tyson, J. Anthony; Wolff, Sidney. Proceedings of the SPIE, Volume 4836, pp. 154-164 (2002)., ed. J. A. Tyson & S. Wolff, 154–164

Kenyon, S. J., & Bromley, B. C. 2006, AJ, 131, 1837

Kenyon, S. J., & Luu, J. X. 1998, AJ, 115, 2136

Kokubo, E., & Ida, S. 1995, Icarus, 114, 247

—. 1996, Icarus, 123, 180

—. 1998, Icarus, 131, 171

—. 2002, ApJ, 581, 666

Lee, M. H. 2000, Icarus, 143, 74

Lee, M. H., & Peale, S. J. 2006, Icarus, 184, 573

Levison, H. F., & Morbidelli, A. 2007, Icarus, 189, 196

Lissauer, J. J. 1987, Icarus, 69, 249

Luu, J. X., & Jewitt, D. C. 2002, ARA&A, 40, 63

Malyshkin, L., & Tremaine, S. 1999, Icarus, 141, 341

Matsubayashi, T., Makino, J., & Ebisuzaki, T. 2007, ApJ, 656, 879

Melosh, H. J., Nemchinov, I. V., & Zetzer, Y. I. 1994, in Hazards Due to Comets and Asteroids, ed. T. Gehrels, M. S. Matthews, & A. M. Schumann, 1111–1132

Morbidelli, A., & Levison, H. F. 2004, AJ, 128, 2564

Murray, C. D., & Dermott, S. F. 1999, Solar system dynamics (Cambridge, UK, Cambridge University Press, 593 p.)

Noll, K. S., Grundy, W. M., Chiang, E. I., Margot, J.-L., & Kern, S. D. 2008, in The Solar System Beyond Neptune, ed. M. A. Barucci, H. Boehnhardt, D. P. Cruikshank, & A. Morbidelli, 345–363

Ohtsuki, K., Stewart, G. R., & Ida, S. 2002, Icarus, 155, 436

Oort, J. H. 1950, Bull. Astron. Inst. Netherlands, 11, 91

Ozima, M., Podosek, F. A., Higuchi, T., Yin, Q.-Z., & Yamada, A. 2007, Icarus, 186, 562

Pahlevan, K., & Stevenson, D. J. 2007, Earth and Planetary Science Letters, 262, 438

Pan, M., & Sari, R. 2004, AJ, 128, 1418

—. 2005, Icarus, 173, 342

Petit, J.-M., & Henon, M. 1986, Icarus, 66, 536

Phinney, E. S. 1992, Royal Society of London Philosophical Transactions Series A, 341, 39

Press, W. H., Teukolsky, S. A., Vetterling, W. T., & Flannery, B. P. 1992, Numerical recipes in C. The art of scientific computing (Cambridge: University Press, —c1992, 2nd ed.)

Quinlan, G. D., & Tremaine, S. 1990, AJ, 100, 1694

Rafikov, R. R. 2003, AJ, 125, 942

—. 2004, AJ, 128, 1348

Rasio, F. A., & Ford, E. B. 1996, Science, 274, 954

Rasio, F. A., & Heggie, D. C. 1995, ApJ, 445, L133

Rickman, H., Fouchard, M., Froeschlé, C., & Valsecchi, G. B. 2008, Celestial Mechanics and Dynamical Astronomy, 102, 111

Saha, P., & Tremaine, S. 1992, AJ, 104, 1633

—. 1994, AJ, 108, 1962

Sato, K. 1999, Levy Processes and Infinitely Divisible Distributions (Cambridge, UK, Cambridge University Press, 486 p.)

Schlichting, H. E., & Sari, R. 2007, ApJ, 658, 593

Sesana, A., Haardt, F., & Madau, P. 2007, ApJ, 660, 546

Shlesinger, M. F., Zaslavsky, G. M., & Frisch, U. e. 1995, Levy Flights and Related Topics in Physics (New York: Springer-Verlag)

Sigurdsson, S., & Phinney, E. S. 1995, ApJS, 99, 609

Stairs, I. H. 2004, Science, 304, 547

Stern, S. A., Bottke, W. F., & Levison, H. F. 2003, AJ, 125, 902

Stewart, G. R., & Ida, S. 2000, Icarus, 143, 28

Tholen, D. J., Buie, M. W., Grundy, W. M., & Elliott, G. T. 2008, AJ, 135, 777

Thommes, E. W., Duncan, M. J., & Levison, H. F. 2003, Icarus, 161, 431

Trujillo, C. A., & Brown, M. E. 2001, ApJ, 554, L95

Veillet, C., Parker, J. W., Griffin, I., Marsden, B., Doressoundiram, A., Buie, M., Tholen, D. J., Connelley, M., & Holman, M. J. 2002, Nature, 416, 711

Ward, W. R. 1986, Icarus, 67, 164

Weaver, H. A., Stern, S. A., Mutchler, M. J., Steffl, A. J., Buie, M. W., Merline, W. J., Spencer, J. R., Young, E. F., & Young, L. A. 2006, Nature, 439, 943

Weidenschilling, S. J. 2005, Space Science Reviews, 116, 53

Wetherill, G. W., & Stewart, G. R. 1989, Icarus, 77, 330

—. 1993, Icarus, 106, 190

Wisdom, J. 1980, AJ, 85, 1122

Wisdom, J., & Holman, M. 1991, AJ, 102, 1528

Yoder, C. F., & Peale, S. J. 1981, Icarus, 47, 1

Yu, Q. 2002, MNRAS, 331, 935

Zhou, J.-L., Sun, Y.-S., & Zhou, L.-Y. 2002, Celestial Mechanics and Dynamical Astronomy, 84, 409